Title
Tuning far-field light-matter interactions using three dimensional plasmonic meta-structures

Author
Khan, MD Imran

Publication Date
2021

UNIVERSITY OF CALIFORNIA, MERCED

Tuning far-field light-matter interactions using three dimensional plasmonic meta-structures

A dissertation submitted in partial satisfaction of the requirements for the degree
Doctor of Philosophy in Physics

by

Md Imran Khan

Committee in charge:
Professor Jay Sharping, Chair
Professor Ajay Gopinathan
Professor Arnold D Kim
Professor Sayantani Ghosh

2021

The Dissertation of Md Imran Khan is approved, and it is acceptable in quality and form for publication on microfilm and electronically:

Ajay Gopinathan

Arnold D Kim

Sayantani Ghosh

Jay Sharping, Committee Chair

University of California, Merced
2021

To my mother and brother, their constant support and encouragement propelled me throughout my graduate studies.

To my father, who sparked my interest in studying physics. I wish you were here.

Contents

List of abbreviations

AuNPs	Gold nanoparticles	EM	Electromagnetic
3D	Three dimensions	MDR	Morphology dependent Resonance
MFS	Methods of Fundamentals of Solutions	FSS	Frequency Selective Surface
LSPR	Localized Surface Plasmon Resonance	THz	Terra Hertz
RF	Radio frequency	TE	Transvers Electric
TM	Transvers Magnetic	MG	Maxwell-Garnett
NP	Nanoparticles	FWHM	Full Width at Half Maximum
TMSPA	N-[3-(trimethoxysilyl)propyl]ethylenediamine	SiNPs	Silica nanoparticles
RCF	Relative centrifugal force	DI	Deionized
SEM	Scanning Electron Microscope	UV-Vis	Ultraviolet-Visible
TTL	Trough-The-Lens	BSD	Backscattered electron detector
nm	Nanometer	-OH	Hydroxyl
NSOM	Near filed scanning optical microscope	SE	Secondary Electron

List of symbols

λ	Wavelength	λ_{inc}	Incident wavelength
$\Delta\lambda$	Wavelength difference	ν_0	Frequency in vacuum
σ_s	Scattering cross-section	χ	Size parameter
λ_0	Wavelength in vacuum	m_0	Refractive index in medium
m	Complex refractive index of scattering particle	n	Real part of the refractive index
K	Extinction coefficients	R	Radius
σ_{abs}	Absorption cross-section	Im	Imaginary part
σ_{ext}	Extinction cross-section	Re	Real part
π	Pi	a_n, b_n	Mie coefficients
Ψ, ξ	Wavefunction	$J_{n+1/2}$	Bessel function of the first kind
P	Polarization	e	Unit electric charge
x	Displacement	N	Numbers
$\mathcal{E}$	Electric field	ϵ	Permittivity
ϵ_r	Relative permittivity	ϵ_0	Vacuum permittivity
ω	Oscillation frequency	i	Imaginary unit constant
γ	Damping constant	m_e	Electron rest mass
ω_p	Plasma frequency	ϵ_m	Metals permittivity
ϵ_d	Dielectric permittivity	m^*	Effective mass
$\epsilon_\propto$	Effective permittivity	∞	Infinity

C_n^{TE}	Transverse electric coefficient	C_n^{TM}	Transverse magnetic coefficient
k_0	Wavenumber in free space	f	Filling fraction
P_s	Polarization vector	$\psi^{ext}, \psi^{int}, \psi^{s}$	Exterior, interior, scattered wavefunction
∂	Partial differential operator	α	Strength parameter
σ_t	Total cross-section	$\theta, \quad \varphi$	Radia, Azimuthal angle
M	MFS points	σ_g	Geometric cross-section
σ_E	Extinction cross-section	R_c	Core Radius
k_1	Wavenumber in a medium	G	Green's function
l	Length parameter	∇	Nabla operator
$\hat{o}$	Incident direction	$\hat{\imath}$	Direction of propagation
$F(\hat{o}, \hat{\imath})$	Complex scattering amplitude	σ_d	Differential cross-section
ϖ_0	Scattering albedo	g	Anisotropy factor
μ	Polar angle	q	Q-point Gauss-Legendre points

List of figures

Acknowledgments

I would like to express my gratitude and appreciation to my advisors Dr. Sayantani Ghosh and Dr. Arnold D Kim, for their continuous support and guidance in all aspects of my graduate studies. It was my great pleasure to working with them.

I would like to thank my lab mates for their assistance and collaboration.

I would like to thank Dr. Tao Ye and his graduate student Zach Petrek for collaborating and facilitating the meta-structure fabrication project. Zach Petrek's input on the optimization process of core-shell meta-structure fabrication was invaluable.

I would like to thank Dr. Ryan Baxter and his graduate student Ryan Brisbin for the collaboration project on characterizing the optical properties of the Luminescent organic molecules (LOMS). That helped me to gain insight into the novel LOMS.

I would like to thank Dr. Son Nguyen and his graduate student Pin Lyu for the collaboration project on scattering cross-section measurements of the Palladium nanoparticles.

I would like to thank my Ph.D. committee chair Dr. Jay Sharping and committee member Dr. Ajay Gopinathan for their support.

I acknowledge the support of CCBM at UC Merced, the National Science Foundation, and the Air Force Office of Scientific Research.

Curriculum Vitae

Md Imran Khan

Ph. D Candidate, Physics

University of California. Merced, School of Natural Sciences

5200 N, Lake Rd. Merced. CA 95344

Advisors: Prof Sayantani Ghosh, Prof Arnold D Kim

EDUCATION

Ph.D. Candidate University of California, Merced	August 2016 - Present 3.58/4.0
Master of Science (M.S.), Physics Binghamton University, The State University of New York	May 2016
Bachelor of Science (B.Sc.), Physics. University of Dhaka.	May 2009

AWARDS AND ACHIEVEMENTS

NSF-CREST Graduate scholar. CCBM), UC MERCED. August 2017 – Present

RESEARCH EXPERIENCE

Nano plasmonics for broadband scattering suppression using 3D Metastructure.

Department of Physics, University of California Merced. Feb. 2017-Present

- Developed a unique numerical model to simulate, characterize and compare the multiple interaction between a spherical dielectric core and plasmonic nanoparticles surrounding it using MatLab and Python.
- Design, assemble, & develop necessary processes with multiple (5+) components operating in tandem to collect diffused light by integrating sphere and measure scattering cross sections in the spectral range of 430nm – 700nm using tunable supercontinuum pulsed laser system connected to a spectrometer.
- Developed a characterization process for sample size distribution(~700nm) measured with Dynamic Light Scattering (DLS), imaging of shell structure by Scanning Electron Microscope

(SEM) and shell wall thickness (~30nm), interparticle spacing (~13nm) was measured using Transmission Electron Microscopy (TEM).

- Optimized nano assembly process to improve sample formation speed (2 times faster) and sample integrity (~30% surface coverage). Developed an alternate route to fabricate core-shell meta structure to compensate lab shutdown due to Covid-19.
- Designed, assembled, and programed experimental system to measure diffraction using a tunable laser and automated data acquisition system using LabView.

Non radiative energy transfer mechanism in Gold nano clusters.

Department of Physics, University of California Merced. May. 2017-2019

- Develop, characterize, & collaborate research on non-radiative energy transfer (FRET, NSET, NVET) measurements between fluorophore (Rred, Cy5, Alexa488), water soluble quantum dots and gold nanocluster (Au_{25}NC, ~2nm) using DNA origami tiles.
- Design & assemble necessary components for Time Resolved Photoluminescence (TRPL) measurements to detect energy transfer between fluorophore and gold nano-cluster (Au_{25}) at varying distances (5nm-17nm) in between.
- Improve signal-noise ratio (5 times) from dilute(50pM-100nM) liquid samples by integrating home built optics.

Collective motion in heterogeneous drone swarms.

Department of Physics, University of California Merced. August 2017 – May 2018

- Design & develop experiment to study effect of heterogeneity on drone swarm made of 110 robotic drones (Kilobot).
- Program, maintenance & troubleshoot microcontroller (AT328) based swarming bots.

Effect of volume on the heterogenous nucleation rate of the Lead-free solder alloys.

Department of Physics. Binghamton University, NY February 2013-December 2015

- Heterogenous nucleation rate studied on C4(IBM microelectronics) led free solder bumps ($150\mu m$-$100\mu m$ diameter).
- Samples were also fabricated in house by making square cut grooves of various sizes ($80\mu m - 100\mu m$) applying wet etching of SiO_2 substrate and depositing Tin (Sn), Coper (Cu) and Silver (Ag) of ~100nm layers using Plasma Enhanced Chemical Vapor Deposition (PECVD) and Sputtering.

PROFESSIONAL AND RELATED EXPERIENCE

Graduate Research Associate. Universal Instruments. Conklin NY. August 2013 – May 2014

Effect of Sn component surface finish on 92.5Pb-5Sn-2.4Ag.

- The effect of added (7.4%) Tin (Sn) on the melting temperature, microstructure and mechanical behavior of 92.5Pb-5Sn-2.5Ag (alloy 151, Indium Corporation) was examined using Differential Scanning Calorimeter (DSC), Scanning Electron Microscope (SEM) and Dage 4000 Plus respectively. See below for related publication.
- Significant changes to the microstructure were observed by adding Sn, with an increase in the precipitate area fraction (20%) and a change from an equiaxed structure to dendritic structure.

CLEAN ROOM

- Led free solder bump of Tin (Sn), Copper (Cu) and Silver (Ag) applying wet etching, E-Beam evaporator, and PECVD.
- End to end microfabrication experience of Thin Film Transistor.

TEACHING AND MENTORING EXPERIENCE

Math Instructor (pre-calculus). University of California. Merced August 2018, 2017

Graduate scholar mentor. (CCBM), UC Merced May 2018-May 2019

- Supervised and trained undergraduate students on research procedure, data collection and interpretation, and lab safety on an average of 7 hours per week.
- Mentored undergraduate students to prepare for graduate school applications as a part of the CCBM graduate scholar program.

PUBLICATIONS, PRESENTATIONS

- **Md Imran Khan,** Sayantani Ghosh, and Arnold Kim. “Engineering spectral and spatial scattering profiles in the visible spectrum using nanoplasmonic mesoscale assemblies”. *publication in progress*(2021)**.**
- **Md Imran Khan**, S. Ghosh, R. Baxter, and A. Kim, "Modeling broadband cloaking using 3D nano-assembled plasmonic meta-structures," Opt. Express 28, 22732-22747 (2020).
- Pin Lyu, Randy Espinoza, **Md. Imran Khan,** Sayantani Ghosh, and Son C. Nguyen. “Mechanistic insight into deep holes from interband transitions in Palladium nanoparticle photocatalysts”. *Publication in progress* (2021).
- **Md Imran khan,** Arnold Kim, and Sayantani Ghosh. Broadband cloaking using 3D nano-assembled plasmonic meta-structures. APS, March, 2021. Virtual Meeting. Oral presentation.
- Size tunable passive cloaking platform using self-assembled plasmonic nanostructures. **Imran Khan**, Sayantani Ghosh, Arnold D. Kim. APS March 2020, Denver, Colorado.
- Collective motion in heterogeneous drone swarms. **Imran khan**, Sayantani Ghosh, Kyle Shaw, Ajay Gopinathan. APS March Meeting 2018, Los Angeles, California. Oral Presentation.
- “Effect of Sn Component Surface Finish on 92.5Pb-5Sn-2.5Ag”. Harry Schoeller, Martin Anselm**, Md Imran Khan**, and Eric Cotts (2014) Additional Conference (Device packaging, HiTEC HiTEN, and CICMT): January 2014, Vol.2014, No. HITEC, pp.000364-000371.

SOCIETY MEMBERSHIP

- American Physical Society (APS)
- Optical Society of America (OPTICA)

Abstract

Tuning far-field light-matter interactions using three dimensional plasmonic meta-structures

by
Md Imran Khan

Doctor of Philosophy in Physics

University of California, Merced

2021

Professor Jay Sharping, Chair

Plasmonic meta-structure paves the way to study and manipulate light both in far and near filed. Achieving invisibility (cloaking) by suppressing scattering from an object using a nanoassembled 3D plasmonic meta-structure is the principal study of this dissertation. The concept of "cloaking" an object is a very attractive one, especially in the visible (VIS) and near infra-red (NIR) regions of the electromagnetic spectrum, as that would reduce the visibility of an object to the eye. One possible route to achieving this goal is by leveraging the plasmonic property of metallic nanoparticles (NPs). In this dissertation a model was developed to simulate light in the VIS and NIR scattered by a core of a homogeneous medium, covered by plasmonic cloak that is a spherical shell composed of gold nanoparticles (AuNPs). To consider realistic, scalable, and robust plasmonic cloaks that are comparable, or larger, in size to the wavelength, a multiscale simulation platform was introduced. This model uses the multiple scattering theory of Foldy and Lax to model interactions of light with AuNPs combined with the method of fundamental solutions to model interactions with the core. Numerical results of the simulations for the scattering cross-sections of core-shell composite indicate significant scattering suppression of up to 50% over a substantial portion of the desired spectral range (400 - 600 nm) for cores as large as 900 nm in diameter by a suitable combination of AuNP sizes and filling fractions of AuNPs in the shell.

Suppressing total scattering cross-section by a plasmonic meta-structure effects the angular distribution of the scattered energy both spectrally and spatially. The second project of this dissertation studies the engineering of spatial and spectral profiles applying the plasmonic meta-structures. The possibility of engineering spectral scattering was explored by three-dimensional mesoscale dielectric targets coated with gold nanoparticles (AuNPs) on the surface. By varying AuNP sizes (5-20 nm) and filling fractions of the AuNP coatings (0.1 - 0.3), simulations reveals that under optimal combination of these two parameters, a meta-structure demonstrates reduced or enhanced scattering efficiency compared to the bare core. Furthermore, analysis of the differential scattering cross-section

shows that the presence of the AuNP coating alters the angular distribution of scattering by suppressing the angular sidelobes, thereby guiding the scattered power preferentially in the forward direction. The simulated results highlight that with the ability to tune both the spatial and spectral aspects of the scattering profile, these coated structures may serve as a platform for a variety of applications, including passive cloaking and high-resolution imaging.

The final part of this dissertation is the experimental realization of nano assembled 3D plasmonic meta-structures following the demonstration of plasmonic cloaking by these structures. These meta-structures were designed based on the simulated results, they are comprised of a dielectric (silica) core coated with randomly distributed AuNPs. Silica surface modified by the suitable amine ligand enabled adsorption of the AuNPs, and electrostatic interactions between AuNPs promoted nanoscale self-assembly, resulted in robust core-shell structures. Furthermore, the meta-structure fabrication process was optimized to achieve a desired surface coverage (> 20%) of AuNPs for varied meta-structure sizes (500 nm, 700 nm). Measured scattering cross-section of bare silica and AuNP coated silica sphere revealed broadband scattering suppression by the plasmonic meta-structures up to 570 nm in the visible spectrum. Simulated and the measured scattering cross-sections of the bare cores and core-shell structures showed a very good agreement confirming the applicability of the multiscale simulation platform to the real-world systems.

Chapter 1

Motivation and Research Overview

This dissertation presents the study of light-matter interactions in terms of scattering cross-section, spatial scattering pattern, and scattered power of nano-assembled 3D plasmonic meta-structures. The plasmonic meta structures are made of a dielectric spherical core surrounded by randomly distributed gold nanoparticles (AuNPs). The system sizes studied are in the range of 400 nm to 800 nm. A new and fully 3D model has been introduced for these systems that explicitly incorporates multiple scattering by the dielectric core and the metal nanoparticles. This new model can account for plasmonic meta structures that are larger than previous models were able to consider, which is unique for practically realizable systems. This chapter introduces the research work and significance of the multiscale simulation platform to characterize and predict optical scattering from 3D nano-assembled plasmonic meta structures and provides a brief overview of all the following chapters.

Developing a robust and multiscale simulation platform to characterize and predict optical scattering responses from nano-assembled 3D plasmonic meta structures motivated this research work[1]. Light reflected from an object makes it visible to the human eye or detectable by any sensor. This reflection process is commonly known as scattering, which plays a crucial role in detecting, imaging, and interference that may arise due to scattering. Therefore, reducing the scattering of the incident light and redirecting the scattered energy would enable us to design and develop efficient and practical devices by reducing losses. Additionally, suppressing scattering would make the objects of interest less visible to detection over a specific incident wavelength, commonly known as passive cloaking.

The currently available models for analyzing interactions of incident light with plasmonic meta-structure were limited in system sizes and complexities. These models were based on homogenization of a composite structure, attributing an effective refractive index for all the constituent components. These models were moderately successful in predicting and analyzing electromagnetic responses of complex plasmonic systems. A unique numerical model has been studied in this dissertation. This model acts as a simulation platform for characterizing and predicting scattering cross-section of complex 3D plasmonic structures by accounting multiple interactions between the incident light and all the constituent elements explicitly.

An introduction and review of light-matter interactions, which act as a building block for the complex interaction between the light and plasmonic meta structures, are described in chapter two. Scattering and absorption of electromagnetic (EM) waves by the dielectric particles of different sizes and gold nanoparticles (AuNPs) are reviewed. Scattering by particles of much smaller particles than the incident wavelength (diameter $<< \frac{1}{10}\lambda_{inc}$) are analyzed using Rayleigh scattering theory. The 3D plasmonic meta structures discussed in this dissertation are a composite of AuNPs with sizes ranging from

5 nm to 20 nm and a spherical dielectric core. The optical response of the AuNPs is analyzed using the Rayleigh scattering because their diameter is much smaller than the visible wavelength range (400 nm to 700 nm). In contrast, Mie scattering theory is suitable for particles with a diameter comparable to the incident wavelength, which is between 400 nm to 700 nm in our case. Instead of applying Mie theory, Methods of Fundamentals of Solution(MFS) was used to analyze scattering since it provides a more significant advantage computationally[1].

Chapter three reviews plasmonic cloaking briefly. This is a passive electromagnetic cloaking method that works by leveraging the plasmonic properties of metallic nanoparticles. This specific type of cloaking method does not require an external energy source to operate and works by suppressing scattering from an object. Conventionally a plasmonic cloaking structure is comprised of a target object (core) with a plasmonic cloaking cover (shell). Optical responses of these core-shell plasmonic structures were modeled via dipole approximation and effective medium theory. This chapter briefly reviews plasmonic cloaking, discusses the drawback of the existing model and the necessity for developing a multiscale simulation platform.

A rigorous analysis of the broadband scattering suppression via plasmonic cloaking has been presented in the chapter four. This chapter highlights the mathematical description and computational procedure of our model. The light-matter interaction between AuNP was computed using the generalized Foldy-Lax method. Interaction between the incident light and the spherical dielectric core was computed using the MFS method. A justification for using these methods to analyze the light matter interactions has been provided in this chapter. Broadband scattering suppression ($\Delta\lambda = 430\ nm - 670\ nm$) for a wide range of structure sizes (450 nm-950 nm) has been presented as a concluding result in this chapter.

Multiple scattering and absorption of incident light between the spherical dielectric core and the surrounding AuNP coating enable broadband scattering suppression. Apart from scattering suppression, these multiple interactions also alter the spatial scattering pattern. Tuning scattering patterns and manipulating the directionality of the scattered power by the plasmonic meta-structures are discussed in chapter five. Multiple scattering and absorption decrease the overall coherence of the scattered light. As a result, angular side lobes of the scattered light are suppressed following a narrower central peak. This chapter also illuminates a crucial interaction that promotes the process that makes broadband scattering possible. A way to manipulate and quantify spatial scattering patterns and scattering intensity has been discussed in this chapter.

The simulation platform presented in this dissertation can generate and predict a couple of variations of the plasmonic meta structures that would show scattering suppression. Plasmonic meta structures of two different core sizes were fabricated following the simulation model. Electrostatic nano-assembly was employed to fabricate 3D plasmonic meta structure. The scattering cross-sections were measured by collecting and measuring diffused light intensities from the plasmonic meta structures. A barium sulfate-coated integrating sphere was used to measure the diffused light in transmission and in reflections. The measured scattering cross-section of the plasmonic structures shows scattering suppression compared with the bare silica sphere over the visible wavelength range. An image analysis process was adopted to quantify the surface coverage or filling fraction of the AuNPs on the silica sphere. Critical parameters such as AuNP diameter, silica sphere diameter, and filling fraction were fed to the simulation model to generate a scattering cross-section. The simulated and measured scattering cross-sections were compared with each other to explore the applicability of the simulation model .

Finally, chapter seven is dedicated to the summary and future work regarding the research presented in this dissertation. This chapter highlights some key advantages and achievements of this research work following some future work.

Chapter 2

Light matter interactions

This chapter presents a brief description of scattering and absorption in general. Two widely known theories for analyzing scattering are Rayleigh and Mie scattering theory. These theories have a specific operational regime and related advantages; hence basic equations to calculate scattering and absorption are included. The origin of the bulk plasmon in the metal following surface plasmon resonance and localized surface plasmon resonance is discussed later in this chapter. Finally, scattering and absorption cross-section together as a function of gold nanoparticle diameter is presented as an example of the tunability of light-matter interactions. The concluding part of this chapter is a brief review of the tunability of light matter interaction via plasmonic nanostructures.

2.1 Scattering and absorption cross-section

Incident electromagnetic waves may be redirected, redistributed angularly (scattering), and partially or fully absorbed (absorption) while interacting with an obstacle in the direction of propagation. In our case, this obstacle would be a scattering particle. This section of the dissertation introduces the scattering and absorption cross-section, Rayleigh and Mie scattering theory following the plasmonic interactions.

Incident electromagnetic (EM)wave interacts with the discrete charges (i.e., electrons or protons) of the constituent scattering particles atoms or molecules. As a result, these charges are perturbed and start to oscillate with the same frequency (ν_0) as the incident EM wave[2].

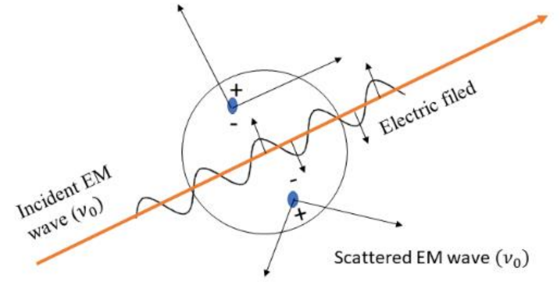

Figure 2.1. Secondary radiation (scattering) by an induced dipole moment

This periodic perturbation in the charge cloud creates a periodic separation of opposite charges, resulting in an induced dipole moment[2]. This oscillating dipole moment acts as a source of secondary radiation or scattered light. The frequency of radiation from the oscillating dipole is mostly the same as the incident frequency ν_0. This type of scattering process is known as elastic scattering. Apart from scattering, a part of the incident EM wave may be extinguished inside the particle when the particle is absorbing. This absorption process refers to a complex refractive index [2]. The scattering and absorption process together is termed as extinction.

A scattering cross-section represents an effective area (cross-section) that is proportional to the probability of interaction of light with an object. Hence, scattering cross-section (σ_s) is defined as a quantity proportional to the rate at which a particular light-matter interaction occurs[3]. Similarly, an absorption cross-section is defined as the probability of absorption due to the interaction of light with the target object[3]. In many practical analysis and experimental setups, absorption cross-section is obtained by subtracting the scattering cross-section from the total extinguished energy (extinction cross-section) due to the interaction of light with the target object.

2.2 Rayleigh and Mie scattering regime

Light scattering by particles of different sizes is analyzed by two theoretical frameworks. This first one is the well-known Rayleigh scattering theory named after Lord Rayleigh. This scattering theory was initially developed for small non-absorbing (dielectric) spherical particles [4]. Later this theory was modified for absorbing (metallic) particles. The second theory is Mie theory, following Gustav Mie, which considers the general spherical solution of the scattering waves[5] and is applicable for both absorbing and non-absorbing particles without a particular bound on particle diameter[6]. A dimensionless parameter known as the size parameter is used to determine the regime of Rayleigh and Mie scattering theory. The size parameter is,

$$\chi = \frac{2\,\pi R}{\lambda} \tag{2.1}$$

Here R is the radius of the particle, and λ the scattering wavelength in the surrounding medium, it is defined as,

$$\lambda = \frac{\lambda_0}{m_0} \tag{2.2}$$

Here λ_0 is the incident wavelength in vacuum, and m_0 is the refractive index of the surrounding medium. The refractive index of the scattering particle m

$$m = n - iK \tag{2.3}$$

Here m is the complex refractive index of the target particle. The real part of the refractive index is n, and K is the extinction coefficient. The value of the extinction coefficient is always non-zero for any material. Materials with K values approaching zero are known as dielectric. The Rayleigh scattering regime is considered for objects with $\chi \ll 1$ and $|m|\chi \ll 1$. This scattering regime assumes that the target particle is sufficiently small. Moreover, EM field incident on the particle is considered uniform at any moment, and the time taken by a wave train to enter the particle is shorter than its period of oscillation[6].

2.2.1 Rayleigh scattering

Light scattering from molecules or very small particles ($R \ll \frac{1}{10}\lambda_{incident}$) falls into the Rayleigh scattering regime [3]. This scattering process is strongly wavelength-dependent [3]. The scattering and absorption cross-sections are,

Scattering cross-section (σ_s):

$$\sigma_{sca} = \frac{2\pi^{\frac{5}{3}}(2R)^6}{\lambda^4}\left|\frac{\widetilde{m}^2-1}{\widetilde{m}^2+2}\right|^2 \;;\quad \widetilde{m} = \frac{n(\lambda)}{n_{background}} \tag{2.4}$$

Absorption cross-section (σ_a):

$$\sigma_{abs} = \frac{8\pi^2}{\lambda}R^3 Im\left|\frac{\widetilde{m}^2-1}{\widetilde{m}^2+2}\right|^2 \tag{2.5}$$

The blue hue of the sky is due to the light scattering off the molecules of air. This is an elastic scattering process since the photon energy (frequency of the scattered light) remains unchanged due to the scattering. The 3D meta structures described in this dissertation have an AuNP coating around a spherical dielectric sphere. Interactions of the incident light with these discrete AuNPs were modeled using Rayleigh scattering. The diameters of these AuNPs were 5, 10, and 20 nm, which are much smaller than the incident wavelength. Hence the Rayleigh scattering theory was appropriate in this case.

2.2.2 Mie Scattering

Mie scattering is dominant for particles whose diameter is comparable to incident wavelength or much larger than the incident wavelength[3][2]. Typical scattering pattern produced by the particles in the Mie scattering regime is like an antenna lobe[2], [3]. These scattering lobes become sharper and more intense in the forward direction as the particle size increases. The scattering and extinction cross-sections are, Extinction cross-section

$$\sigma_{ext} = \frac{\lambda^2}{2\pi} \sum_{n=0}^{\infty} (2n+1)[Re\{a_n\} + Re\{b_n\}] \tag{2.6}$$

Scattering cross-section

$$\sigma_{scate} = \frac{\lambda^2}{2\,\pi} \sum_{n=0}^{\infty} (2n+1)(|a_n|^2 + |b_n|^2) \tag{2.7}$$

The absorption cross-section, σ_{abs} can be calculated by taking differences between the equation 2.6 and equation 2.7.

The parameters a_n and b_n stated above are known as Mie coefficients which are from the expansion of the scattered field and can be determined from the boundary conditions. The parameters a_n and b_n are defined as,

$$a_n = \frac{\Psi_n(\chi)\,\Psi'_n(m\,\chi) - m\,\Psi_n(m\,\chi)\,\Psi'_n(\chi)}{\xi(\chi)\,\Psi'_n(m\,\chi) - m\,\Psi_n(m\chi)\,\xi'_n(\chi)} \tag{2.8}$$

$$b_n = \frac{m\Psi_n(\chi)\,\Psi'_n(m\,\chi) - \Psi_n(m\chi)\,\Psi'_n(\chi)}{m\xi(\chi)\,\Psi'_n(m\,\chi) - \Psi_n(m\chi)\,\xi'_n(\chi)} \tag{2.9}$$

Here the Ricatti-Bessel functions Ψ and ξ are defined in terms of the half-integer-order Bessel function of the first kind ($J_{n+\frac{1}{2}}(z)$). It is worth mentioning that these coefficients (a_n and b_n) diverge as the denominators start to become very small or zero. The divergent cases in the series expansion are denoted as a resonance peak. From the equations 2.8 and 2.9, resonances are strongly dependent on the size parameter χ. Hence these resonances are also known as morphology dependent resonance (MDR)[7]. Apart from the size of the particles, resonance peaks are also influenced by the refractive indices of the particles, and surrounding medium, and incident wavelength.

2.3 Optical properties of metallic nanoparticles

The high density of free electrons originating from the valence electrons gives the metal its unique shiny properties under the visible wavelength. This electron density is responsible for scattering and absorption [8] and gives rise to the interesting phenomena known as a surface plasmon. An extraordinary example of plasmonic interaction of the metallic nanoparticles from the ancient world is the Lycurgus cup (Roman empire, 4th century AD). Figure 2 shows Lycurgus cups in reflected light (green) and in transmitted light (red). These variations in color were possible because of the inclusion of metallic nanoparticles such as copper, silver, and gold in the glass matrix. Light scattered by the silver nanoparticles gives it a greenish hue under reflected light. The AuNP absorbs light around 550 nm, because of that, the Lycurgus cups appear red under transmitted light[9]. The optical properties of the metallic nanoparticles are dependent on the collective oscillations and excitations of the conduction electrons[10]. The coherent oscillation of electrons due to the incident light produces bulk plasmon and localized surface plasmons. The following section describes the fundamentals of surface plasmons briefly.

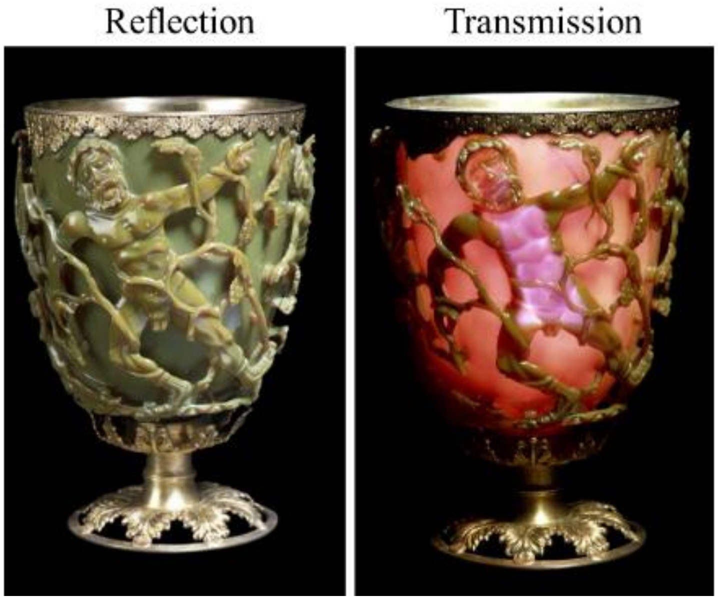

Figure 2.2. Lycurgus cups (Roman empire, 4th century AD). ©British Museum.

2.3.1 Bulk plasmon

Free electrons in the metal experience no significant resistance and act as a gas of charged particles , or plasma under the influence of incident EM waves [8]. The interaction of the incident light with this plasma gas has been described using the Lorentz-Drude model[11]. According to this model, a system of free electron gas is polarized with polarization, $P = -Nex,$ due to the electric field ($\mathcal{E}$) of the incident EM wave. Here N is the number of electrons per unit volume, x is the displacement of electrons from equilibrium due to the EM wave. The displacement vector and the relative permittivity ϵ_r ,

$$\begin{aligned} D &= \epsilon_r \epsilon_0 \mathcal{E} \\ &= \epsilon_0 \mathcal{E} + P \\ &= \epsilon_0 \mathcal{E} - \frac{N\, e^2 \mathcal{E}}{m_0(\omega^2 + i\gamma\omega)} \end{aligned} \tag{2.10}$$

Here ω is the frequency of the incident wave, and γ is the damping constant. From equation 2.10,

$$\epsilon_r(\omega) = 1 - \frac{Ne^2}{\epsilon_0 m_0} \frac{1}{(\omega^2 + i\gamma\omega)} \tag{2.11}$$

The equation 2.11 can be written as,

$$\epsilon_r(\omega) = 1 - \frac{\omega_p^2}{(\omega^2 + i\gamma\omega)} \tag{2.12}$$

Here the quantity $\left(\frac{Ne^2}{\epsilon_0 m_0}\right)^{\frac{1}{2}}$ is known as the plasma frequency ω_p,

$$\omega_p = \left(\frac{Ne^2}{\epsilon_0 m_0}\right)^{\frac{1}{2}} \tag{2.13}$$

For a lightly damped system the constant $\gamma = 0$. Therefore, equation 2.12 can be expressed as,

$$\epsilon_r(\omega) = 1 - \frac{\omega_p^2}{\omega^2} \tag{2.14}$$

This equation 2.14 is an interesting one since it indicates that $\epsilon_r(\omega) = 0$ at plasma frequency (ω_p). An interesting consequence of $\epsilon_r = 0$ is, at this frequency, a collective longitudinal excitation mode is formed where the electric field and the wave vector are parallel [12]. This collective excitation mode is physically a collective oscillation of the conduction electron gas with reference to the background of the positive atomic cores[13]. The quanta of this charge oscillation are known as plasmons or bulk plasmons.

2.3.2 Localized surface plasmon resonance

Surface plasmon or surface plasmon polaritons (SPPs) are propagating electromagnetic excitations along the interface between a metal and dielectric medium. The permittivity of the metal (ϵ_m) and the dielectric medium (ϵ_d) needs to be opposite $(\epsilon_d = -\epsilon_m)$ of each other as a necessary condition to sustain a propagating electromagnetic excitation along the interface[14]. Figure 3 shows a schematic of the propagating plasmons along the interface. This composite system is composed of an EM wave in the dielectric medium and an oscillating electron plasma in the metal. The interaction between the photon and the plasmon are strong enough to be considered as a coupled system called polariton or surface plasmon polariton. Here both modes have decaying characters [15].

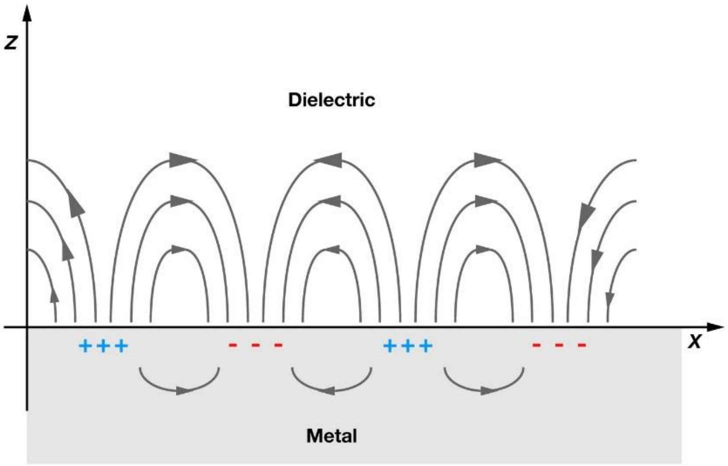

Figure 2.3. Schematic diagram illustrating a surface plasmon polariton or propagating plasmon. Reproduced from reference[14] with permission © Annual Reviews.

In the case of colloidal metallic nanoparticles, the surface plasmon polaritons are non-propagating; hence they are known as a localized surface plasmon. The curved surface of the nanoparticles provides a resulting restoring force on the oscillating electron, causing a resonance [16]. Field amplification both inside and in the near-field zone outside the particle is observed due to this resonance[17], called localized surface plasmon resonance (LSPR).

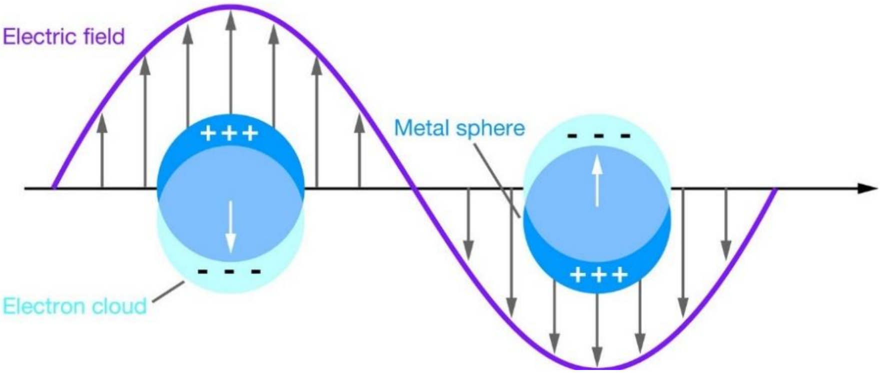

Figure 2.4. Schematic diagram of LSPR for a spherical gold nanoparticle. Reproduced from reference[14] with permission © Annual Reviews.

An advantage of the curved surface is that plasmon resonance can be excited via direct incident light, in contrast to propagating surface plasmons which requires the phase-matching techniques for resonance[18]–[22]. Gold and Silver nanoparticles show LSPR in the visible wavelength region[23][24]. A fascinating consequence of this resonantly enhanced interaction is the bright colors exhibited in reflected and transmitted light.

The origin of the bright colors is LSPR enhanced scattering and absorption[25]. The following section describes the scattering and absorption of the gold nanoparticles (NP).

2.3.2 Scattering and absorption of gold nanoparticles

The differences in the optical properties between a metallic nanoparticle and the bulk metal can be explained in terms of polarizability[8]. The polarizability of a smaller metallic particle or a nanoparticle can be described as.

$$\alpha = 4\,\pi\,R^3\,\frac{\epsilon_m - \epsilon_d}{\epsilon_m + 2\epsilon_d} \tag{2.15}$$

Here polarizability α, depends on the radius (R) of the particle, the permittivity of the metal (ϵ_m), and dielectric (ϵ_d). Based on the expression above, resonance occurs at $\epsilon_m = -2\epsilon_d$, but in the case of undamped plasma resonance occurs at $\omega_p/\sqrt{3}$, here air acts as dielectric independent of the particle size[17]. Plasmonic resonance in the metallic nanoparticles was experimentally found to be dependent on the size and surrounding medium[8]. There is a shift in the resonance frequency due to the Interbrand absorption of the metal[26]. LSPR enables plasmon-enhanced scattering and absorption of metallic nanoparticles. In this dissertation AuNPs plays a key role for enabling multiple scattering and absorption between the spherical dielectric core and the plasmonic shell.

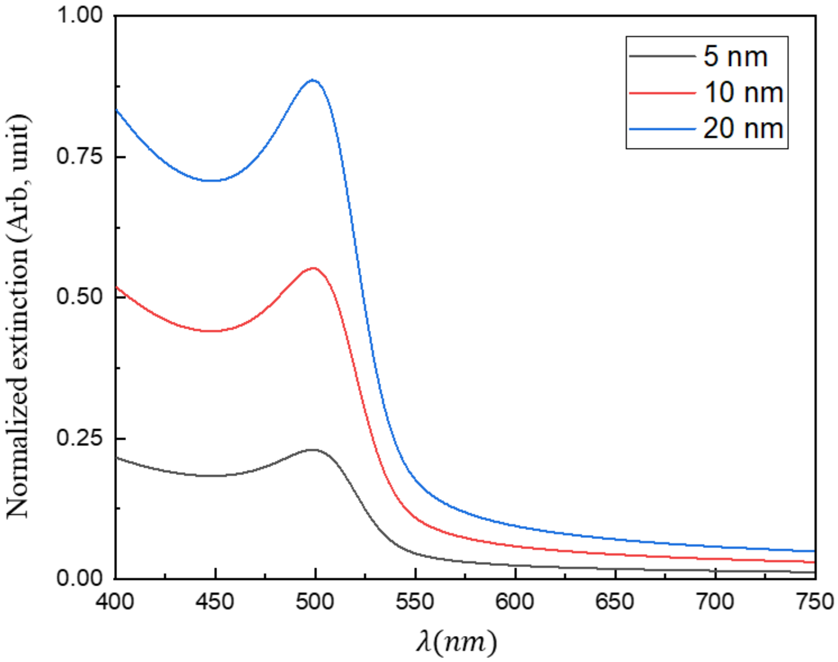

Figure 2.5. Normalized extinction cross-section of gold nanoparticle as a function of size over visible wavelength. Extinction cross-sections are normalized by the corresponding maximum and rescaled.

Normalized extinction cross-sections (scattering plus absorption) of gold nanoparticles of varied sizes were shown in figure 2.5. Extinction cross-sections of 5 (black line), 10 (red line), and 20 nm (blue line) are exhibiting resonance around 510 nm as evidence of plasmon-enhanced scattering and absorption[10]. An increase in the extinction cross-section with the increased diameter shows tunability of light-matter interaction using plasmonic gold nanoparticles. The extinction cross-section was plotted using equations 2.5, 2.6, and optical constants for the AuNPs were from the experimentally measured plasmonic gold thin film[3][27].

2.4 Introduction to plasmonic interaction of the nanostructures

Plasmonic nanostructures show promises for a wide range of applications such as broadband scattering suppressions [1], biosensing [28]–[36], spectroscopy [14], [37]–[48], nanolasing [49]–[60], all-optical switching [61]–[66], nonlinear optical process[67]–[73], and meta surface technology[74]–[84]. Plasmonic nanostructures make a flexible and geometry-dependent response to the electromagnetic field. As a result, these structures yield many exotic properties, such as the ability to confine light to sub-wavelength scales following significant local field enhancement[77][8]. The building block of these plasmonic nanostructures are metallic nanoparticles such as gold, silver, and copper[85]. These metallic nanoparticles have intrinsic nonlinear optical constants, which are many orders of magnitude larger than dielectric materials[86]. At the sub-wavelength scale[87], these nanostructures individually show localized surface plasmon resonances (LSPRs)[88], which are incident electromagnetic fields coupled to the free-electron plasma of a metallic nanoparticle at a metal-dielectric interface[8]. Governing by the size and shape, an individual nanoparticle can be polarized by the incident electromagnetic wave, acting like a lossy dipole antenna[89]. Hence plasmonic nanoparticles shows both scattering and absorption properties[8]. The plasmon-enhanced scattering and absorption properties lead to light-matter interaction tunability by facilitating multiple scattering and absorption between a dielectric host and randomly distributed metallic nanoparticle coating[1][90].

2.4.1 Tuning light-matter interaction using plasmonic nanostructures

Plasmonic responses of the nanostructures are highly tunable as the surface plasmons (SPs) are strongly dependent on materials and structures. Hence by varying constituent metals, semiconductors, dimensions(2D or 3D), and morphology, plasmonic resonance wavelengths can be tuned from ultraviolet(UV), visible, near-infrared(NIR) to far infrared[91]–[94]. Surface plasmons (SPs) are the coupled Electromagnetic (EM) waves with the free electrons on the material dielectric boundary. Conventionally, air works as an interfacing dielectric medium to accommodate SPs. The plasmon resonance frequency is expressed as,

$$\omega_p = \left(\frac{4\,\pi N e^2}{\epsilon_\propto m^*}\right)^{\frac{1}{2}} \tag{2.16}$$

Here N is the carrier density (electron or holes), m^* is the effective mass of the carriers, e is the charge of the carriers (electron or holes), and $\epsilon_\propto$ is the effective permittivity of the system. We can readily conclude from the equation 2.16 that the plasma frequency of a system can be varied by changing the carrier density and effective permittivity. The noble metallic nanoparticle's typical carrier density is$10^{22} - 10^{23}\, cm^{-3}$ and the plasmon resonance frequency is in the NIR to the visible range[95]. In the case of a doped semiconductor, the typical value of N is $10^{16} - 10^{12}\ cm^{-3}$ and the plasmon frequency is in the THz and NIR region[96]. Apart from the carrier or doping density, the plasmon resonance frequency is also strongly dependent on physical size, surrounding host medium, morphology, and geometrical arrangement[97]–[100].

Plasmonic colloidal metallic nanoparticles possess a unique ability to couple with the incident light with wavelengths are much longer than their diameter. As a result, plasmonic nanostructures manifest some extra ordinary optical or electromagnetic response such as negative refractive index, perfect lensing, and transparency or cloaking properties that are not available in naturally occurring materials[101], [102]. These composite structures are commonly known as meta-materials. Wide research interest has been developed to study novel properties of meta materials or artificial materials due to recent advances in nano-synthesis, characterization, and fabrication [103]–[105]. Meta materials are well designed and fabricated nanostructures that collectively show an electromagnetic and optical response beyond the boundaries of the naturally existing materials[106][107]. One of the most exotic metamaterial applications is achieving transparency or invisibility by manipulating the incident light. The working principle of achieving transparency varies depending on the design and applications. A review of some of the electromagnetic cloaking methods and their working principles are presented in the following chapter.

Chapter 3

Passive cloaking via scattering suppression

This chapter briefly reviews conventional electromagnetic cloaking methods. The mechanism of passive cloaking is explored here to a more considerable extent within the scope of this dissertation. Invisibility cloaking by the plasmonic metamaterial recently opened a promising field of research, where spherical core-shell structures at the size of the wavelength of operation can be fabricated and which passively (no external power required) achieve invisibility by canceling scattering[108]. A widely used method to model and compute optical responses from the plasmonic metamaterials is the effective medium theory. Some of the relevant applications of this theory along with the drawbacks are described in this chapter.

3.1 Electromagnetic cloaking method

Passive cloaking by scattering suppression is one possible solution to the electromagnetic cloaking that has been developed over the last few decades[102]. There are several other cloaking methods currently being tested for different physical situations, and a brief overview of those techniques will provide an idea of the existing methods and their advantages or disadvantages. These cloaking methods can be classified into Transformation electrodynamics, Carpet cloaking, and Mantle cloaking[102].

3.1.1 Transformation electrodynamics:

The transformation-based cloaking method works by controlling the flow of electromagnetic energy[109]. For example, a ray of light propagates in a straight line in free space, but if the space coordinates can be modified in such a way that it is stretched or bent, then according to the Fermat principle, the path of the ray will be altered entirely and redirected as shown in figure 3.1.

A medium with specific inhomogeneity, anisotropic permittivity, and permeability distributions makes this type of transformation possible[109]. A two-dimensional metamaterial with a negative refractive index is one such candidate for building a coordinate transforming medium[110], where the cloak is constructed using a metamaterial, and a target object is placed inside it. The magnetic and electric response (permeability and permittivity) of the cloak needs to be exact to match the background impedance of the cloaking shell so that there would be no reflection or scattering from the cloak itself[105].

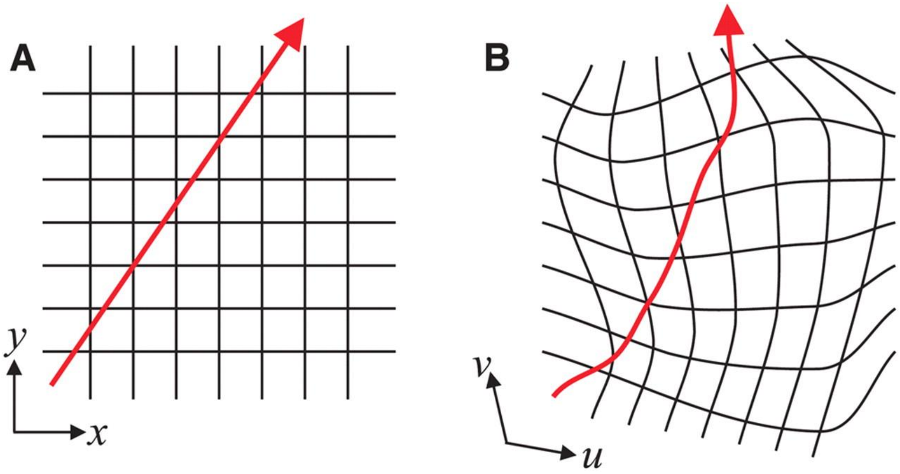

Figure 3.1 Coordinate transformation can be used to manipulate the path of light. Reproduced from reference [109] with permission.©2006, AAAS.

Distance traveled by the light would be larger in the transformed coordinate system, or inside the cloak compared to the free space. This implies the phase velocity of the light inside the cover has to be more than the free space (superluminal) to compensate for the phase delay due to traveling longer distances [111].

According to Kramers-Kronig relation, superluminal propagation only happens for a passive, causal, linear, and time-independent material at an isolated frequency[111]. Therefore, cloaking via transformation electrodynamic is ideal for a single frequency. There are two mentionable drawbacks to this cloaking method. The requirement of superluminal propagation of light prevents broadband cloaking, and the complex fabrication process of the constitutive material makes this method of cloaking difficult. The condition of superluminal flow can be solved by sacrificing the phase of the wave by employing carpet cloaking and its variant[111]. A plasmonic cloak can solve the requirements for the complex fabrication of the constitutive material.

3.1.2 Carpet cloaking

This cloaking method was proposed by Li and Pendry[112]. Experimentally it was shown that a specific type of transformation could be attained in two dimensions with dielectric materials, with practical values of permittivity and weak anisotropy in the cloaked medium[112]. Figure 3.2 shows the simulation and experimental results of carpet cloaking.

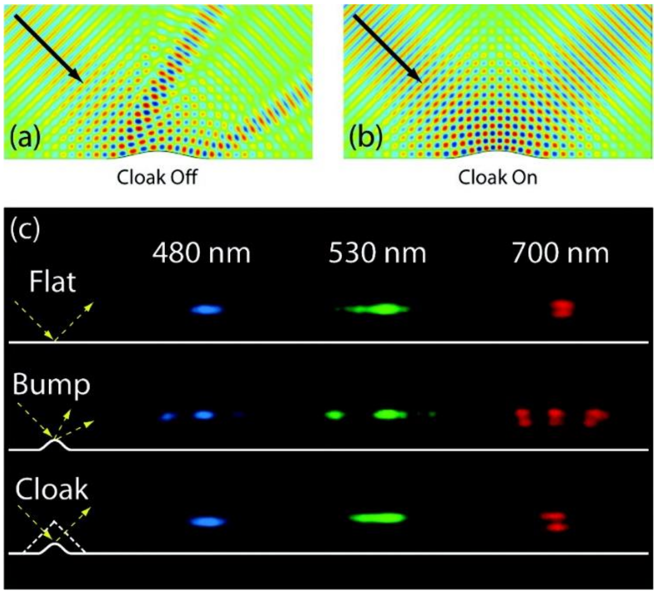

Figure 3.2 (a) and (b) showing a simulated schematic of the carpet cloaking in operation. (c) Experimental results are showing carpet cloaking. Reproduced with permission from[113]. © 2011, American Chemical Society.

A two-dimensional quasi-conformal transformation is applied in this cloaking method. A carpet cloak is built on a perfect electrical conductor (i.e., mirror) as a background or substrate for the target object then a cloak is applied on top of it[112]. Carpet cloaking has been experimentally demonstrated for frequencies ranging from microwave to optical[113][114]. There are a couple of drawbacks to this cloaking method. It cloaks in two dimensions only. The concealed object is readily detectable in the third dimension [115]. Another disadvantage is finding a specific transformation to hide the target object[115].

3.1.3 Mantle cloaking

Mantle cloaking strongly suppresses the scattering of an object by canceling the principal terms in the multipole expansion of the scattered field [116]. Mantle cloaking uses an ultra-thin frequency-selective surface (**FSS**) that is designed to induce a current along the surface that cancels the scattering from the target object [117][118]. This technique is practically applicable at microwave frequencies for which FSS are available and easy to develop[119]. Mantle cloaks have advantages of low weight and thinness. Generally, mantle cloaks are designed using periodic metallic patterns deposited on thin dielectric layers as arrays of stripes, patches, holes, or crosses [118]. One atom thick mantle cloak was proposed using graphene at THz frequencies [120]. Figure 3.3 shows the schematic of a planar surface cloak or mantle cloak. Where a patterned conductor (left) is at the radio frequency (RF) and an atomically thin graphene monolayer is grown on SiO_2

(right) at Terra hertz (THz) frequency. Both geometries can be used to cloak a dielectric planar slab.

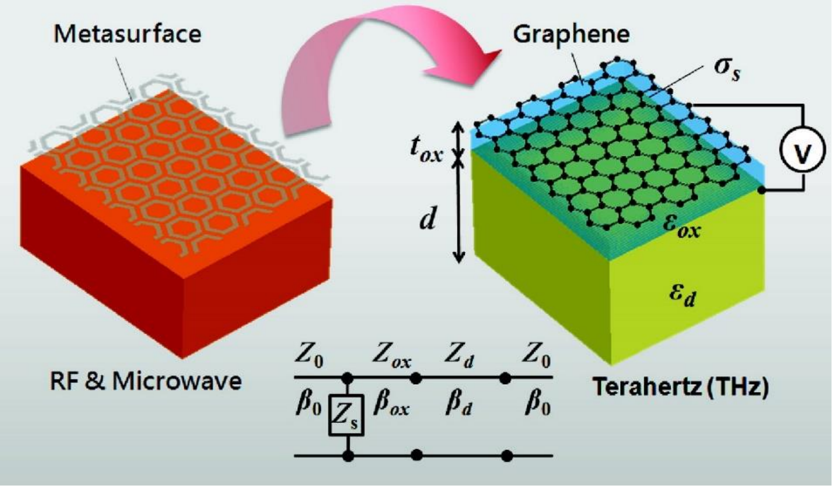

Figure 3.3 Schematic diagram of a planar mantle cloak realized with monolayer graphene operational over the RF, microwave, and THz. Reproduced with permission from reference[120]. © 2011, American Chemical Society.

Mantle cloaks have been extensively studied to suppress scattering from transmitting and receiving antennas because of their conformability and the convenience of fabrication [121][122]. However, the main drawback of mantle cloaking is the frequency selective surface (FSS) that restricts its application to broadband cloaking.

3.2 Passive plasmonic cloaking

This cloaking technique is based on all-angle scattering cancellation using a homogenous layer of material with low or negative permittivity or permeability[123]. This method relies on producing a local polarization vector that is in “anti-phase” in reference to the object to be cloaked[123]. Plasmonic cloaking implies that a well-designed cloaking cover may recover the near and far-field incident wavefront and is independent of the incident angle, form, and polarization of the incident wave and location of the observer[124][125] [126]. Figure 3.4 shows an artistic diagram of the plasmonic cloak in action[127].

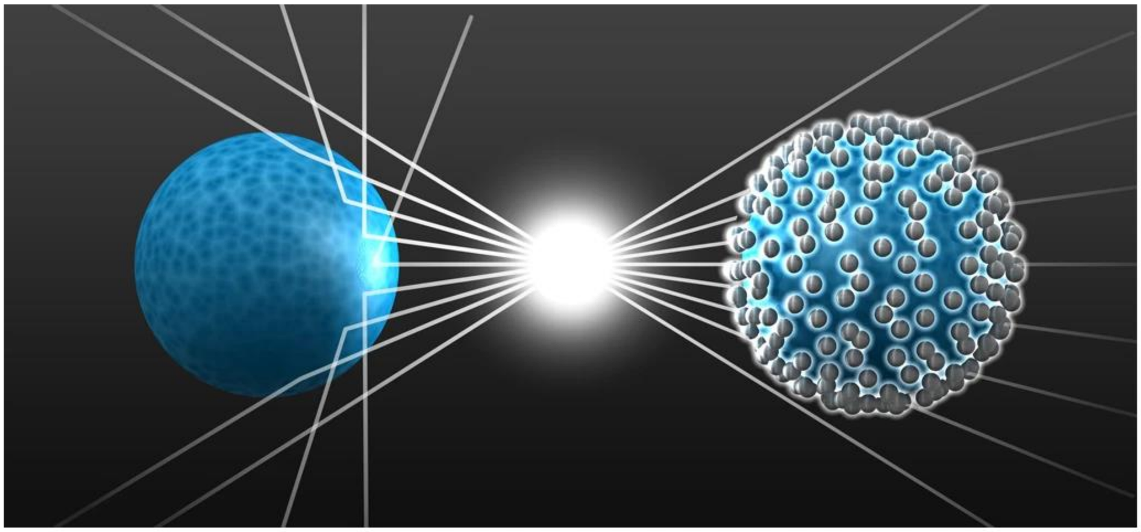

Figure 3.4 Artistic view of the plasmonic cloaking. On the left is a bare dielectric object that reveals its presence and a plasmonic shell covering the dielectric object on the right. The suppression of the scattered light makes the object undetectable. Reproduced with permission from [128] © 2013, Stefan Mühlig et al.

Only a single layer of plasmonic cloaking cover has been shown to reduce the scattering significantly from a couple of multipolar scattering orders [129]. This is cloaking an object on the scale of the wavelength of the operation. Cloaking a larger object and multiband operation can be carried out using multilayered plasmonic cloaking covers[130]. In this case, it will act on more degrees of freedom and suppress a higher scattering order. A plasmonic cloaking cover is easy to fabricate compared to other cloaking methods discussed in previous sections. The plasmonic cloaking method does not require external energy to operate (passive cloaking), which is another advantage. It has been hypothesized that a plasmonic cloaking cover scatters as much light as the target object, but the phase difference is π out-of-phase[128]. As a result, scattered light from the target object and the cloaking cover interferes destructively in the far-field.

A latent quality of this method is the possibility of interaction between the incident wave and the cloaked object, where the system as a whole remains invisible with respect to the incident wave [123]. The other cloaking techniques (transformation, carpet cloak, and mantle cloak) completely isolate the object from the incident wave.

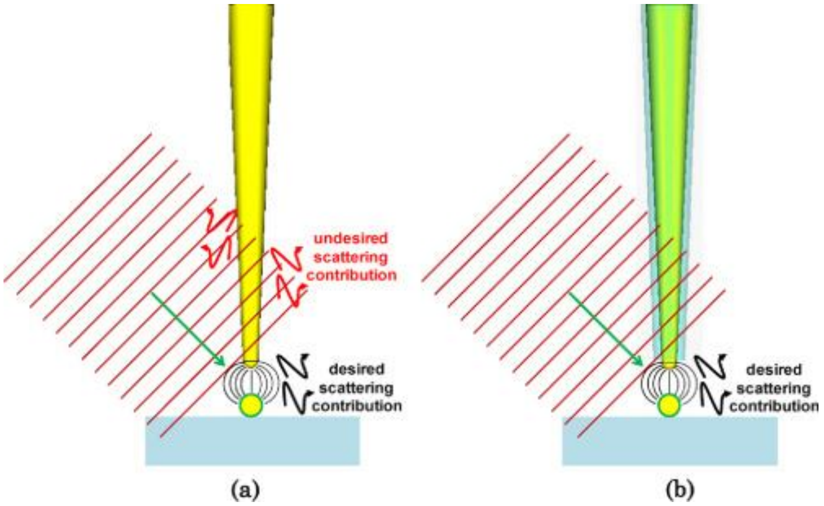

Figure 3.5 Operation of (a) a regular apertureless NSOM tip and (b) an NSOM tip partially covered by a scattering suppression material. Reproduced with permission from reference[131]. © 2011, OSA.

This quality of interaction with the incident wave enables a cloaked object to sense the electromagnetic field around them. As a result, plasmonic cloaking may be applied to sensors in near-field measurements where the presence of such a system creates fewer disturbances to the sensing system [131][132][133]. This cloaked sensor technique becomes very useful in near-field scanning optical microscopy (NSOM) or receiving antennas. Figure 3.5 is a schematic that shows the operation and the advantages of a partially cloaked NSOM tip. A partially cloaked scanning tip reduces unwanted scattering from its presence without interfering with the signal from the sample. Hence it increases the signal-to-noise ratio.

3.2.1 Plasmonic cloaking working principle

Plasmonic cloaking is achieved by suppressing dominant scattering harmonics radiated from the cloaked object[102]. How much scattered filed is generated in each transverse electric (TE), and transverse magnetic (TM) mode is determined by the coefficients C_n^{TE}, and C_n^{TM} [12]. These coefficients do not depend on the excitation wave. Instead, it depends on the object's refractive index, size, surrounding medium, and operating frequency[12]. The scattering cross-section, or the visibility of the object,

$$\sigma_s = \frac{2\pi}{|k_o|^2} \sum_{n=1}^{\infty} \sum_{m=-n}^{n} (2n+1)(|c_{nm}^{TM}|^2 + |C_{nm}^{TE}|^2) \qquad (3.1)$$

Here k_0 is the wavenumber in the background medium. In general, the sum in equation 3.1 is dominant up to a few terms. For an object of characteristic size χ, the only terms $n \approx k_0\chi$ contributes significantly to the scattering waves[134][3]. In more applied cases, the object of interest is considered as an electrically small dielectric object of radius **a**, illuminated by a plane wave. Here the only surviving terms would be $m = 1, n = 1$ in the expansion of equation 3.1[12][3]. These surviving terms indicate scattering or radiation from a dipole. The overall scattering can be reduced or canceled completely by having the core and the plasmonic shell opposite polarizability[124]. Hence, plasmonic cloaking is a scattering cancellation technique where concentric shells of isotropic and homogenous materials are used to suppress each of the dominant terms stated in equation 3.1. Figure 3.6 shows the cancellation of the overall dipole moment through an induced negative polarization vector.

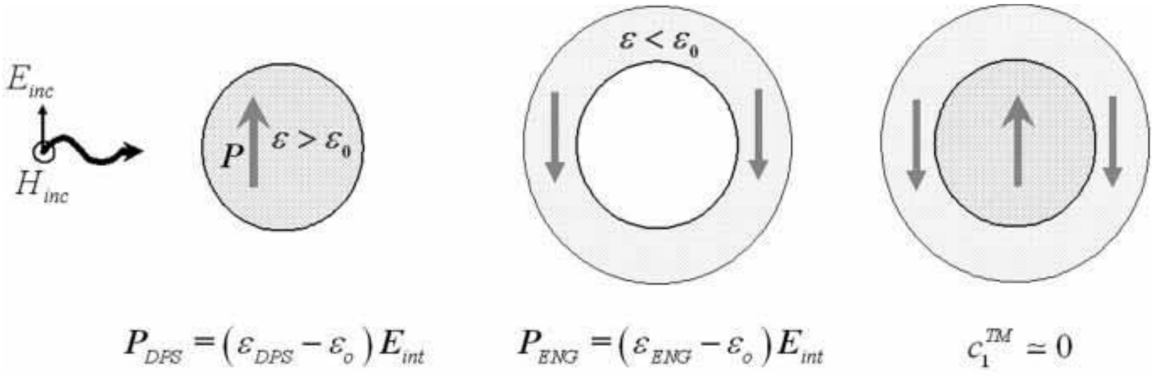

Figure 3.6 Heuristic interpretation of the transparency phenomenon: cancellation of overall dipole moment through an induced negative polarization vector. Reproduced from reference [124] with permission. © 2005, Phys. Rev. E.

In the case of more practical consideration, for cloaking a dielectric sphere with permittivity $\epsilon > \epsilon_0$, the cloak would require $\epsilon \cong 0$. This condition can be achieved by plasmonic material shell or cover. Plasmonic materials have a very small permittivity around the plasma frequency[8][13]. The resulting induced dipole moment in the cloak takes an opposite sign compared with the core dielectric object in the core-shell system. This equal and opposite induced dipole moment precisely compensates each other. This method of cloaking is quite different from any other cloaking method described before. Both the cloak and the target object scatter incident light, and invisibility is obtained by pairing them destructively. As a result, there is zero net-induced dipole moment and dipolar scattering[124]. The cloaking shell can be realized at microwave frequencies using metamaterials and at optical frequencies using noble metals[135][125].

3.3 Limitations of existing cloaking methods

Each cloaking method has some notable advantages or disadvantages. The spherical transformation electrodynamic cloak is an ideal and all-angle cloaking method. A significant limitation of this method is its frequency dependency. In this case, a new cloak needs to be designed and fabricated for each operational frequency. These requirements make the transformation electrodynamic cloak zero bandwidth and highly complicated for fabrication[102]. A potential replacement of the transformational cloaking method was carpet cloaking and its variant. The carpet cloaking method provides a couple of advantages over transformation-based cloaking, such as its applicability to dielectric material and its supports for a wide bandwidth. Carpet cloaking lacks the support for three-dimensional geometry. It can cloak in two dimensions only[102]. Another major disadvantage of carpet cloaking is that it requires a mirror or highly reflecting plane as a supporting background, and it is not an all angle cloaking. Mantle cloaking presents several advantages over transformational electrodynamic cloak, and carpet cloak. It works by canceling dominant scattering harmonics radiated from the target object[102]. The mantle cloak uses an ultrathin frequency-selective surface to induce the surface current. Hence this cloaking method requires FSS to cancel dominant scattering harmonics. The main advantage of mantle cloaking is that it is isotropic, all angle, and can support a reasonable bandwidth. The requirement of FSS is a significant setback of this cloaking method[102].

Plasmonic cloaking is all angle scattering cancellation method. The working concept of this cloaking method has been hypothesized and modeled as a compensating dipole moment of the target object by applying a shell made of plasmonic material having opposite polarizability[124] at the operational frequencies. This method is isotropic, conformal, and can support a reasonable bandwidth. The major disadvantage of plasmonic cloaking is that it is size limited and unable to support a broadband frequency[102][124]. Suppressing scattering by compensating dipole or inducing an opposite dipole to have a net zero dipole moment turns out to be impractical for mesoscale structures[102]. The plasmonic cloaking shell works effectively at or near the plasma frequency, which restricts its bandwidth of operation. Another assumption of this method is that a plasmonic shell and the scattering dielectric core makes an electromagnetically homogenous medium. This composite core-shell structure has been analyzed using effective medium theory or mixing formula such as Maxwell Garnett approximation[136]. Application of effective medium theory and assuming the core-shell as a homogenous structure imposes size and bandwidth constrain on the applicability of plasmonic cloaking[102]. The effective medium theory in plasmonic cloaking and its drawback has been discussed briefly in the following subsection.

3.3.1 Effective medium theory

In 1904 Maxwell Garnett developed a mixing formula that is a simple yet very successful homogenization theory [136]–[138]. This mixing formula is also known as effective medium theory. This theory approximates complex electromagnetic mediums. The Maxwell Garnett mixing formula provides the permittivity of a composite complex medium, or in other words, it gives effective permittivity[137]. Permittivity and volume fractions of each constituent medium are considered for calculating effective permittivity[137].

The core-shell structure in plasmonic cloaking is fabricated with plasmonic nanoparticles (such as silver or gold) as a cloaking cover, and the enclosing objects can be dielectric or metal[128][139]. Each component in such a core-shell structure has different permittivity, and they are often surrounded by air. Altogether, these structures create an effective medium whose permittivity is not the same as any of the constituent mediums. A Maxwell Garnett or Maxwell Bruggeman approximation is the appropriate tool to calculate effective permittivity. Plasmonic cloaking to work, a shell with negative permittivity or close to zero, is required. The effective permittivity of the plasmonic shell can be calculated using the Maxwell-Garnett mixing formula as,

$$\epsilon_{eff} = \epsilon_m \frac{\epsilon_i(\omega)[1+2f]-\epsilon_m[2f-2]}{\epsilon_m[1+f]+\epsilon_i(\omega\,)[1-f]} \tag{3.2}$$

Here ϵ_m is the nondispersive permittivity of the host medium. $\epsilon_i(\omega)$ the permittivity of the nanoparticles and f the filling fraction of the effective medium.
The filling fraction can be expressed as $f = \left(\frac{4\pi}{3}\right)\left(\frac{a^3}{d^3}\right)$. Where a is the radius of the nanoparticles and d is the inter-particle distance. A polarization vector induced by the effective medium $P_s = \epsilon_0(\epsilon_s - 1)E,$ and polarization vector of the bare object $P_c = \epsilon_0(\epsilon_c - 1)E.$ Figure 3.6 shows both polarization vectors, and scattering suppression occurs when these polarization vectors cancel out each other[124][102].

3.3.2 Drawbacks of the effective medium theory

The derivation process of the effective medium theory is not mathematically rigorous. Lorentz local field correction is a prerequisite for this approximation, which relies on integrating the electric field of a dipole over a specific geometry such as sphere or ellipsoid of finite radius[138]. It would be mathematically incorrect to assume that, since the integration converged for some specific region, it would converge over a whole region for any geometry. When integrated over the whole space, the electric field of a static dipole does not converge at all, so any arbitrary deformation in the integration space would yield an arbitrary result[138]. This indicates that the Lorentz local field correction is affected by the geometry. Apart from the drawbacks described above, there are some additional shortcomings while applying this approximation in an experiment. This theory can produce any effective permittivity depending on the filling fraction of arbitrary values between 0 and 1[137]. Such random values of the filling fraction may not be achievable in practical applications. The effective medium theory is a mixing formula that needs to be modified based on the type and number of constituent mediums. In most cases it can account for the host medium but in case of the core-shell structures it does include dielectric core in the calculations [137].

Passive electromagnetic cloaking via scattering suppression is the most promising among all the cloaking methods. Achieving scattering suppression by canceling the resultant dipole arising from the cloak and the target object is inefficient and impractical. It imposes size limitations on the cloaking system. A significant amount of incident power is extinct because of absorption by the encapsulating metallic shell of finite thickness. Apart from the power extinction and size limitation, operational bandwidth is another drawback that makes it unsuitable for real-world applications. Broadband scattering suppression by leveraging the scattering and absorption properties of the plasmonic nanoparticles is a unique and robust method of achieving transparency. This method overcomes some of the major drawbacks of other cloaking methods discussed in this chapter. Development, numerical experiments, and related scattering suppression results are discussed in the following chapter.

Chapter 4

Modeling broadband cloaking using 3D nano-assembled plasmonic meta-structure

The mechanism of achieving broadband scattering suppression using plasmonic meta-structure is explored in this chapter. These meta-structures are composed of a spherical dielectric core coated with gold nanoparticles. The incident light on the structures undergoes multiple scattering and absorption between the dielectric core and nanoparticles. A rigorous model to compute multiple interactions explicitly instead of applying a homogenization theory was developed. A wide variety of cores and metallic nanoparticle combinations were analyzed using this model. This numerical model serves as a scalable and robust simulation platform to characterize and simulate the scattering of the incident electro-magnetic waves by the 3D nano-assembled plasmonic meta-structures.

4.1 Introduction

Advances in nano-synthesis [105], [106], [140] and nano-assembly [141]–[145] have opened up possibilities of many intriguing applications that seek to leverage not just the unique size-dependent properties of single nanoparticles (NPs), but also the collective behavior of ensembles of NPs, which are distinct both from isolated NPs and from their bulk counterparts [146], [147]. One of these is the fabrication of meta-materials using metallic NPs whose interaction with electromagnetic (EM) waves have demonstrated exotic and anomalous phenomena, including 'cloaking' [102], [128], [148]. The fundamental concept allowing for cloaking is the ability of metallic NPs to modify EM waves in the near- and far-field regimes, a characteristic known as plasmonics, which is tunable via NP size, shape, composition, and in an ensemble, inter-NP separation [149]–[157]. This property allows for achieving invisibility via scattering cancellation [108], [125], [158]–[162], a method of passive cloaking which requires no external power. The spectral band over which scattering is suppressed is controlled by the physical properties of the NPs that, in turn, control their plasmonic response. The cloaking technique is based on all angle scattering cancellation using a layer of plasmonic material with low or negative effective permittivity and relies on producing a local polarization that is in "anti-phase" in reference to the target being cloaked. A well-designed cloaking cover may recover the

near- and far-field incident wavefront, and is independent of the incident angle, form and polarization of the incident wave and location of the observer.
The most common type of structure that has experimentally demonstrated significant scattering suppression is a spherical core-shell construct[128][158][163], schematically represented in Fig. 4.1.

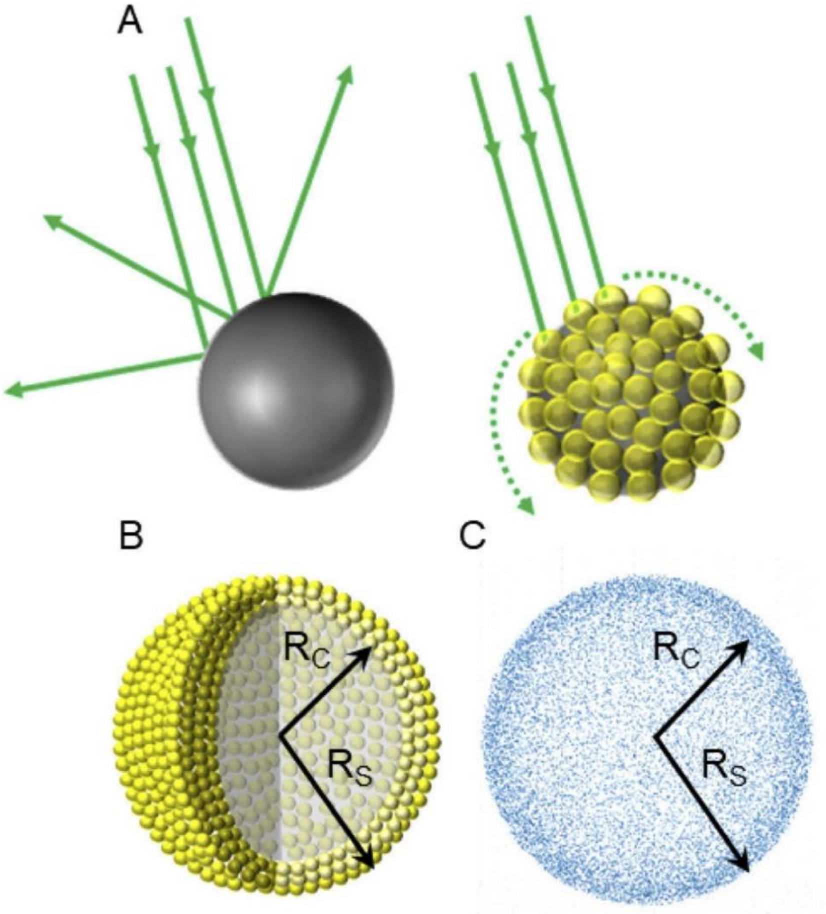

Figure 4.1 Plasmonic cloaking with 3D nano-assembled shells. (a) Schematic depicting the difference of optical scattering from a bare sphere [left] and sphere coated with AuNPs [right] (b) Shell of finite-sized AuNPs of thickness $R_S - R_C$ surrounding the core of radius R_C (c) The corresponding set of point scatterers used in the model. Reproduced with permission from reference [1]. © 2020. OSA.

The core is the target to be cloaked, and the shell consists of an amorphous arrangement of metallic NPs, typically gold or silver. Even a single layer of NPs in the shell has reduced scattering significantly, although the spatial size of the cores cloaked is limited to the subwavelength scale, and the spectral band of operation is relatively narrow – on the order of tens of nanometers. Theoretical predictions [129], [164], [165] have outlined the possibility that multilayered plasmonic covers could extend both the physical scale of targets and the operation wavelength ranges over which they are cloaked. Such structures face both experimental and theoretical challenges, as they are difficult to fabricate and scale up using traditional top-down and bottom-up approaches, and additionally, complicated to simulate, given that the most prevalent approach for the latter is based on a dipole approximation.

We have established a method [166][167] of nano-assembly capable of fabricating multi-layered plasmonic covers in the form of shells. These are 3D hollow constructs whose radii can be tuned from $200\ nm\ - 2\ \mu m$ and whose wall consists of several layers of densely packed AuNPs (see Fig. 4.1 (b)). Effective medium theory [137] is not valid for modeling the multiple and densely packed AuNP layers forming these shells. Instead, a new multiscale modeling and simulation platform is needed to account for the strong multiple interactions of light with the individual AuNPs making up the shell. Additionally, this model must take into account interactions with the core. Because the strong, multiple interactions between the core and the AuNPs are the main mechanisms to be featured in this model, the power scattered and absorbed by the shell due to the optical properties of an individual AuNP needs to be taken into account.

Here, we present a multiscale modeling and simulation platform that satisfies these requirements, and provides valuable insights into the relevant issues, such as the fact that scattering efficiency of a plasmonic cloak is suppressed most when each individual metal NP in the shell scatters and absorbs strongly. As strong multiple scattering in the shell assists with confining power to the shell, it therefore follows that strong absorption in the shell attenuates the overall power scattered by the cloak. Results from our simulations are consistent with this interpretation.

In this model, scattering by the core is computed using the Method of Fundamental Solutions (MFS) [168] or Discrete Source Method [169]. Since the AuNPs are small compared to the wavelength, we model them as point scatterers (see Fig. 4.1(c)) and use the multiple scattering theory of Foldy [170]and Lax [171] to compute multiple scattering by them. We combine these two methods to obtain generalized Foldy-Lax [172] theory for this problem. Using this multiscale simulation platform, we compute the scattering efficiency of a plasmonic cloak for core diameters between 400 nm and 900 nm, gold NPs (AuNPs) with diameters of 5 nm, 10 nm, and 20 nm, and filling fraction of metal NPs in the shell between 0% and 65%. Through these simulations, we show that significant suppression of power is achieved for a broad spectral window from approximately 400 nm to 630 nm depending on the specific parameter values. The remainder of this chapter is as follows. We give a brief description of the method used to fabricate nano-assembled hollow shells composed of densely packed metal NPs in Section 4.2. In Section 4.3 we give the details of the multiscale model used to compute the scattering efficiency of a plasmonic cloak. Included in Section 4.3 is a detailed description of modeling assumptions and choices as well as validation studies. Results from using this model to compute the scattering efficiency for several different plasmonic cloaks is given in Section 4.4. We give our conclusions in Section 4.5. Appendix A gives the details of the model and Appendix B gives the method we use to compute the total scattering cross-section that is used for all the results shown here.

4.2 Design and fabrication

Shell formation is driven by a process reported in our earlier work [166], [167]. This process leverages the phase transition of thermotropic hosts to assemble NPs dispersed in it into three-dimensional (3D) structures. The first step is to modify the surface of the NPs. The native ligands on the NPs are exchanged with custom-designed aromatic molecules, followed by dispersion of the NPs into a liquid crystal (LC) material. We use a commercially available LC, known as 5CB, as the host, and the functionalized NPs are added at 40 C when 5CB is in its isotropic (disordered) phase. This allows uniform dispersion and is followed by decreasing the temperature of the suspension at the rate of 0.5 C/s down to 33 C. 5CB transitions from isotropic to nematic (ordered) phase at 35.5 C, so as the temperature decreases and the LC order parameter increases, it expels the previously well-dispersed NPs into shrinking isotropic domains. This proximity allows the ligands on the NPs to begin the shell formation through an attractive $\boldsymbol{\pi - \pi}$ interaction of their aromatic rings. Once shell formation is complete, the structures are very robust, and impervious to increased temperature. Further, they can be extracted from the host LC and re-dispersed into other optically homogeneous solvents. By a judicious choice of ligands, shell diameters can be controllably tuned from 200 nm to $2\,\boldsymbol{\mu m}$. In addition to this scalability, there are other advantages offered by this novel nano-assembly method. The first is versatility, where NPs of different compositions (including metallic, semiconducting and magnetic) and of a wide range of sizes can be used to form the shells. Therefore, the use of different sizes of AuNPs to allow tuning the operational spectral band with relative ease. The second is the capability of encapsulation offered by this assembly process. An inclusion of choice can be added to the LC medium concurrently with the functionalized NPs, and as the NP-LC composite is cooled, the inclusions are trapped within the shells. Encapsulation of organic fluorescent dye, quantum dots and fluorescent bacteria have been successfully demonstrated [167], and this ability offers an additional degree of functionality not accessible to solid core-shell structures.

4.3 Model

We model the plasmonic cloak as a sphere composed of a uniform dielectric medium (core) surrounded by a random distribution of point scatterers (shell). The key parameters for the core include the diameter *d* and the relative refractive index *m* given as the ratio of the refractive index of the sphere divided by that of the surrounding medium. The key parameters for the shell include the number and positions of point scatterers and their individual optical properties. The number and positions of the point scatterers depend on the shell thickness and the filling fraction. We evaluate the cloaking properties of this structure by computing its scattering efficiency over wavelengths ranging from 400 nm to 700 nm.

The key parameters described above of this model are all elementary quantities. Consequently, this model has no inherent limitations on size or material properties. The key challenge is modeling the strong multiple scattering of light in this system. To simplify the modeling, we use the scalar approximation [[173], Chapter 13]. Even though the scalar approximation does not account for all the physical details in the system, it effectively accounts for the redistribution of power due to the multiple interactions between the core and the surrounding AuNPs, and therefore the overall behavior of the scattered light. For this reason, this scalar theory provides valuable insight into the problem while also keeping the discussion relatively simple.

4.3.1 Mathematical formulation

In what follows, we give a mathematical formulation for scattering by the system comprised of the dielectric spherical core, and the shell composed of randomly distributed metal NPs. This

formulation follows closely with formulations of multiple scattering given by Ishimaru [174], for example. Suppose that the origin of a coordinate system lies at the center of the dielectric sphere. We

denote the interior domain by $D = \{|r| < \frac{d}{2}\}$ and the exterior domain by $E = \{|r| > \frac{d}{2}\}$. The spherical surface $B = \{|r| = \frac{d}{2}\}$ is interface between the interior and exterior. The interior field ψ^{int} satisfies

$$(\nabla^2 + k_1^2)\psi^{int} = 0, \text{ in D}, \tag{4.1}$$

with k_1 denoting the wavenumber for the dielectric sphere. Let N denote the number of point scatterers in the shell. The exterior field, ψ^{ext}satisfies

$$(\nabla^2 + k_0^2)\psi^{ext} = -k_0^2 \sum_{n=1}^{N} V_n \psi^{ext}, \text{ in E}, \tag{4.2}$$

Here, k_0 is the wavenumber for the exterior and V_n corresponds to the scattering potential for the *n*th metal NP. We write ψ^{ext} as the sum $\psi^{ext} = \psi^{inc} + \psi^{s}$ with ψ^{inc} denoting the incident field, and ψ^{s} denoting the scattered field. We must supplement the equations above with conditions on *B* as well as radiation conditions. In particular, we prescribe that

$$\psi^{int} = \psi^{inc} + \psi^{s} \text{ on B},$$
(4.3)

And

$$\partial_v \psi^{int} = \partial_v \psi^{inc} + \partial_v \psi^{s} \text{ on B}, \tag{4.4}$$

with $\boldsymbol{\partial_v}$ denoting the derivative along the normal on B pointing into E. Additionally, we require that $\boldsymbol{\psi^s}$ satisfies the Sommerfeld radiation condition. Equations (1) and (2) along with interface conditions Eqs. (4.3) and (4.4), and the requirement that $\boldsymbol{\psi^s}$ satisfies the

Sommerfeld radiation condition constitute a complete mathematical description of the problem. To compute the fields interior and scattered by the core, we make use of the Method of Fundamental Solutions (MFS) which is also known as the Discrete Source Method. This method was introduced by Mathon and Johnston [168]. It provides an accurate and efficient computational method for solving the full scattering problem [169]. Scattering by the metal NPs in the shell is computed using the self-consistent scattering theory due to Foldy [170] and Lax [171]. By combining these two theories, we arrive at the so-called generalized Foldy-Lax scattering theory introduced by Huang *et al.* [172] to study scattering by a system made up of an extended scatterer surrounded by smaller scatterers. This model contrasts with that by Huang *et al.* in that we use the MFS instead of a boundary integral equation method to model scattering by the extended object which is the core in our model. The details of this method are given in Appendix A. In Appendix B, we show how to compute the total scattering cross-section for the plasmonic cloak using the results from this method.

4.3.2 Modeling assumptions and choices

The key modeling assumption is that each metal NP is small enough that we can approximate it by a point scatterer. A point scatterer has a constant (complex) scattering amplitude, which we denote here by α. Scattering by a point scatterer is isotropic. Hence, its scattering cross-section σ_s is given by

$$\sigma_s = 4\,\pi\,|\alpha|^2 \tag{4.5}$$

Additionally, by the Optical Theorem or forward scattering theorem [2], [3], [173], [175] we have

$$\sigma_t = \frac{4\pi}{k_0}\,Im\,[\alpha], \tag{4.6}$$

It follows that if σ_s and σ_t for an individual metal NP are known. Then

$$\alpha = \left[\frac{\sigma_s}{4\pi} - \left(\frac{k_0\sigma_t}{4\pi}\right)^2\right]^{\frac{1}{2}} + i\,\frac{k_0\sigma_t}{4\pi} \tag{4.7}$$

In our model, we consider the metal NPs in the shell are identical in size and composition, so that there is only one scattering amplitude _ needed for all *N* metal NPs. This assumption is not a restriction of the model. In fact, the details of the method described in Appendix A allow for a polydisperse distribution of metal NPs, each having different scattering amplitudes. Using a monodisperse distribution of metal NPs is a modeling choice based on the fabrication and design of these plasmonic cloaks described in Section 4.2. The ligands described in Section 4.2 may affect the optical properties of the shell and therefore would need to be included in the model. However, experimental measurements have not shown any significant scattering, extinction, or other optical signature from the ligands, over a range of 350 – 800 nm. Therefore, we neglect the ligands here and consider only scattering by the metal NPs as the main mechanism in this model leading to strong, multiple interactions between the core and shell. In the results shown here, we have taken the optical properties for the metal NPs from experiments done on plasmonic film developed for plasmonic and nanophotonic applications. The measurements for gold are taken from Yakubovsky *et al.* [27], and the measurements for silver are taken from McPeak *et al.* [176]. The plasmonic films in those experiments were fabricated depositing polycrystalline grains whose diameter is approximately same as the film thickness. The plasmonic properties and grain diameter motivated us to use dielectric data from these sources. With those data, we compute the scattering cross-section _*s* and the total scattering cross-section $\boldsymbol{\sigma_t}$ used to define $\boldsymbol{\alpha}$ in Eq. (4.7) using Rayleigh scattering theory [175][2], [3]. Finally, these core-shell meta-structures depend on several parameters such as core diameter, NP diameter, shell thickness, volume filling fraction of the NP in the shell, etc. The model described in Appendix A can account for all of these system parameters. Nonetheless, we have chosen to focus here on the specific case in which the shell thickness is three times the constituent metal NP diameter. This modeling choice is based on and consistent with the fabrication and design of the plasmonic cloaks described in Section 4.2. Moreover, it provides a useful restriction allowing for us to study individual system parameters such as the filling fraction, core diameter, and metal NP diameter in a controlled way.

4.3.3 Computational procedure

We give the computational procedure to compute the total scattering cross-section for a plasmonic cloak. This model requires specifying the relative refractive index *m* and diameter *d* of the core, and the diameter of an individual metal NPs. Once those values are specified, we perform the following computational procedure.

1. Compute the scattering and absorption cross-section for an individual metal NP using the experimentally measured optical properties for gold [27]or silver [176]. With those data, we compute the cross-sections for the metal NPs using Rayleigh scattering [2], [3], [175]. Those cross-sections are then used to compute $\boldsymbol{\alpha}$through evaluation of Eq. (4.7).

2. Specify the filling fraction *f* which gives the volume of all *N* metal NPs divided by the volume of the shell. Using that, we compute

$$N = \left\lfloor f \, \frac{volume\ of\ shell}{volume\ of\ metal\ NP} \right\rfloor \tag{4.8}$$

With $\lfloor \boldsymbol{x} \rfloor$ denoting the floor function giving the largest integer that is less than or equal to $\boldsymbol{x}$.

3. Compute the positions of the metal NPs. r_n^{NP} for n = 1, … … ,N. For each metal NP, we compute three pseudo-random numbers: $r, \theta, and\ \varphi$. The radial length r is sampled

uniformly over $R_c \leq r \leq R_s$ with $R_c = d/2$ and R_s denoting the outer radius of the shell set to be three times the diameter of one metal NP (see section 4.3.1). The polar angle θ is uniformly sampled over $0 \leq \theta \leq \pi$, and the azimuthal angle φ is uniformly sampled over $0 \leq \varphi \leq 2\pi$. The coordinate for the center of a metal NP are $x = r\, sin\theta\, cos\varphi, y = r\, sin\theta sin\varphi,$ and $z = rcos\theta$. The algorithm checks positions of subsequent NPs for overlap and vacancy with other metal NPs. If the algorithm detects an overlap, that computed coordinate is discarder and another coordinate is computed. This process of generating non-overlapping coordinate is continued until it finishes generating N positions.

4. Use the Fibonacci lattice[177] to compute boundary points $r_j \in B$ for $j = 1, \dots, M$ and compute r_j^{int} and r_j^{ext} using Eqs. (A2) and (A6) respectively. In our simulations, we have set $M = 512$ and $l = 0.125d$.

5. Solve the linear system comprised of Eqs. (A11) – (A13) with $\psi^{inc}(r) = e^{ik_0\,\hat{z}.r}$ to determine the expansion coefficients c_j^{int} and c_j^{ext} for $j = 1, \dots, M$, and exciting fields, $\Psi_E(r_n^{NP})$ for $n = 1, \dots, N$.

6. Evaluate Eq(B5) at $\hat{\imath} = \hat{o} = \hat{z}$ and use that to compute the total scattering cross-section according to Eq. (B6).

Steps 5 and 6 are repeated for each wavelength sample the spectrum.

There are two parts of this procedure that require the most computational effort. Step 3 for computing the positions of the N metal NPs requires large computational times as N increases because each additional metal NP requires checking for overlap with the previous metal NPs. Future modifications to the computational platform will seek more efficient methods for determining these positions. The other major computational effort is Step 5 which requires solution of the $2MN \times 2MN$ linear system of equations. The corresponding system matrix is dense and full. In the results shown here, we have only used a general Gaussian elimination method to solve this linear system. Therefore, this computation has a complexity of $O(8M^3N^3)$. However, the entries of the system matrix are mostly evaluations of Green's functions which yield an inherent structure in the system matrix that may be exploited for more efficient computations. Future modifications to the computational platform will seek to use state-of-the-art numerical linear algebra methods to make this computation more efficient.

4.3.4 Validation

Before proceeding to simulate the scattering efficiency and suppression of the nano-assembled shell structures, it is important to validate the model. We do so by first studying the accuracy of the MFS in computing scattering by the dielectric core without the shell of metal NPs to demonstrate the high accuracy achieved with this method. For a second validation study, we apply our model to the system studied by Mühlig *et al*[128] . where silver NPs (AuNPs) are used to decorate the surfaces of silica cores to show that the model captures features that are not predicted using Maxwell-Garnett theory. Consider the plane wave $\psi^{inc} = e^{ik_o r.\hat{z}}$ incident on a silica sphere with relative refractive index m = 1.4 and diameter d = 750 nm. For this problem, we can determine the solution of this scattering problem exactly. The scattered field is given as an expansion in Legendre polynomials whose expansion coefficients can be determined analytically. To compute the scattered field using the MFS, we use the method described in Appendix A, but without terms corresponding to scattering by the metal NPs so that $\Psi_n = 0$, identically. This leads to $2M \times 2M$ linear system corresponding to Eqs. (A11) and (A12) with $\alpha_n = 0$. The code used to compute these results along with extensive documentation is available at the GitHub repository. In the left plot of Fig. 4.2 we show the scattering efficiency σ_E defined as the total scattering cross-section σ_t normalized by the geometric cross-section, $\sigma_g = \pi d^2/4$. The solid blue curve is the result from the first 64 terms of the Legendre expansion for the exact solution and the orange circles is the result from the MFS approximation. These results show excellent agreement. In the right plot of Fig. 4.2 we show the relative error made by the MFS approximation. Over the spectral window, we find that the MFS is highly accurate with relative errors less than 0.1%. We have found that the MFS performs consistently well for a broad range of sphere diameters thereby demonstrating its effectiveness in modeling scattering by the core.

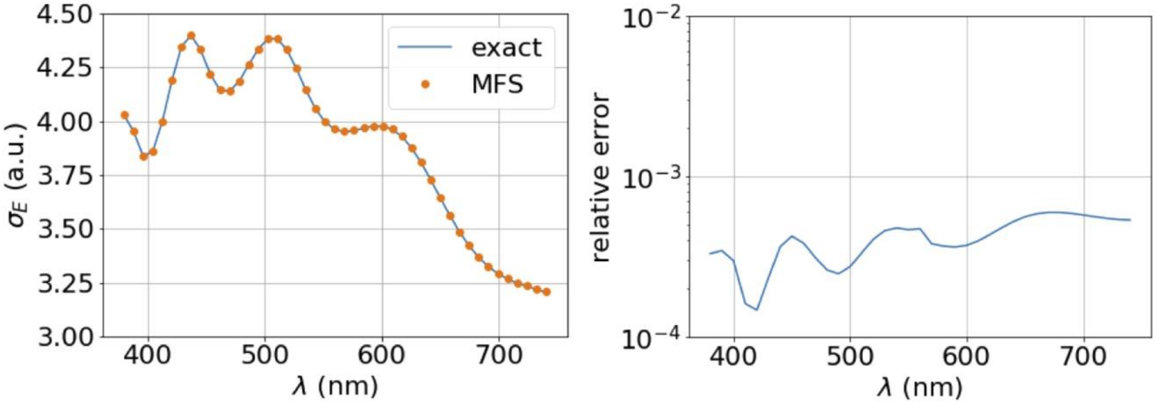

Figure 4.2 Comparison of the exact solution and the MFS approximation for a silica sphere with relative refractive index m = 1.4 and diameter d = 750 nm. The left plot shows the scattering efficiency σ_E given by the total scattering cross-section σ_t normalized by the geometric cross-section $\sigma_g = \pi d^2/4$. The solid blue curve is the result from the exact solution and the orange circles is the result computed using the MFS. The right plot shows the relative error of the MFS approximation. Produced from reference [1] with permission. © 2020, OSA.

For the full model that includes many metal NPs in a shell surrounding the dielectric core, there is no analytical solution available. Instead, we have applied this model to plasmonic cloaks studied experimentally by Mühlig *et al.* [128]. For this comparison, we have used a relative refractive index of $m = 2.18$ and diameter $d = 55$ nm for the silica core. We have used a filling fraction of $f = 10\%$ for the AgNPs on the surface of the core. This comparison was done using only one realization of the AgNPs positions, so no averaging was done to compute the simulation results. No other tuning of our model was done in this comparison study. Figure 4.3 shows the data from the experiment by Mühlig *et al.* [128] (solid squares), where a scattering suppression is observed between 340 – 390 nm, as is expected, given the spectral band of the plasmonic resonance of silver. The calculated values derived from Maxwell-Garnett theory reported by Mühlig *et al.* [128] are also plotted (triangles). According to Maxwell-Garnett theory, the maximum suppression range is 300 – 350 nm, which is blue-shifted from the experimental data. In contrast, the results of our simulation (circles) are in closer agreement to the experimental results.

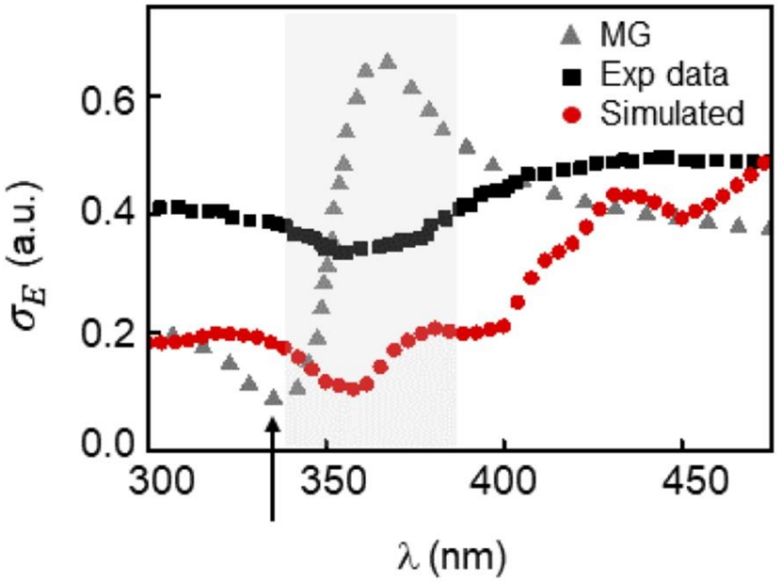

Figure 4.3 Experimental results (Exp data) by Mühlig *et al.* [128] for the scattering efficiency σ_E compared with Maxwell-Garnett theory (MG) and results from our model (simulated). The gray-shaded region highlights the agreement between the experimental results and our model. The arrow indicates the scattering minimum predicted by Maxwell-Garnett theory which, is blue-shifted from the other two results. Reproduced from the reference[1] with permission. © 2020, OSA.

The results shown in Fig. 4.3 demonstrate the usefulness of this new model. It compliments the Maxwell-Garnett approximation by providing a different interpretation for scattering suppression. The fundamental mechanisms in this model is the multiple interactions included between the metal NPs and the dielectric core. Most importantly, it has the capability of scaling up to larger systems without restriction. In what follows, we use this model to study the scattering suppression properties of plasmonic cloaks.

4.4 Results and discussion

In the simulation results that follow, we consider a core made of silica with relative refractive index assumed to be m = 1.4 over the spectral window of 400 nm to 700 nm, and AuNPs with diameters of 5 nm, 10 nm, and 20 nm. The shell thickness is set to be three times the diameter of an individual AuNP and the ligand length is assumed to be 0.98 nm. We show results for different values of the core diameter d and filling fractions f . In particular, we plot the scattering efficiency, σ_E, defined according to

$$\sigma_E = \sigma_t(\lambda)/\sigma_g, \tag{4.9}$$

with σ_g denoting the geometric cross-section. For reference, we compare our results for the results for the scattering efficiency of plasmonic cloak with that for the silica core alone. cross-section for the silica core is $\sigma_g = \pi R_c^2$ with $R_c = d/2$ denoting the core radius, and the geometric cross-section for the plasmonic cloak is $\sigma_g = \pi R_s^2$ with R_s denoting the shell outer radius.

Figure 4.4 summarizes our results for a d = 750 nm silica core covered with plasmonic cloak comprising 10 nm AuNPs of varying filling fraction f. The scattering efficiency for the bare silica core, σ_E^C, shows the characteristic oscillatory behavior seen in Mie theory [2], [3]. The peaks of those oscillations correspond to so-called Mie resonances. The locations and heights of those peaks are characteristic of the size and relative refractive index of the sphere. The scattering efficiency for the core with the plasmonic shell (σ_E^{CS}) composed of 10 nm AuNPs for all f = 0.05, f = 0.10, and f = 0.30 shown in Figs. 4.4(a)–4.4(c) demonstrate a suppression in the spectral range 400 −550 nm where the core -shell composite shows little to no trace of the Mie resonances associated with the silica core. Thus, the spectral signature of the core is effectively removed by the shell of AuNPs. As intuitively expected, the scattering suppression $\Delta\sigma_E$ (defined as $\sigma_E^C - \sigma_E^C$), increases with the filling fraction f.

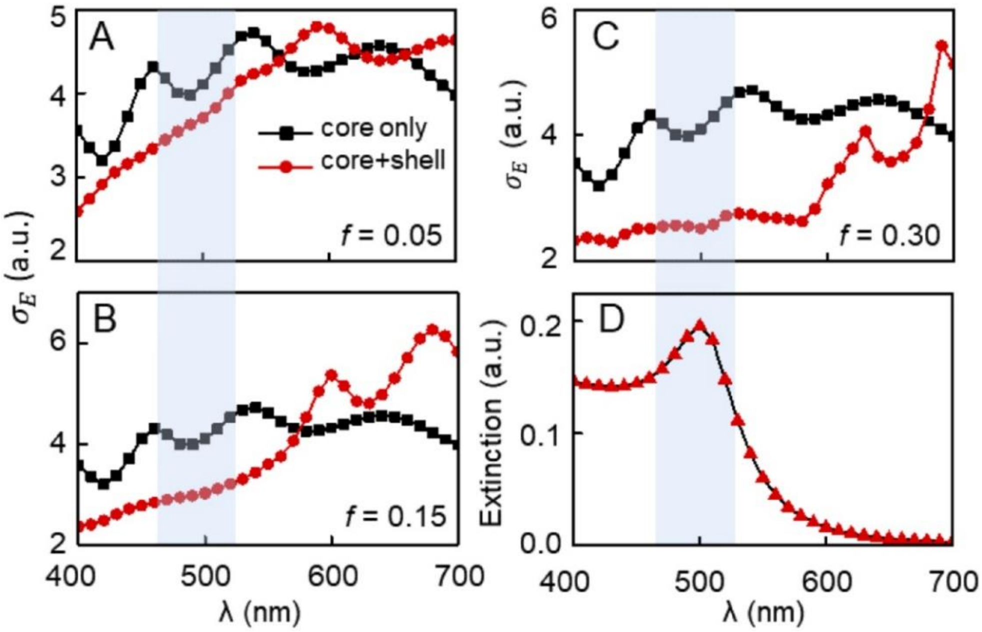

Figure 4.4 Comparisons of the scattering efficiency _*E* for a 750 nm silica core (square symbols) with that for a core and shell (circle symbols) made up of 10 nm AuNPs for filling fractions (a) *f* = 0.05, (b) *f* = 0.15, and (c) *f* = 0.30. The extinction spectrum for a single 10 nm AuNP is shown in (d), with its FWHM band highlighted in blue in (a) - (d). Reproduced with permission from reference [1]. © 2020, OSA

This spectral region over which the plasmonic shell cover suppresses the scattering of the core occurs corresponds closely to the FWHM spectral band of the extinction spectrum of a single AuNP (Fig. 4.4(d) highlighted in blue) highlighting that the main mechanism in this model is the multiple scattering due to the AuNPs and the dielectric core. Consequently, scattering suppression of the plasmonic cloak depends strongly on scattering and absorption by each individual AuNP. When scattering by an individual metal NP is strong, power incident on the shell of AuNPs undergoes strong multiple scattering in the shell. When absorption by each AuNP is also strong, this strong multiple scattering effectively yields higher absorption of the overall power. Thus, strong scattering creates multiple interactions with strong absorbing AuNPs thereby yielding a suppression in power scattered by the plasmonic cloak. Figure 4.5 shows results that compare plasmonic cloaks with 5 nm and 20 nm AuNPs for the same 750 nm diameter silica core. Recall that the shell thickness is set to be three times the diameter of the AuNP. Thus, for the 5 nm diameter AuNP, the shell thickness is 15 nm and for 20 nm diameter AuNPs, the shell thickness is 60 nm. It then follows that the filling fraction sets the corresponding number of AuNPs contained in the shell. In Fig. 4.5 the black curves with square symbols show the scattering efficiency for the silica core, the green curves with triangle symbols show the scattering efficiency for the plasmonic cloak made up of 5 nm diameter AuNPs, and the blue curves with diamond symbols show the scattering efficiency for the plasmonic cloak made up of 20 nm diameter AuNPs. Figure 4.5(a) is for filling fraction *f* = 0.10 and Fig. 4.5(b) is for filling fraction *f* = 0.30. Figure 4.5(c) shows the extinction for an individual 5 nm diameter (green curve) and 20 nm diameter AuNP (blue curve). Because Fig. 4.5(c) shows that the extinction for the 20 nm diameter AuNP is relatively larger than that for the 5 nm diameter AuNP, we expect that the scattering suppression by the plasmonic cloak made up of 20 nm diameter AuNPs to be greater than that for a plasmonic cloak made up of 5 nm diameter AuNPs. The results in Figs. 4.5(a) and (b) show this to be the case. We observe substantially more suppression of scattering using the 20 nm diameter AuNPs in comparison with the 5 nm AuNPs for both f = 0.10 and f = 0.30. For the larger filling fraction, we find that the 20 nm diameter AuNPs suppress scattering across the entire spectral range. The results in Figs. 4.4 and 4.5 indicate that the plasmonic cloaks effectively suppress scattering over a broad spectral range. The amount of scattering suppression depends strongly on the filling fraction. To study the dependence on the filling fraction, we show in Fig. 4.6 a map of the scattering suppression $\Delta\sigma_E$. Here, the plasmonic cloak is made up of 10 nm AuNPs. Thus, when $\Delta\sigma_E > 0$, it implies that incorporating the plasmonic shell cover reduces scattering from the core, and that cloaking is successful. And when $\Delta\sigma_E < 0$, it signifies that scattering efficiency of the bare silica core is higher than the silica core-shell composite. The dark regions of Fig. 4.6 show where the plasmonic cloak is effective in suppressing scattering. These results show that both the magnitude of $\Delta\sigma_E$ and its operational spectral band are enhanced as the filling fraction increases. Indeed, we observe that the onset of cloaking begins around a small value of $f \geq 25\%$ and rapidly improves thereafter. Figure 4.7 maps $\Delta\sigma_E$ for different core diameters ranging from 400 nm to 900 nm. For these results, the plasmonic cloak is made up of 10 nm AuNPs and the filling fraction was held fixed at f = 0.30. For all of the silica core diameters shown here, we observe significant scattering suppression. An important point to note is that the ratio of the radius of AuNPs to the shell thickness is the same for all cases. This implies that, as the cores get larger, the ratio of shell wall to core-shell diameter decreases. This agrees with our experimental platform. Further, $\Delta\sigma_E > 0$ for the entire range of core sizes leads to the conclusions that not only does a plasmonic shell successfully cloak cores with $d\sim\lambda$ but in addition, do so without requiring the need to add more AuNP layers.

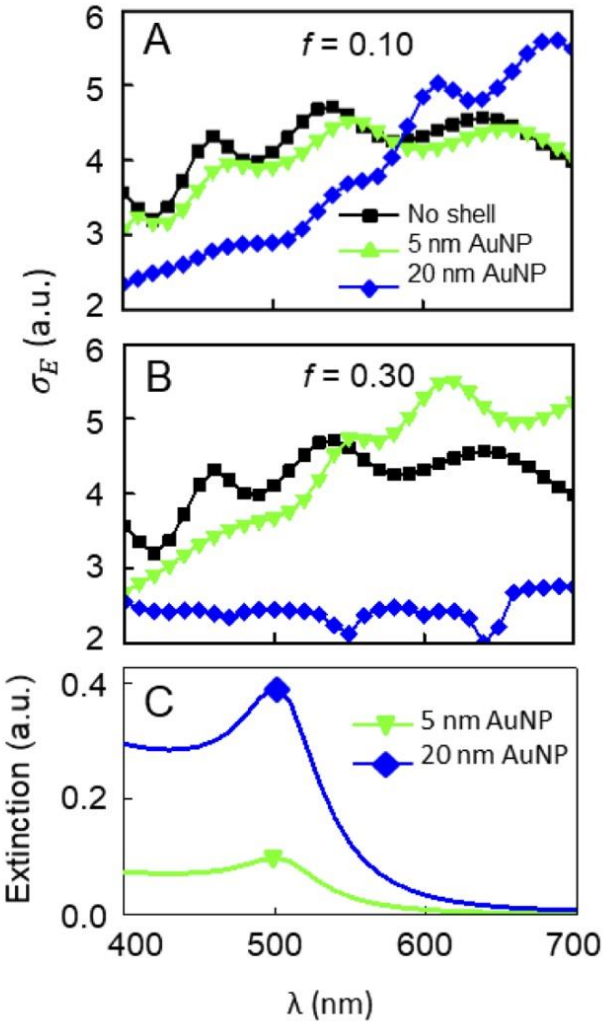

Figure 4.5 Comparisons of the scattering efficiency σ_E for a 750 nm silica core (square symbols) with that by a core and shell made up of 5 nm AuNPs (triangle symbols) and 20 nm AuNPs (diamond symbols) for filling fractions (a) f = 0.10, and (b) f = 0.30. A comparison of the extinction for single 5 and 20 nm AuNP is shown in (c). Reproduced with permission from reference [1]. © 2020, OSA

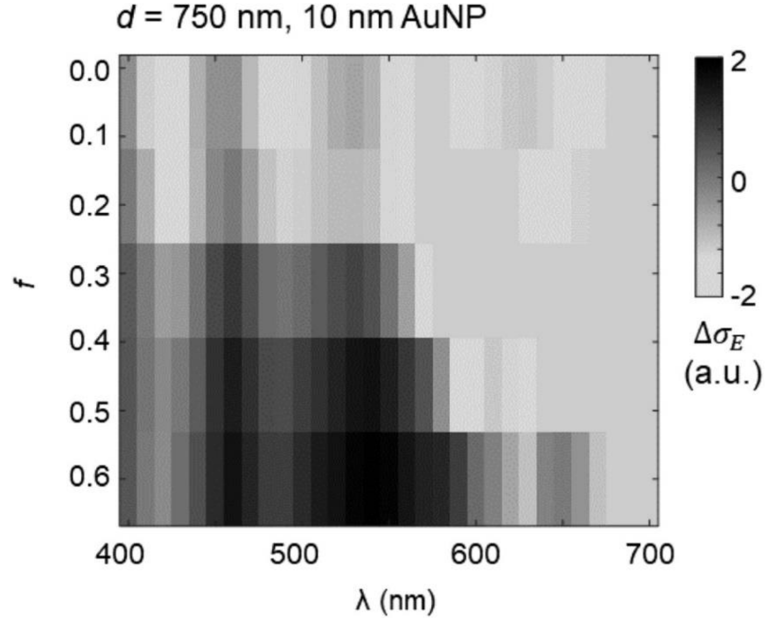

Figure 4.6 A plot of the scattering suppression (scattering efficiency of silica core minus scattering efficiency of plasmonic cloak) as a function of filling fraction f and wavelength λ for a core diameter of 750 nm and AuNPs with diameter 10 nm. Reproduced with permission from reference [1]. © 2020. OSA

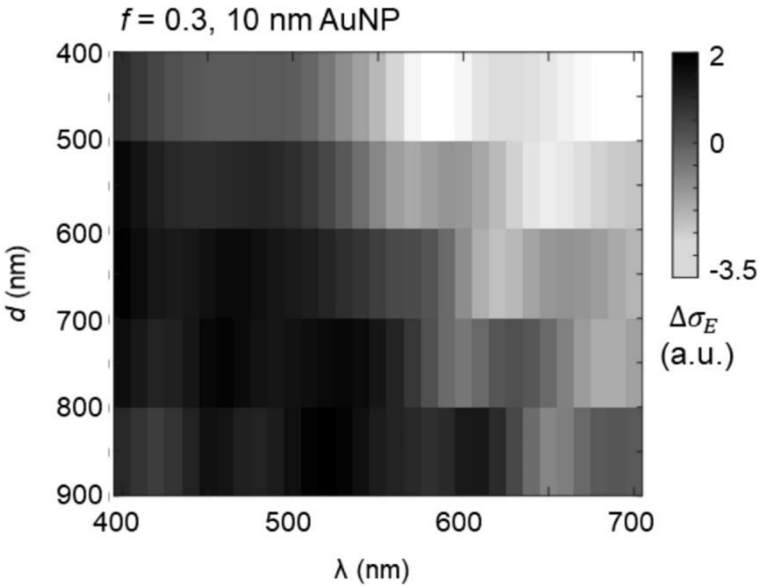

Figure 4.7 A plot of the scattering suppression as a function of core diameter d and wavelength λ for a filling fraction of $f = 30\%$ and AuNPs with diameter 10 nm. Reproduced with permission from reference [1]. © 2020. OSA

4.5 Conclusions

We have developed a computational platform to study plasmonic cloaking structures composed of a core surrounded by a shell of AuNPs. This model uses fundamental quantities such as the scattering and absorption cross-sections of the AuNPs and the material properties of the core by combining the Method of Fundamental Solutions to compute scattering by the core with Foldy-Lax theory to compute multiple scattering by the AuNPs. It also takes into account strong multiple interactions between the core and the AuNPs, which is essential for understanding complex plasmonic cloaks composed of multiple layers of NP coverings. And while it is limited because it uses the scalar approximation and a point scatterer assumption for the AuNPs, it nonetheless provides a useful tool for studying broadband 3D plasmonic cloaking. Simulations results presented confirm that plasmonic NPs can be used to design cloaks in the visible part of the EM spectrum, and along with suppressing scattering over a broad spectral range, AuNPs robustly cloak silica cores as large as 900 nm, larger than the wavelength of operation. Additionally, as the core size increases, cloaking is successful without a subsequent increase in the layers of AuNPs, as shown by the suppression via a constant filling fraction.

4.6 Funding and acknowledgement

National Science Foundation (CHE-1752821, DMS-1819052, DMS-1840265, HRD-1547848);
Air Force Office of Scientific Research (FA9550-17-1-0238, FA9550-18-1-0519).

Chapter 5

Engineering spectral and spatial scattering profiles in the visible spectrum using nanoplasmonic mesoscale assemblies

This chapter of the dissertation presents some of the consequences of scattering suppression using plasmonic meta-structures The scattering of electromagnetic waves by an obstacle can be thought of as an angular redistribution of the incident energy carried by the wave. Total scattering suppression was achieved by the plasmonic meta-structures by leveraging strong multiple scattering and absorption between the nanoparticle shell and the dielectric core. As a result of this multiple scattering and absorption spectral and spatial properties of the scattered light are altered. Angular redistribution of the spatial and spectral profiles was studied in terms of differential cross-section and anisotropy of the scattering pattern. A study of the far-field diffraction pattern and the scattering anisotropy revealed how these two properties are tunable by varying gold nanoparticle diameter and wavelength of the incident light.

5.1 Introduction

Metallic nanoparticles (NPs) couple to and modulate electromagnetic waves through the phenomenon of localized surface plasmon resonance (LSPR) [14], [88], [178]–[180], which make them highly suitable as building blocks for designer optical and photonic meta materials [181]–[184] Some novel functionalities demonstrated by nanoplasmonic constructs include extraordinary transmission, optical magnetism, and photonic lensing [185]–[191]. As in all cases of nano-assembly, these hierarchical structures can be constructed using top-down or bottom-up methods. The latter approach offers greater flexibility in terms of composition and morphology of the constituent NPs, while also providing a route towards generating large scale structures, extending from the nano to the mesoscale and beyond [155][192][193]. Colloidal techniques, such as polymer templating, DNA-ligation, or thermotropic phase transition driven directed assembly are some of the few methods that have produced meta structures comprised of metallic NPs with tailored permittivity, photoconductivity, LSPR tuning and passive cloaking via scattering suppression [155][192] [123], [194]–[197].

Regardless of assembly method, a robust model capable of accurate prediction of structure function correlations is needed to transition these techniques from a laboratory setting to a standard manufacturing set-up for developing novel multifunctional metamaterials. However, bottom-up assembly results in structures with inherent randomness possessing only short-range order, adding complexity to any modeling platform. Accounting for the multiple length scales involved (incident wavelength, NP dimensions, near- and far-field regimes) when plasmonic behavior is at play places even greater demand on the sophistication of the required model. Most computational approaches either consider the nano assembled structure as a homogenous medium (effective medium theory) or focus on phase matching of the incident and scattered fields (anomalous diffraction theory) [155][194] [137][198]. These have been only moderately successful in modeling the broadband response of plasmonic metastructures and have been unable to breach the gap between theory and experiment. What is required is a multi-scale model that can handle not only near-field interactions arising from local NP arrangements, but additionally allow extension to far-field regimes, particularly when the assembled ensembles approach the mesoscale. In this work, we model three-dimensional cloaked targets constructed via directed assembly of gold nanoparticles (AuNPs) that form a cover around a dielectric core. Instead of homogenizing this composite, we explicitly consider the multiple interactions between the core and the nanoassembled cover, which allows us to accommodate a broad range of system sizes with core diameter between $400 - 800$ nm. Composite structures such as these have the potential for cloaking in the visible and near infra-red spectral regions, and here, we confirm the viability of broadband scattering suppression in the visible regime. More importantly, we show that these structures can transfigure scattering patterns with spectral selectivity.

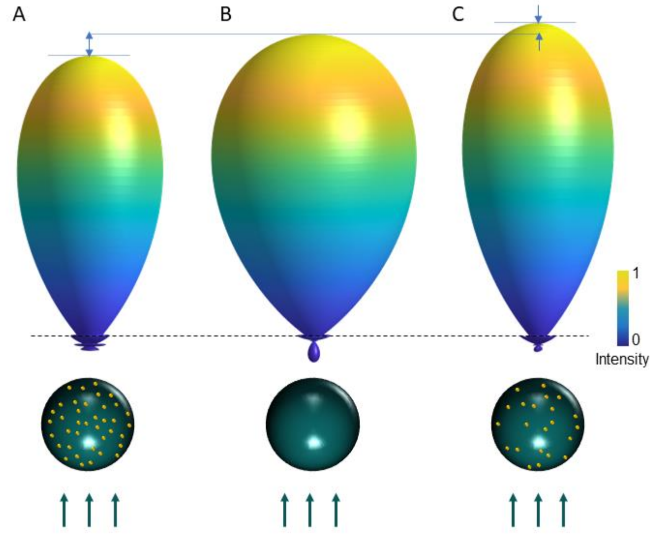

Figure 5.1 3D Deferential cross-section of a 750 nm diameter silica core covered with 10 nm AuNPs at filling fractions (A) $f = 0.3$, (B) $f = 0$ (corresponding to a bare core), and (C) $f = 0.1$.

We further identify two non-dimensional quantities, the albedo, and the anisotropy factor, that characterize relative amounts of absorption and scattering, and the scattering anisotropy, respectively, and demonstrate that, by varying AuNP sizes (5, 10 and 20 nm) and filling fractions (0.1−0.3) in the cloak, scattering intensity can be suppressed or enhanced, while reducing scattering anisotropy in both cases. To calculate the filling fraction f , we consider a `shell' around the core, with thickness equivalent to a single AuNP diameter, and f is defined as the fraction of the shell volume occupied by all the AuNPs. In other words, it is a measure of the surface coverage density. Figure 5.1 shows the simulated three-dimensional differential scattering cross-sections of a bare silica core, and cores with 10 nm AuNPs on their surfaces with varying f. A smooth and spherical dielectric core has no absorption in the visible wavelength range, so any extinction of power is solely due to scattering. By contrast, AuNPs have an appreciable amount of scattering and absorption in the same spectral range. Therefore, while all three cores exhibit a strong forward-scattering peak above the dashed line (indicating their positions) we observe two key differences. The first is the change in the magnitude of the forward scattering peak, which is suppressed at filling fraction f= 0.3 (Figure 5.1A) but enhanced at f = 0.1 (Figure 5.1C), compared to the bare core (Figure 5.1B), indicating variation in the overall power scattered by the AuNP cloaks. The second difference is that for both coated cores, the forward scattering peaks are narrower, and backscattering is suppressed compared to the bare core, implying that the scattered power is preferentially focused in the forward direction with the addition of the cloaks.

5.2 Scattering and absorption by a gold nanoparticle

We begin with a discussion of the scattering and absorption when a monochromatic plane wave is incident on a single AuNP, as those form the basis of how the ensemble of AuNPs in the cloak ultimately behaves. Additionally, we make the scalar approximation in what follows because the model for the coated core includes strong multiple scattering by the AuNPs, which would lead to a negligible degree of polarization of the scattered light.

Consider the observation of the scattered filed U_s at distance R away from an AuNP with $R > d^2/\lambda$ where d is the AuNP diameter and λ the wavelength of the incident light. For this case, the scattered filed behaves according to [174],

$$U_s(R\hat{s}) = F(\hat{o},\hat{\imath})\frac{e^{ikR}}{R} \tag{5.1}$$

where, $\hat{o}$ is the direction of observation, $\hat{\imath}$, the propagation direction of the incident plane wave, and $k = 2\pi/\lambda$, the wavenumber. We call F the complex scattering amplitude. It contains the amplitude and phase of the scattered filed in the far-field. We introduce the differential scattering cross-section σ_d defined in terms of F as:

$$\sigma_d(\hat{o},\hat{\imath}) = |F(\hat{o},\hat{\imath})|^2 \tag{5.2}$$

The scattering cross-section σ_s characterizes the observed scattered power, and the absorption cross-section σ_a characterizes the total absorbed power. The total cross-section is the sum, $\sigma_t = \sigma_s + \sigma_a$. In terms of σ_d the scattering cross-section is defined as

$$\sigma_s = \int_{4\pi} \sigma_d d\Omega, \tag{5.3}$$

where this integral is taken over all directions corresponding to the unit sphere.

According to the Optical theorem[173], we have

$$\sigma_t = \frac{4\pi}{k}\, Im\, [F(\hat{\imath}, \hat{\imath})]. \tag{5.4}$$

Upon computing σ_s and σ_t, we compute $\sigma_a = \sigma_t - \sigma_s$ to determine the absorption cross-section.

Using these cross-sections we compute the scattering efficiency, σ_E, and the albedo, ϖ_0. The scattering efficiency σ_E is σ_s normalized by the corresponding geometric cross section, $\sigma_g = \pi d^2/4$. The albedo is defined as

$$\varpi_0 = \frac{\sigma_s}{\sigma_t} \tag{5.5}$$

When $\varpi_0 = 1$, extinction is due entirely to scattering, and when $\varpi_0 = 0$, extinction is due entirely to absorption. It is therefore a measure of what proportion of the extinction is a result of scattering versus that of absorption.

We compute the total extinction (scattering plus absorption) and albedo (ϖ_0) for in-dividual AuNP with diameter $d = 5, 10,$ and 20 nm (Figure 5.2 A and 5.2 B) using experimentally measured optical properties [27]. Comparing the relative values of both parameters (Figure 5.2 C) shows that 5 nm AuNPs have a relatively low albedo while the albedos for 10 nm and 20 nm AuNP are higher. In other words, we confirm that 5 nm AuNPs have the highest absorption while 20 nm AuNPs scatter most strongly over the visible spectrum.

5.3 Modeling the mesoscale cores with nanoplasmonic covers

In our computational model [1], the scattered and interior fields for the core are computed using the Method of Fundamental Solutions (MFS), otherwise known as the Discrete Source Method[168]. Multiple scattering and absorption by the AuNPs is computed using the self-consistent scattering theory developed by Foldy[170] and Lax[171]. It follows that the complex scattering amplitude for the AuNP-coated core is given by

$$F(\hat{o},\hat{\imath}) = \frac{1}{4\pi}\sum_{j=1}^{M} c_j^{ext} e^{ik_0\hat{o}.r_j^{ext}} + \frac{1}{4\pi}\sum_{n=1}^{N} \alpha_n e^{ik_0\hat{o}.r_n^{NP}} \Psi_E(r_n^{NP}), \tag{5.6}$$

where k_0 is the wavenumber for the surrounding medium. The first sum in Equation (5.6) represents the contribution from the core and the second sum that of the AuNP cover. For the first term, the sum is taken over the M discrete source points at positions r_j^{ext}, for $j = 1, \dots, M$. The coefficients c_j^{ext} for $j = 1, \dots, M$ give the individual strengths of each of the discrete sources. Those coefficients depend on the incident direction, $\hat{\imath}$. In the contribution due to the AuNP cover, the sum is taken over the N AuNPs centered at positions r_n^{NP} for $n = 1, \dots N$. Here, α_n is the complex scattering amplitude for the nth AuNP, which is computed using its individual absorption and scattering cross-sections. We denote the field exciting the nth AuNP by $\Psi_E(r_n^{NP})$, which depends on the incident direction $\hat{\imath}$. The coefficients c_j for $j = 1, \dots, M$ and exciting fields $\Psi_E(r_n^{NP})$ are computed through the solution of a linear system resulting from requiring that fields and their normal derivatives are

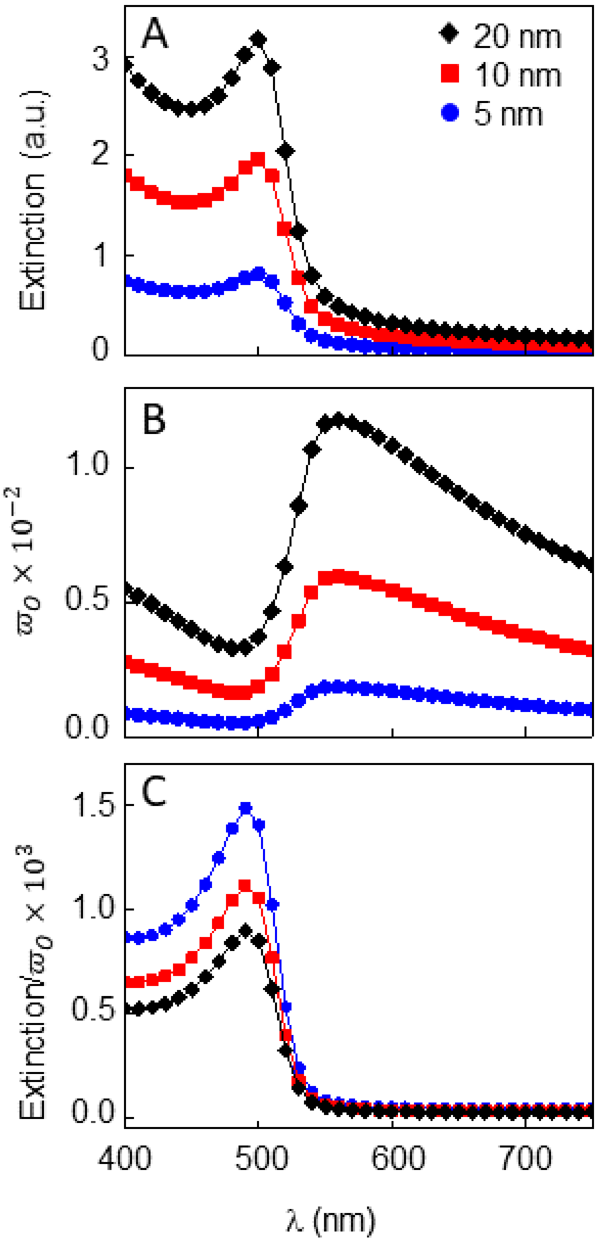

Figure 5.2: (A) Extinction (absorption plus scattering), and (B) Scattering albedo of single AuNPs of different diameters (C) Ratio of extinction to albedo, which indicate that absorption contributes more to the total extinction with decreasing AuNP size.

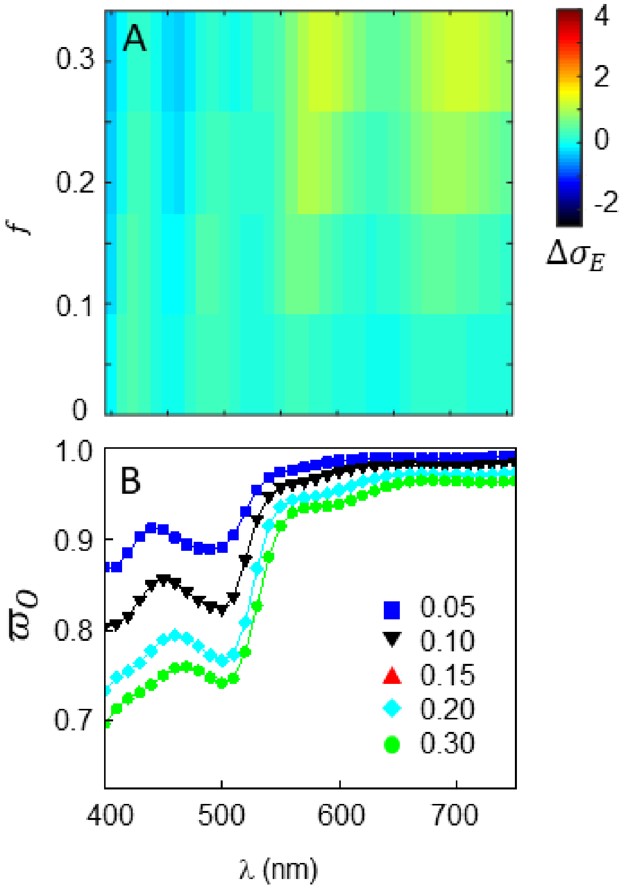

Figure 5.3: (A) Scattering efficiency change $\Delta\sigma_E$ in a 750 nm silica core with 5 nm AuNP cover mapped with incident wavelength λ and filling fraction f. Negative values of $\Delta\sigma_E$ indicate the AuNP cloak lowers scattering compared to the bare core while a positive value indicates enhanced scattering. (B) Scattering albedo for the same core at different f. Scattering albedo of 5 nm AuNP coated structures as f is tuned from 0.05 to 0.30. The monotonic decrease in ϖ_0 with increasing f indicates a steady increase of absorption of incident power as more AuNPs are added to the core surface. Taken together, these indicate a lack of strong and complex optical interactions between the AuNPs and the core, which in turn, lead to no significant scattering suppression and only minor hints of enhancement in the map in part (A).

continuous on the surface of the core[1]. Upon computing Equation (5.6), we determine σ_t using Optical Theorem given in Equation (5.4). To compute σ_s, we introduce a spherical coordinate system in which $\hat{\imath}$ is the north pole.

We denote the cosine of the polar angle by $\mu = \hat{o}.\hat{\imath}$, and the azimuthal angle by φ. In terms of μ and φ, we have

$$\hat{o}(\mu,\varphi) = \left(\sqrt{1-\mu^2}cos\varphi, \sqrt{1-\mu^2}sin\varphi, \mu\right) \tag{5.7}$$

We compute the scattering cross-section using the Q-point product Gaussian quadrature rule on the sphere [199] as ,

$$\sigma_s = \int_0^{2\pi}\int_{-1}^{1}|F(\hat{o}(\mu,\varphi),\hat{\imath})|^2 d\mu d\varphi \approx \frac{\pi}{Q}\sum_{p=1}^{2Q}\sum_{q=1}^{Q} w_q\left|f\left(\hat{o}\left(\mu_q,\varphi_p\right),\hat{\imath}\right)\right|^2 \tag{5.8}$$

where, μ_q and w_q for $q = 1, \dots, Q$ are the Q-point Gauss-Legendre quadrature points and weights, respectively, and $\varphi_p = (p-1)\pi/Q$ for $p = 1, \dots, 2Q$. With σ_t and σ_s computed, we computed the albedo through evaluation of Equation (5.5). We can use this same quadrature rule to compute an anisotropy factor g, though evaluation of

$$g \approx \frac{1}{\sigma_t}\frac{\pi}{Q}\sum_{p=1}^{2Q}\sum_{q=1}^{Q} w_q\mu_q|F(\hat{o}\left(\mu_q,\varphi_p\right),\hat{\imath}|^2 . \tag{5.9}$$

This nondimensional quantity gives a measure of the amount of power flow in the forward direction that is retained after scattering. When $g = 0$, scattering isotropic and when $g = 1$, it is purely in the forward direction.

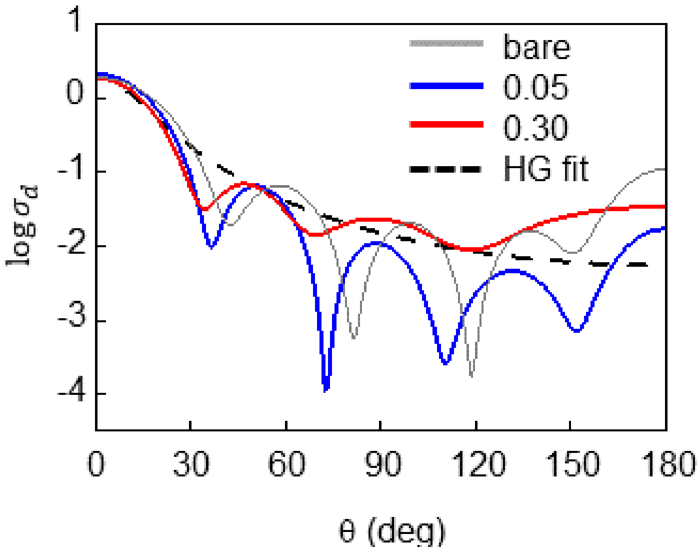

Figure 5.4. Differential scattering cross-section (log-scale) of a 750 nm core at incident λ = 500 nm at different f of 10 nm AuNPs. The fit to the anisotropy data at $f = 0.3$ is the Henyey-Greenstein (HG) scattering model discussed in the text. The fit returns g values of 0.71, 0.75 and 0.76 for $f = 0, 0.05$, and 0.3, respectively.

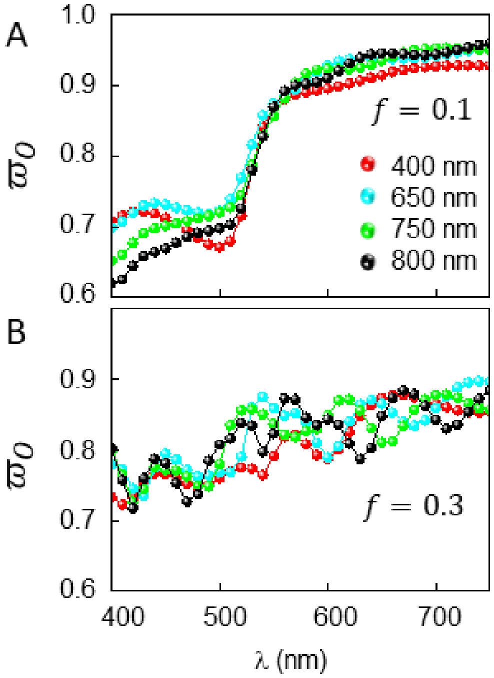

Figure 5.5: Scattering albedo ϖ_0 for different core sizes coated with 20 nm AuNP at (A) $f = 0.1$, and (B) $f = 0.3$. The f dependent ϖ_0 consistently shows the functional form observed in Figure 5.7C in the main text. Low f shows absence of oscillatory behavior in the variation of ϖ_0 with λ. ϖ_0 shows oscillatory feature at high f with the change of λ, indicating strong and complex interaction between the dielectric core and the AuNP cover leading to either scattering suppression or enhancement for a wide range of core sizes.

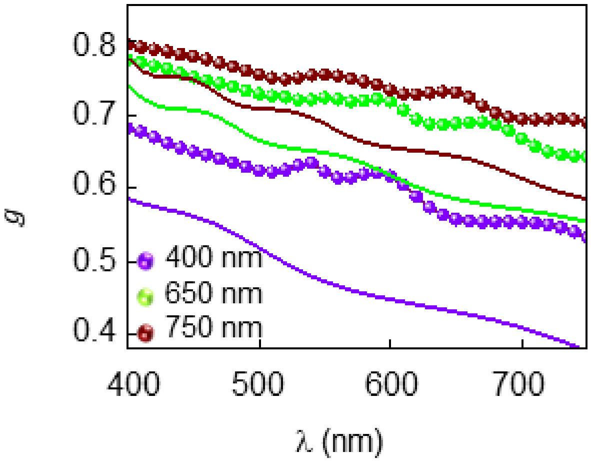

Figure 5.6: H-G fitted anisotropy factor g of 10 nm AuNP coated cores of different diameters at $f = 0.3$. Solid lines correspond to the bare cores and filled circles to the coated cores for each corresponding color. Addition of the cloak increases g over the entire spectral range for all core sizes but the extent to which g changes is more prominent as core sizes decrease.

5.4 Results

For our results we have used M = 512 discrete source points for the core. The number N of AuNPs used depends on the λ filling fractions [1] in each case. To compute σ_s and g, we set Q = 512 for the product Gauss quadrature rule.

In Figure 5.4 we show our computed results for the differential cross-section, σ_d for a 750 nm diameter core when bare, and when coated with 10 nm AuNPs at filling fractions $f = 0.05$ and $f = 0.3$. We plot the azimuthal average of σ_d as a function of the polar angle θ defiend with respect to the propagation direction of the plane wave incident on the target. Due to multiple scattering by the AuNPs on the surface, we expect an overall decrease in coherence in the scattered _field. As a result, the angular side lobes, that are characteristic of diffraction by a bare core, are shifted and suppressed. In other words, we find that σ_d is smoother for the coated cores compared with the bare one, and the smoothing is enhanced as f increases. In light of this, we consider the well-known Henyey-Greenstein (HG) scattering model [200] which defines σ_d as:

$$\sigma_d^{HG}(\theta) = \frac{\sigma_s}{4\pi} \frac{1-g^2}{(1+g^2-2g\cos\theta)^{3/2}} \tag{5.10}$$

Where σ_s and g are the only free parameters. HG has been extensively used to study multiple scattering by particles in radiative transfer theory[175]. In fact, it is often used as a simplified model for a dielectric sphere. Because coated cores have smoother σ_d than the bare core, HG is an appropriate model to use here. In Figure 5.4, this fit to the $f = 0.3$ results is shown as a dashed black curve. We use this fitted value for g to evaluate differences in angular distribution of scattered power for different structures as core size, AuNP size, and filling fraction f is varied.

Figure 5.7 summarizes the effect of AuNP size and f on the scattering efficiency σ_E , HG-fitted anisotropy factor g, and scattering albedo ϖ_0 of the coated cores over the visible spectrum. For all of these results, the diameter of the core is 750 nm and the diameter of the AuNPs is 20 nm. Figure 5.7A shows a color contour plot for the difference of scattering efficiency denoted by σ_E with f varying from 0.0 to 0.3. $\Delta\sigma_E$ is calculated as the difference of scattering cross sections of the coated core with respect to the bare one. Therefore, a negative value of $\Delta\sigma_E$ implies scattering suppression when the AuNP cloak is present. The region of scattering suppression is highlighted by a white dashed rectangle, and corresponds to a broad range of f and a wide spectral window. When $\Delta\sigma_E$ is positive, the coated core has a higher scattering efficiency than the bare core e.g. scattering enhancement occurs on adding the cloak. A black dashed rectangle encloses this region. From these results, we find that scattering suppression is achieved for $f > 0.2$ over the wavelength range 400 nm - 670 nm, while for $0 < f < 0.2$ scattering is enhanced over the wavelength range 600 nm - 750 nm. Figure 5.7B shows results for HG-fitted g for the same core as a function of incident wavelength for different values of f. We expect g to increase as λ decreases since the core size and λ become comparable to one another.

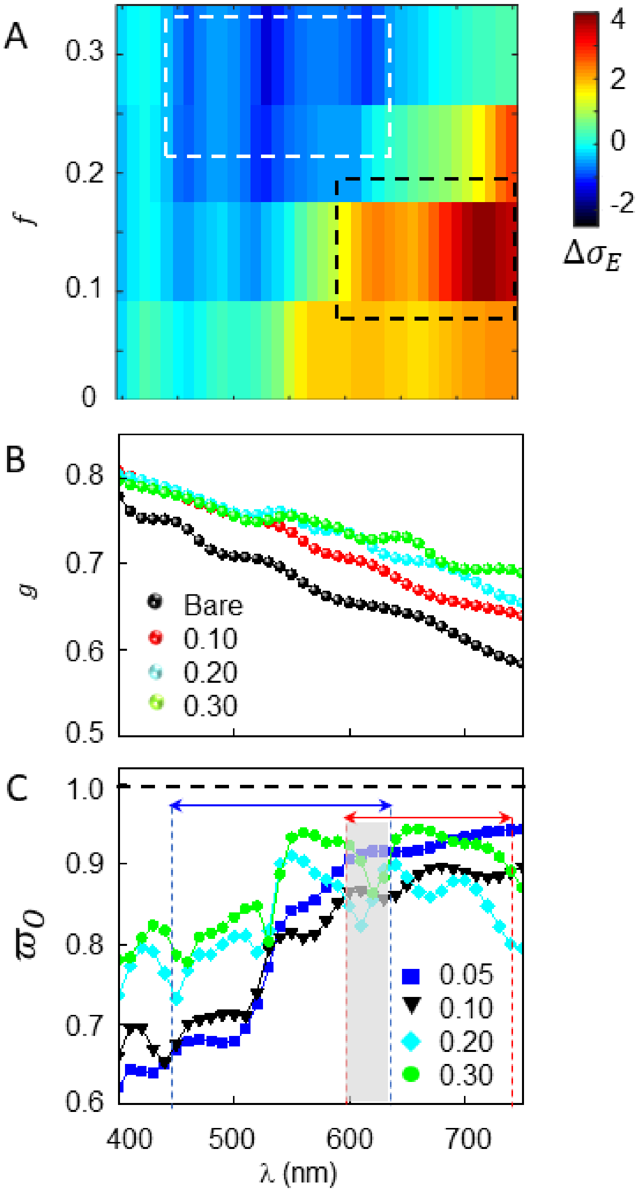

Figure 5.7 Optical properties of a 750 nm silica core with 20 nm AuNPs. (A) Differences of extinction cross-sections ($\Delta\sigma_E = \sigma_E^{core/NP} - \sigma_E^{core}$) for different filling fractions as a function of λ. The region of scattering suppression ($\Delta\sigma_E < 0$) is indicated by a white dashed rectangle, and that of scattering enhancement ($\Delta\sigma_E > 0$) by a black one. (B) Anisotropy factor g of the core for different f. (C) Scattering albedo ϖ_0 of the core for different f. The arrows correspond to regions where scattering suppression (blue) and enhancement (red) is observed in part (A). The grey shaded region shows spectral range where scattering power and g are both enhanced.

We observe this behavior in the results shown in Figure 5.7B. In addition, we note that g is larger than that for the bare core for all values of f. This behavior corresponds to the feature highlighted in Figure 5.1 in which the forward peak is more pronounced and wider angle sidelobes are suppressed. We attribute this to multiple scattering by the AuNPs which suppresses diffraction by the core, leading to reduction of the wide-angle scattering. As a consequence, the power that is scattered by the coated structures is more concentrated in the forward direction relative to scattering by the bare core. Figure 5.7C shows ϖ_0 over the visible spectrum for the structures. The bare core has $\varpi_0 = 1$ over this wavelength range. The addition of AuNPs results in increased absorption (and decreased ϖ_0) across the entire spectrum, but the magnitude of the change varies with f. For low f (< 0.1) ϖ_0 indicates significant absorption for $\lambda < 500$ nm, but relatively higher ϖ_0 for high $f (> 0.2)$ over the same spectral range suggests scattering surpasses absorption as AuNP coverage of the core increases. Referring back to Figure 5.7A, it seems scattering suppression occurs in the spectral range where composites have some optimal absorption relative to scattering, as with the structures $f > 0.2$. On the other hand, scattering enhancement is observed when ϖ_0 approaches 1. There is an additional feature in the variation of ϖ_0 with λ at high f, where we observe an oscillatory behavior. These oscillations indicate strong and complex interactions between the dielectric core and the AuNP cover that, in turn, strongly affects the scattering intensity. When we repeat these simulations for the same core with 5 nm AuNPs, both this non-monotonic behavior of ϖ_0 with f, and the oscillations are absent. As a result, neither suppression nor enhancement occurs (Figure 5.3). However, this f dependence of ϖ_0 is clearly observed in a wide range of core sizes (Figure 5.5) when 20 nm AuNPs are used, underlining the importance of AuNP size.

In Figure 5.8 we explore the dependence on AuNP size. Figure 5.8A plots the scattering efficiency σ_E as a function of λ for a 750 nm bare core and cores with covers of 5, 10 and 20 nm AuNPs, all at $f = 0.3$. The cover consisting of 5 nm AuNPs does not cause any suppression, and in fact, enhances σ_E for $\lambda > 500$ nm. The cover made of 10 nm AuNPs lead to suppressed scattering up to 550 nm, while the cover made of 20 nm AuNPs suppress scattering over the entire visible spectral range. Figure 5.8 B plots the HG-fitted g for the same structures, and shows that g for the 5 nm AuNP coated structure closely follows that of the bare core over the visible spectrum. In contrast, coverage by 20 nm AuNPs results in a significantly higher g, indicating how the angular distribution of power can be tuned by AuNP size. Higher g indicates stronger forward scattering, which we check by computing the angular width of the central peak of the differential scattering cross section at -3dB below the peak, which serves as an approximation for the full-width at half-maximum (FWHM) for forward scattering cone. Figure 5.8C plots this FWHM over the visible region and confirms that the 20 nm AuNP coverage narrows the forward scattering peak the most. The schematics shown in Figure 5.8C, 5.8D, and 5.8E summarize this data, and highlight the changes in the scattered field due to different AuNP sizes on the surfaces of the cores, such as narrowing of the forward scattering peak as FWHM decreases, and smoothing of the side lobes with increasing g, as AuNP size increases. This effect is not limited to a specific core size, and is observed down to core sizes of 400 nm (Figure 5.6).

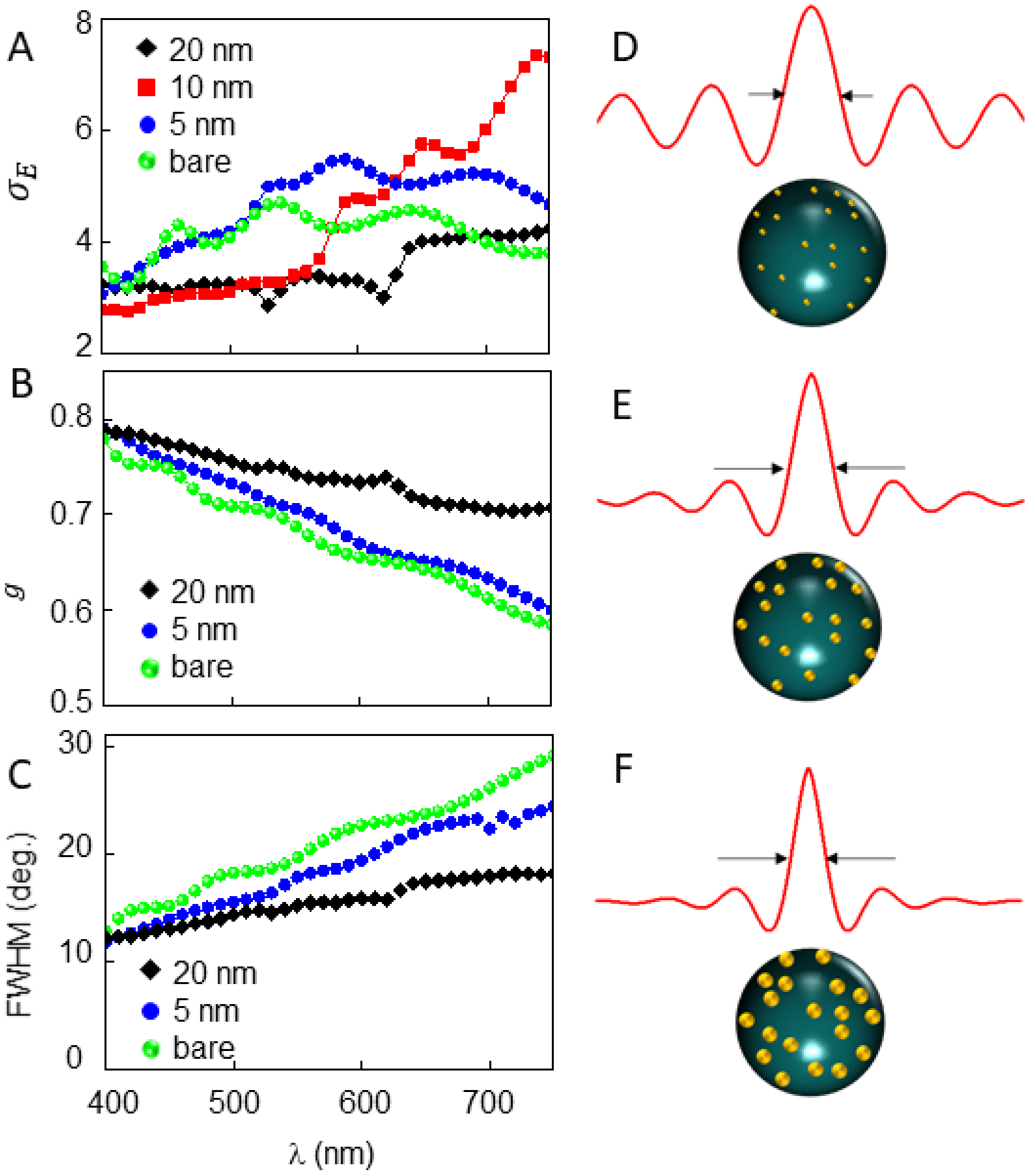

Figure 5.8 (A) Scattering efficiency σ_E, (B) HG-fitted anisotropy g, and (C) FWHM of the differential scattering cross sections for the bare core and core with AuNPs of different sizes, all at $f = 0.3$. Schematic of the cores with coatings of (D) 5 nm AuNPs (E) 10 nm AuNPs, and (F) 20 nm AuNPs, summarizing these changes.

5.5 Conclusion

Our computational model demonstrates that a cover of randomly distributed AuNPs on a dielectric core can be optimized to modulate the mesoscopic optical properties in the visible spectrum in more than one way. A cover consisting of 20 nm AuNPs with moderate filling fractions $0.2 < f < 0.3$ results in significant scattering suppression up to λ = 600 nm for cores larger than the incident wavelength. But a slight variation of f, between 0.1 - 0.2, leads to scattering enhancement in the spectral regime λ > 650 nm for the same cover. This substantial difference in optical response highlights the versatility of this platform. In addition to this spectral modulation, we observe that the presence of the cover results in a preferential concentration of the scattered power in the forward direction. This reshaping of the angular distribution of power occurs when scattering is suppressed and enhanced. Our results further underscore the critical role of absorption versus scattering by the AuNPs, as we establish that some absorption by the AuNP cover is needed to suppress the scattering of the core. However, scattering is suppressed most when f is optimal to promote both multiple scattering and absorption with a stronger dependence on former. It is for this reason that 20nm AuNPs yield more suppression than 5nm AuNPs. In fact, it is because of multiple scattering in the cover that the angular distribution of scattered power by the coated cores is qualitatively different from that by the bare core. Multiple scattering decreases the overall coherence of scattered light and consequently, suppresses the angular sidelobes in the distribution of scattered power. As a result, the forward peak in scattering is more pronounced and the anisotropy factor increases. Through this investigation of the mesoscopic optical properties of nano-assembled plasmonic covers, we have identified parameter regimes where the cover of AuNPs lead to scattering suppression or enhancement. These results can then guide decisions on tuning AuNP size and filling fraction for a wide range of optical and photonic applications in the visible spectrum, ranging from near-field microscopy to high-resolution imaging.

Acknowledgements

Md. I. Khan and S. Ghosh acknowledge support by the National Science Foundation Center for Cellular and Biomolecular Machines (HRD-1547848). A. D. Kim acknowledges support by the National Science Foundation (DMS-1819052 and DMS-1840265) and the Air Force Office of Scientific Research (FA9550-21-1-0196).

Chapter 6

Broadband scattering suppression using 3D plasmonic meta-structure in the visible spectrum

The numerical model established in the earlier chapters showed broadband scattering suppression achieved by the plasmonic meta-structures. These structures are made of dielectric cores coated with colloidal gold nanoparticles. This chapter presents an experimental demonstration of the broadband scattering suppression using plasmonic meta-structures of two core sizes, 500 nm, and 700 nm. A scalable and robust fabrication method was developed to make these core-shell meta-structures. This fabrication method has been described in detail in the earlier parts of this chapter, following a process for characterizing the core-shell meta-structures. Scattering cross-section measurements were carried out over the visible wavelength range for bare silica cores and the core-sell structures. The scattering cross-section measurements revealed broadband scattering suppression by these meta-structures. The simulated scattering cross-section of the bare cores and core-shell structures showed good agreements with the measured results for a filling fraction of 0.3. This filling fraction was computed using an image analysis method.

6.1 Fabrication of plasmonic meta-structures

The core-shell meta-structures are consist of a silica sphere coated with gold nanoparticles randomly distributed on it’s surface, as shown in the schematic in Figure 6.1.

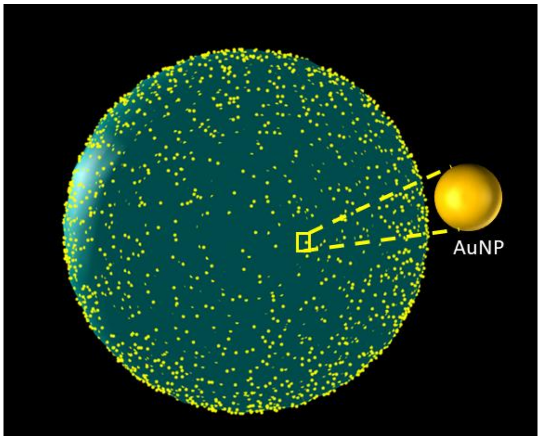

Figure 6.1 Schematic of the plasmonic meta-structure. Spherical silica core (blue) decorated with randomly distributed gold nanoparticles (yellow).

AuNP coated silica sphere fabrication has two main steps. In the first step, the surfaces of solid, nonporous silica spheres are functionalized with amine terminated ligands. In the second step, the silica surfaces are decorated with citrate-capped gold nanoparticles. The silica spheres, with average diameters 500 and 700 nm, were purchased from Bangs lab. The amine terminated ligand used to functionalize the silica surface was N-[3-(trimethoxysilyl)propyl]ethylenediamine (TMSPA). This ligand and 20 nm gold nanoparticles (OD 1) were purchased from Sigma Aldrich. All the chemicals and nanoparticles were used without any further purification.

6.1.1 Functionalizing silica surface

Non-functionalized silica nanoparticles (SiNPs) have natural hydroxyl(-OH) groups on them. In the case of silica, these hydroxyl groups are commonly known as silanol groups[201]. The surface functionalization process takes advantage of silanol groups to attach the alkoxysilane ligand. The methoxy group of the ligand ($-OCH_3$) reacts with the silanol present on the silica surface. As a result, the ligand binds with the silica by forming a siloxane(-Si-O-Si-)[202]–[211]. Figure 6.2 shows a schematic of this reaction.

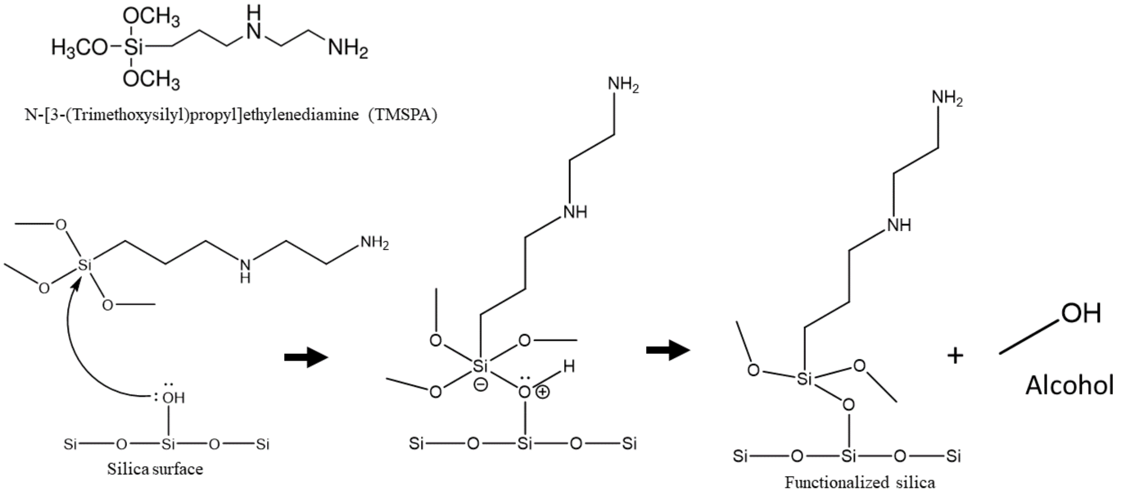

Figure 6.2 Reaction schematic to functionalize silica with TMSPA (bottom row). Methanol is produced as a byproduct. Structure of a single TMSPA ligand is shown on the top left.

Surface functionalization takes place at room temperature. Silica nanoparticles and TMSPA are added to ethanol in a glass vial. Then the solution is stirred vigorously using a magnetic stirring bead at 1250 revolution per minutes (RPM) for eight hours. Surface functionalized silica is then centrifuged at approximately 2000 relative centrifugal fource (RCF) to separate it from the non-absorbed ligands and ethanol mixture. Then the functionalized SiNPs are redispersed in deionized (DI) water. The centrifugation and redispersion process is repeated five times to remove all the non-absorbed ligands. The exact surface functionalization process was applied for both 500 nm and 700 nm silica spheres. Following this process, 1 mg of SiNPs of each size was functionalized for the experiments. The 500 nm and 700 nm SiNPs were functionalized with $500\mu L$ and 1ml of the ligands, respectively. Functionalized and cleaned SiNPs were stored in DI water for gold nanoparticles coating.

6.1.2 Gold coated silica sphere

The core-shell structures of silica and gold nanoparticles were fabricated via electrostatic nano-assembly[212][213]. This is a self-assembly process in which lone pair electrons of the amine are shared with gold nanoparticles forming a coordinate bond[214]–[222]. As a result, AuNPs are adsorbed on the functionalized silica surface. Adsorbing citrate capped AuNPs arranged themselves on the silica surface due to the electrostatic interactions between the SiNP and each other, resulting in to a robust and stable core-shell structure[223][224]. As purchased AuNPs were centrifuged (26×10^3 rcf, 30 min) to concentrate at the bottom of the Eppendorf tube before the fabrication process. A higher concentration decreases interaction time between the AuNPs and the SiNPs, promoting a faster adsorption process. Functionalized SiNPs were added to the concentrated AuNPs dispersed in DI water. This mixer was then stirred using a vortex mixer gently. The adsorption process was allowed to react for four hours at room temperature. Figure 6.3 shows AuNP decorated silica sphere pallets at the bottom of the tube.

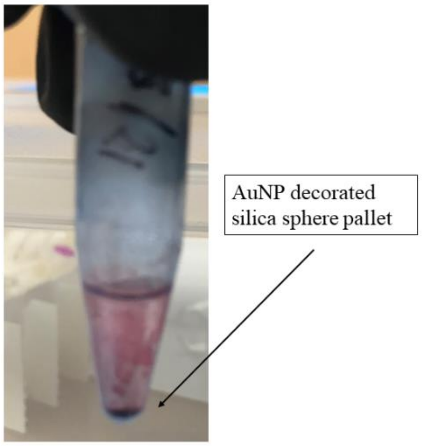

Figure 6.3 AuNP decorated SiNP pallet at the bottom. The supernatant containing non-adsorbed AuNP.

The supernatant contains non-adsorbed AuNPs. The supernatant was pipetted out, and the sample pallet was redispersed in DI water. The redispersed solution was then centrifuged at a very low speed (500 rcf) for two minutes to separate heavier AuNP coated silica from the non-adsorbed AuNPs following removal of the supernatant. This process was repeated five to seven times to ensure the solution was free from non-adsorbed AuNPs. 6 ml and 12 ml of purchased AuNP solutions were concentrated and used to fabricate core-shell structures of core sizes 500 nm 700 nm, respectively.

6.2 Meta-structure characterization

Nano-assembled meta-structures were characterized using the ultraviolet-yisible (UV-Vis) spectroscopy and the scanning electron microscope (SEM). UV-Vis spectroscopy shows the absorbance properties of the material. UV-Vis measurement determined the purity and absorption maximum of the sample.

6.2.1 Ultra-violet Visible spectroscopy

UV-Vis spectroscopy (Lambda 35, Perkin Elmer) was carried out on the as-obtained AuNP from the manufacturer and ligand functionalized silica nanoparticles. Gold nanoparticles show much higher absorbance compared to the TMSPA functionalized silica core. A plasmon enhanced absorption peak for AuNPs was observed at 523 nm (Figure 6.4).

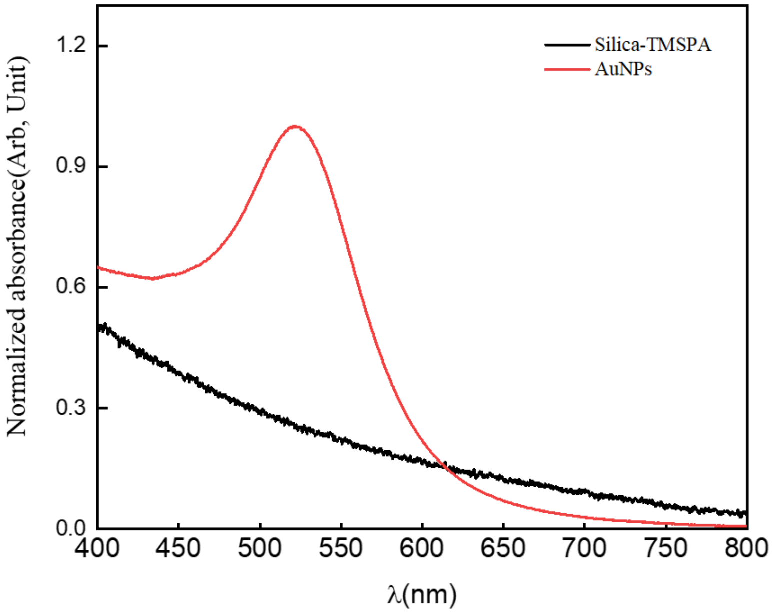

Figure 6.4 UV-Vis spectroscopy of 20 nm gold nanoparticles (red) and ligand (TMSPA) functionalized silica sphere of 500 nm (black).

Ligand functionalized silica core showed very low absorbance in the visible wavelength range. The absorbance of the silica sphere showed a monotonous rise as the wavelength gets smaller. The 500 nm and 700 nm functionalized silica showed almost identical absorption curves. Hence only the UV-Vis spectra of the 500 nm silica are included here.

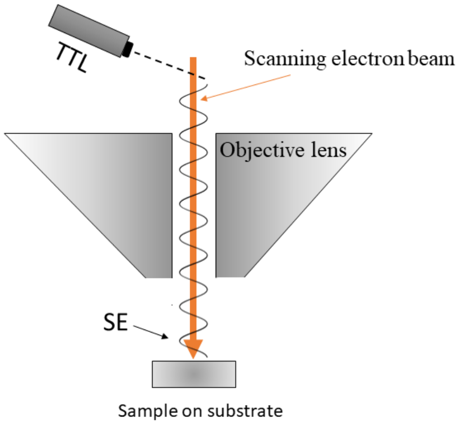

Figure 6.5 Schematic of the working process of the TTL detector.

6.2.2 Scanning electron microscopy

SEM micrograph of the surfaces of the meta-structures revealed the integrity of the core-shell structures. A Zeiss Gemini 500 scanning electron microscope was used for characterization. Meta-structures were imaged using the Through-The-Lens (TTL) detector and backscattered electron detector (BSD).

The primary scanning electron beam of the SEM interacts with the specimens and creates secondary electrons (SE). These secondary electrons are categorized as SE_1, SE_2, SE_3 based on their kinetic energy, from high to low[225]. SE_1 and SE_2 are originated just below the sample surface. Therefore, they exit the surface without deviated much from their point of origin. On the other hand, SE_3 signals are originated from a deeper part of the sample, and escaped trajectory is prone to much more deviation. Figure 6.5 shows a schematic of the TTL detector's working process. A TTL detector uses a confined magnetic field in the objective lens column to pull SE_1 and SE_2 electrons through the objective while ignoring SE_3 signals. As a result, a TTL detector provides a higher resolution and finer surface details than other detectors[225].

When the primary scanning electron beam interacts with the specimen's atoms, their trajectories deviate. The primary electrons can scatter back and be ejected out of the sample in suitable conditions, preserving most of its kinetic energy. Generally, heavier nuclei scatter back electrons with higher energy than nuclei of lighter elements [225][226]. A BSD detector detects these backscattered electrons from the specimen. It is a disk-shaped detector located just above the sample, and it is made of two parts A, and B (figure 6.6). Combining the SE and the backscattered electrons signals, information about the sample's topographical and compositional state can be obtained[225]. Signals from both parts (A and B) of BSD are added to get the compositional form of the sample. The havier element appears brighter in the BSD image. Meta-structure imaged using the BSD provides geometric distribution of the AuNPs on the surface of silica spheres. BSD images were used to calculate the surface filling fractions. Figure 6.7 shows both TTL (A, B, C) and BSD (D) images of the core-shell structures.

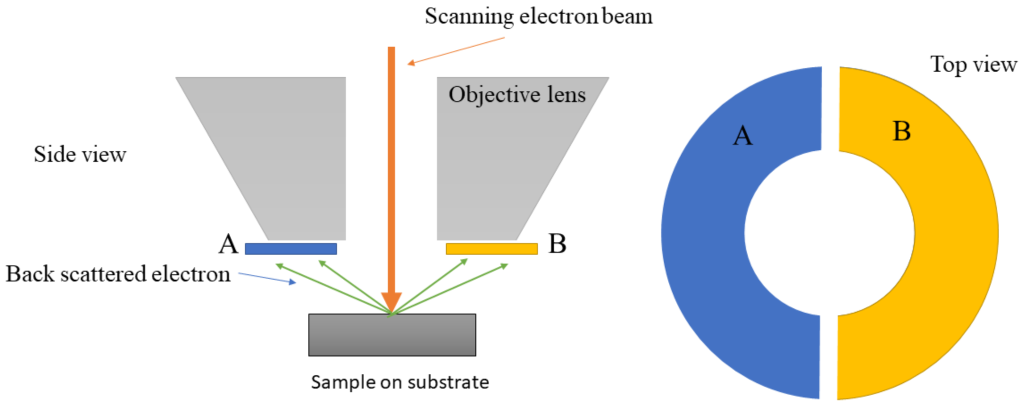

Figure 6.6 Schematic of location of BSD detector. Side view (left) and top view (right) of the detector configuration.

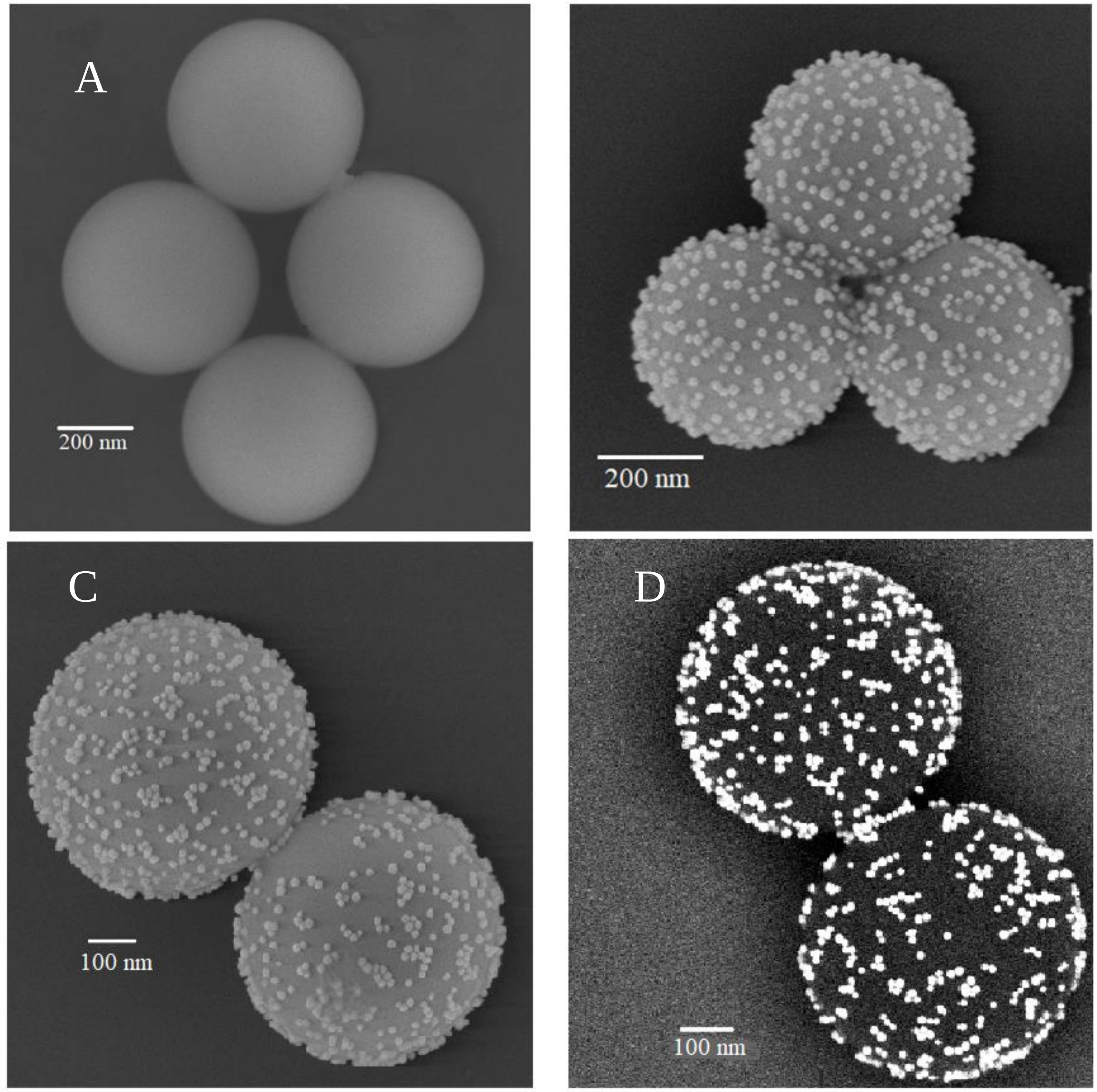

Figure 6.7 Scanning electron micrograph of bare silica cores and AuNP coated silica spheres. (A) Bare silica sphere with diameter 500 nm. (B) AuNP coated 500 nm silica spheres. (C) 700 nm silica spheres coated with AuNPs. (D) BSD image of 700 nm silica spheres coated with AuNP. The AuNPs appear brighter compared to the background in BSD images.

Broadband scattering suppression by the plasmonic meta-structures occurs for AuNP filling fraction of more than 20%, predicted by the numerical model. Fabrication of the core-shell meta-structures was optimized to achieve this high filling fraction(> 20%). Figure 6.8 shows a much lower surface coverage of AuNPs.

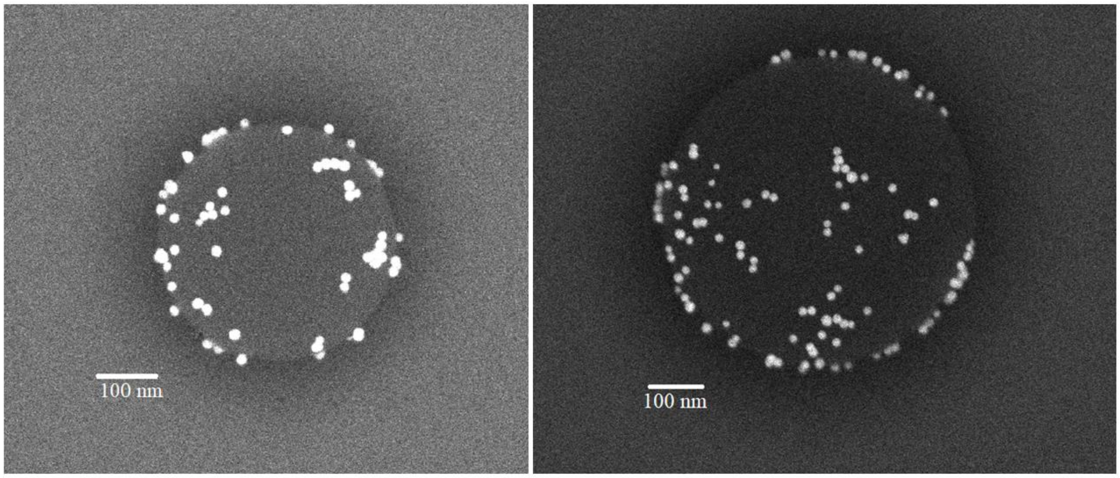

Figure 6.8 BSD image of low surface coverage core-shell structures. A 500 nm silica core coated with AuNP is shown on the left, and a 700 nm coated silica core on the right.

During the optimization of the fabrication process, it was found that the amount of AuNPs, ligands, and the silica-ligand functionalization duration plays a crucial role. Therefore, one of these three elements was varied while keeping other elements constant to optimize the fabrication process. Figure 6.7 shows the final product of this optimized fabrication process, yielding very high adsorption of AuNPs on the silica surface. The amount of AuNPs and the ligand combinations for a specific core diameter reported in section 6.1 was obtained after successfully optimizing the fabrication process.

6.2.3 Surface coverage

Surface coverage is one of the crucial parameters in predicting and simulating scattering suppression by the plasmonic meta-structures. Surface coverage was calculated as a ratio of the area occupied by the AuNPs to the total surface area of a silica sphere. Thus, the surface area occupied by the AuNP clusters provides a practical method of quantifying the number of nanoparticles on the surface of a dielectric core. Figure 6.9 depicts a generalized step-by-step process of isolating and calculating the number of AuNP clusters on the silica surface.

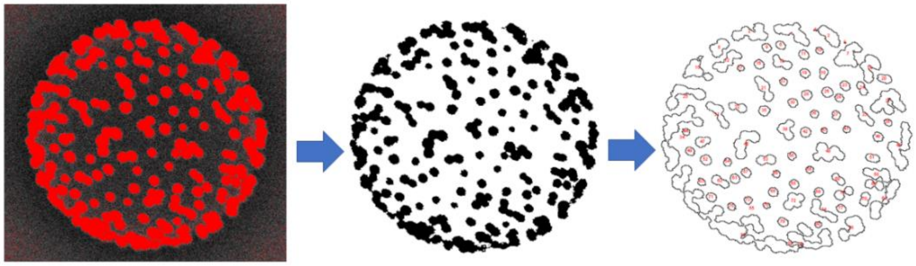

Figure 6.9 Surface coverage computation process via image processing using ImageJ. BSD image of a 500 nm core-shell structure with highlighted AuNP clusters(red).

The process of removal of the background and finally obtaining the AuNP clusters shown from left to right in figure 6.9. In step one, AuNP clusters are selected based on the brightness difference compared to the background using a mask in ImageJ[227]. Then the background of the image is removed by highlighting just the AuNP clusters. Finally, the total areas of the clusters are computed. This process was somewhat automated and carried out using ImageJ.

Numbers of AuNPs in case of simulating meta-structures were generated using shell volume as a container. Shell volumes were calculated as a multiplication of the core's surface area and the shell-thickness (see chapter 4, section 4.3.3).

The AuNP number density was generated as,

$$N = \left\lfloor filling\ fraction \times \frac{shell\ volume}{nanoparticle\ volume} \right\rfloor \tag{6.1}$$

The *filling fraction* in Eq (6.1) determines how much of the volume would be occupied by the AuNPs. Here the shell-thickness was considered as constant for a specific structure as well as the diameter of the nanoparticles.

AuNPs on the fabricated meta-structures were not constant in diameter. The BSD images revealed that AuNPs are clustered with varied areas instead of distributed as separate particles (figure 6.9). As a result, computing the size of these AuNP clusters and the ratio of this area to the entire surface area of the core provides a practical method of estimating the amount of filling fractions in terms of surface coverage.

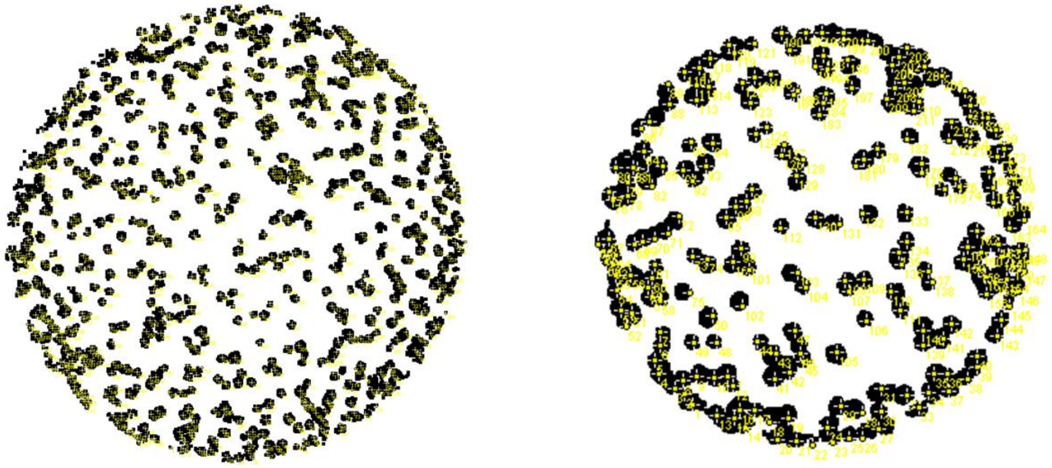

Figure 6.10 Highlighted AuNPs of 700 nm (left) and 500 nm (right) meta-structures using ImageJ. The estimated highlighted particles (yellow cross marks) on 700 nm structures were approximately 660 and on 500 nm structures were approximately 290.

A proof-of-concept analysis process was developed and described here to demonstrate the equivalence between the surface fraction analysis using ImageJ and volume filling fraction for simulated structures. In this process, an isolated dark spot on the BSD image was highlighted using a yellow cross mark, assuming it is a single AuNP. In the case of clusters, the number of cross marks was estimated by comparing with a single AuNP or a dark spot (figure 6.10).

Analyzed images shown in figure 6.10 are an example. Here approximately 290 spots on one 500 nm structure and 660 spots on a 700 nm structure. Therefore, the total number of spots or AuNPs would be 580 for 500 nm and 1320 for 700 nm core-shell structures. This estimation assumes that both surfaces of the meta-structures have an equal amount of AuNPs. The surface fraction from image analysis of these two structures yields a filling fraction of 0.3 for 500 nm and 0.28 for 700 nm structures. The simulated number of AuNPs for the 500 nm and 700 nm structures was 680 and 1176, respectively, for the filling fractions mentioned above. The measured AuNP diameter observed using SEM was as large as 29 nm, and the smallest was 19 nm. Hence an average AuNP diameter was considered 24 nm, and shell-thickness was 24 nm for simulation. Compared with the fabricated structures, nanoparticles diameter can be thought of as shell thickness.

The differences between the image analyzed nanoparticle number and simulated was approximately 14% for 500 nm and 10% for the 700 nm core-shell structures. This discrepancy between the image analyzed and simulated AuNP numbers are acceptable and understandable for the following reasons. The actual number of dark spots comprising a cluster cannot be determined with a high degree of accuracy. More than one AuNP assembled on top of another is possible in fabricated structures. That was not visible in the BSD image. In the fabricated structures, there is a variation in the AuNP diameter, but in the case of simulation, it is constant. Hence the assumption of a constant shell thickness for the simulated structure would impact the amount of AuNP packed in the shell volume. An average filling fraction obtained by analyzing several images was applied to the simulation model. This average filling fraction resulted in a simulated scattering cross-section across the spectrum showed a good agreement with the measured cross-section, confirming the validity of finding the filling fraction this filling fraction analysis (see section 6.4).

Surface filling fractions calculations following the process described above were carried out on both 500 nm and 700 nm core-shell structures. The average computed filling fraction was approximately 0.35 for 500 nm and 0.31 for 700 nm core-shell structures. Figure 6.11 shows a 500 nm meta-structure count as a function of surface coverage by gold nanoparticles. An average of 0.35 filling fraction or surface coverage was obtained by a gaussian distribution fit of the meta-structure count and corresponding filling fractions.

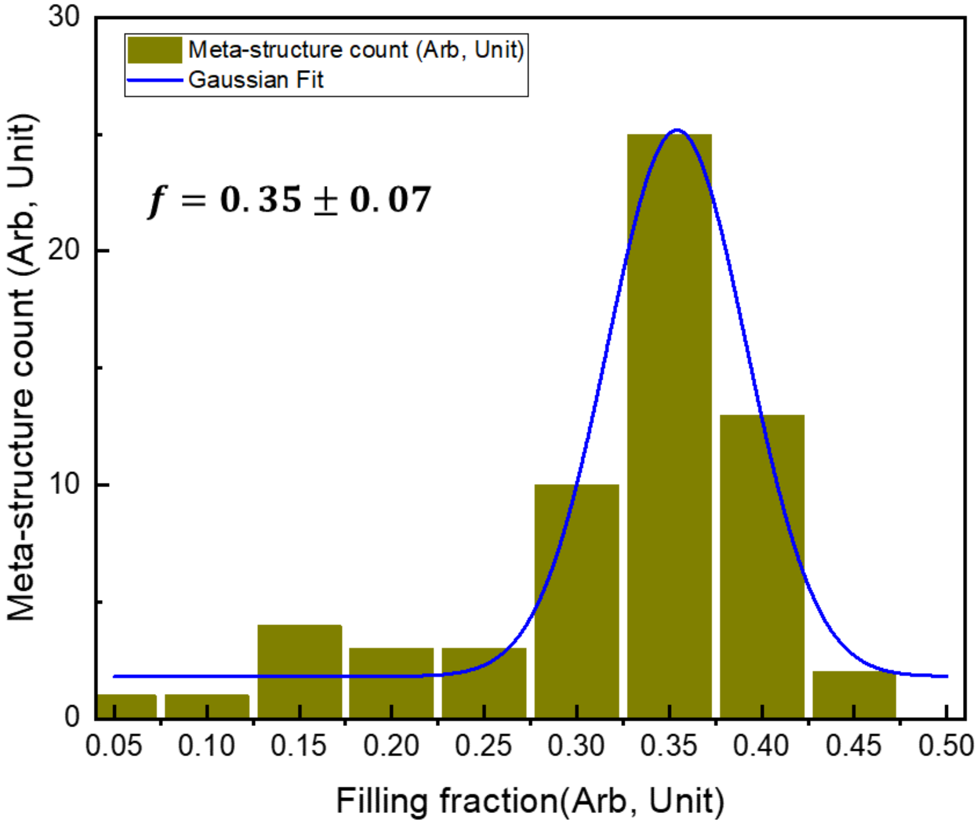

Figure 6.11 500 nm meta-structure count as a function of filling fraction. The average filling fraction was $f = 0.35$ with a standard deviation of 0.07 obtained using a gaussian fit.

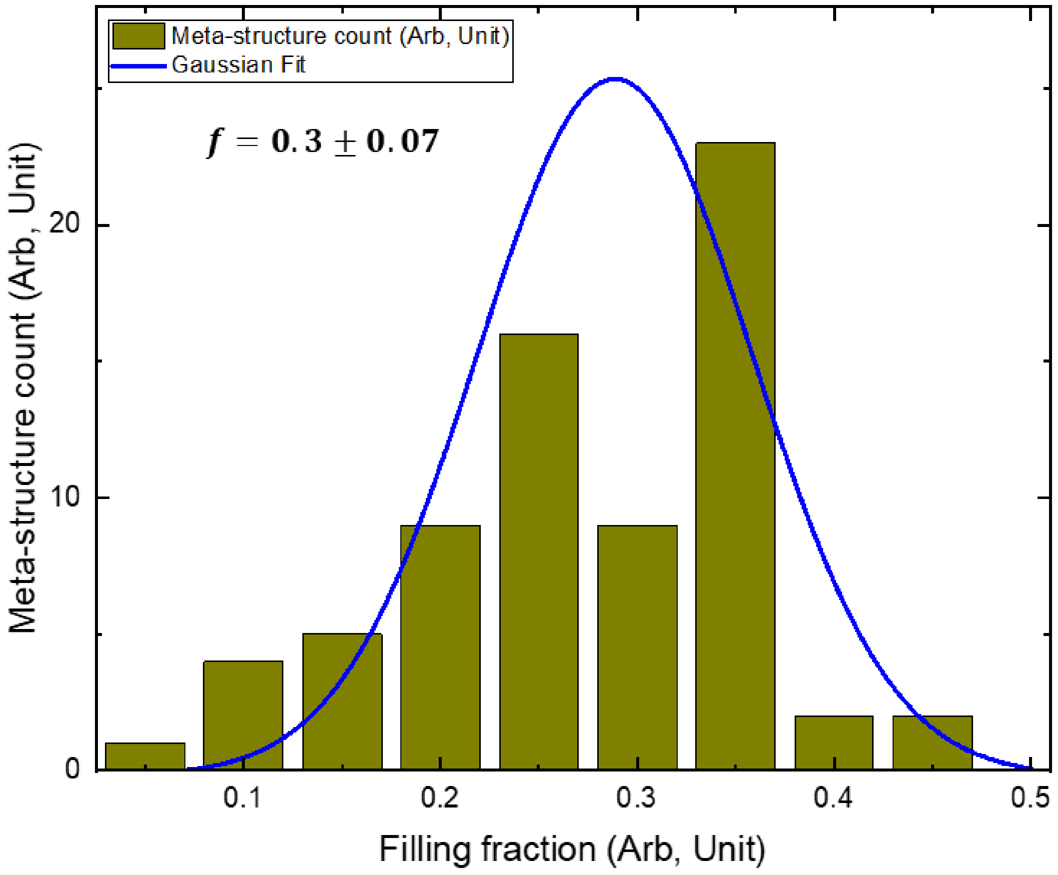

Figure 6.12 700 nm meta-structure count as a function of filling fraction. The average filling fraction was $f = 0.3$ with a standard deviation of 0.07 obtained using a gaussian fit.

Surface coverage analysis on 700 nm core-shell structures yielded an average of 0.30 or 30% of the silica surface covered by AuNPs. Figure 6.12 shows surface coverage analysis results of the 700 nm meta-structures. Few meta-structures of both sizes had barely any AuNP on them, but their quantity is low enough not to lower the overall filling fraction of the meta-structures. Figure 6.8 shows typical low-filling fractions structures. The filling fraction obtained following this process was applied to the simulation model to compare the simulated and experimental results of the scattering cross-sections. The following sections describe experimental methods and related scattering cross-sections results.

6.3 Scattering cross-section measurements

Scattering cross-section of the bare silica sphere and AuNP coated silica spheres were measured to demonstrate the broadband scattering suppression. Scattering cross-section was measured by collecting the diffused light in transmission and reflection. The total scattering cross was obtained by adding diffused light intensities (reflection and transmission) [128], [228]–[231]. Figure 6.13 shows the geometric aspect of scattering of the incident light schematically. A specular component of the incident light maintains the same direction of propagation in transmission (0°) and the opposite direction in reflection (180°) with respect to the incident beam. Incident lights are diffused due to the scattering by the samples. Diffused components are spread at an angle from the point of origin[3].

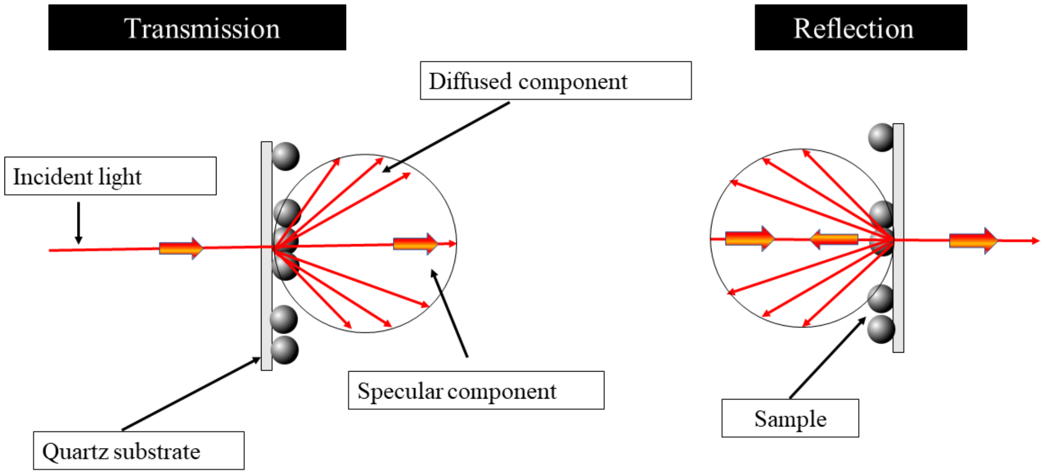

Figure 6.13 Schematic showing the diffused and specular components of scattered light.

Sample for measurement was prepared by drop-casting 50 μL of well-dispersed (in DI water) solution on a circular quartz substrate. A thorough cleaning and drying process was followed before drop-casting the sample on it. First, the quartz substrate was thoroughly cleaned using acetone, methanol, and DI water alternately in a sonication bath. The substrate was then dried using nitrogen, ensuring no foreign particles were present. Finally, the quartz surface was plasma cleaned using a tabletop, basic plasma cleaner (PDC-32G, Harrick Plasma) to make the surface hydrophilic before drop casting. Then the drop casted sample was dried in a desiccator before optical measurements.

The scattering cross-section was measured using an integrating sphere. A tunable (430 nm to 700 nm) pulsed laser system (Super K, NKT photonics) was used as a source of incident light. Figure 6.14 shows the experimental setup of the scattering cross-section measurements. A barium sulfate coated integrating sphere (4″ diameter, model 819 C SF-4, Newport) was used to collect diffused components of scattered light. This highly reflecting coating provides more than 97% reflectance in the operating wavelength range[232]. The sample was mounted on the 0° port or entrance port.

The scattered lights are collected at the 90° port, which is perpendicular to the direction of incident light. A port that is opposite to the entrance port (180° port) was blocked using a light trap. The light trap was constructed in house using a foot-long non-reflecting metallic pipe of 1″ diameter. One end of the pipe was mounted to the 180° port, and another end was blocked by a beam blocker. The light trap prevents specular components of the light from interacting with the interior of the integrating sphere, ensuring that only diffused components are collected.

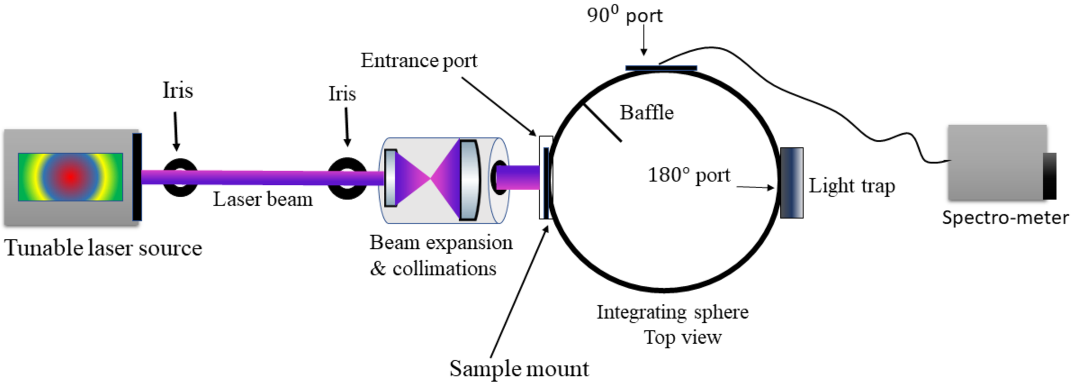

Figure 6.14 Experimental setup of scattering cross-section measurements.

Diffused light intensity was measured using a Spectro-meter (Princeton Instruments, SP-2300i) connected to the 90° port for both reflection and transmission. The wavelength of the incident light was varied 10 nm for consecutive measurements from 430 nm to 700 nm. Total scattering cross-section was computed as the sum of diffused transmission and reflection intensities. These measurements were carried out for bare silica spheres, and AuNP coated silica spheres. The following section depicts the results of scattering cross-section measurements.

6.4 Result

500 nm and 700 nm plasmonic meta-structures show suppressed scattering cross-sections. Figure 6.15, and figure 6.16 demonstrate broadband scattering suppression by the 500 nm and 700 nm meta-structures, respectively.

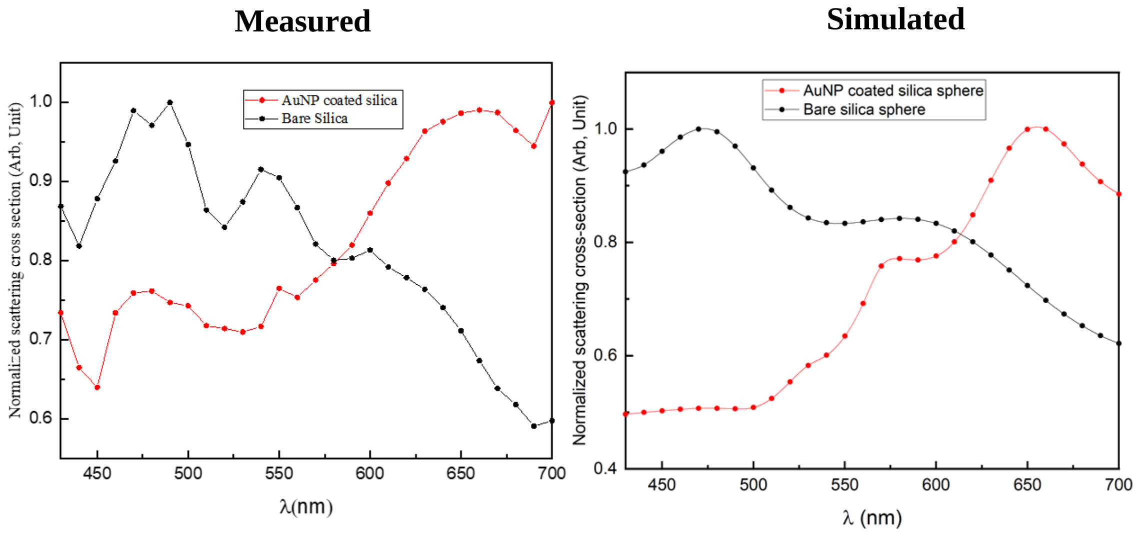

Figure 6.15 Measured scattering cross-section (left) of 500 nm bare silica sphere (black dots) and AuNP coated silica sphere (red dots) of the same size. Simulated scattering cross-section of the bare core and core-shell structures for 30% filling fraction showed on the right.

AuNP coated 500 nm silica sphere shows suppressed scattering compared to the bare silica core of the same size up to 575 nm in the visible wavelength range (figure 6.15). The figure 6.16 shows suppressed scattering by the 700 nm core-shell meta-structure (red dots) compared to bare silica spheres (black dots) of the same size. The 700 nm core-shell structures suppress scattering up to 600 nm in the visible spectrum (figure 6.16). The well-known signature Mie scattering resonant peaks from the bare silica cores (black dots) are absent or mostly suppressed in the case of meta-structure scattering cross-section (red dots) for both core-shell structures (figure 6.15, and figure 6.16). Scattering cross-section of the meta-structures increases beyond 575 nm incident light in the case of 500 nm and beyond 600 nm in the case of 700 nm core-shell structures. The average filling fraction for both core-shell sizes was approximately 30% obtained via image analysis (see section 6.2.3). Simulated cross-sections for 30% filling fraction are shown in the case of both structures (figure 6.15, and figure 6.16). Simulated and measured scattering cross-section depicts a good agreement between them.

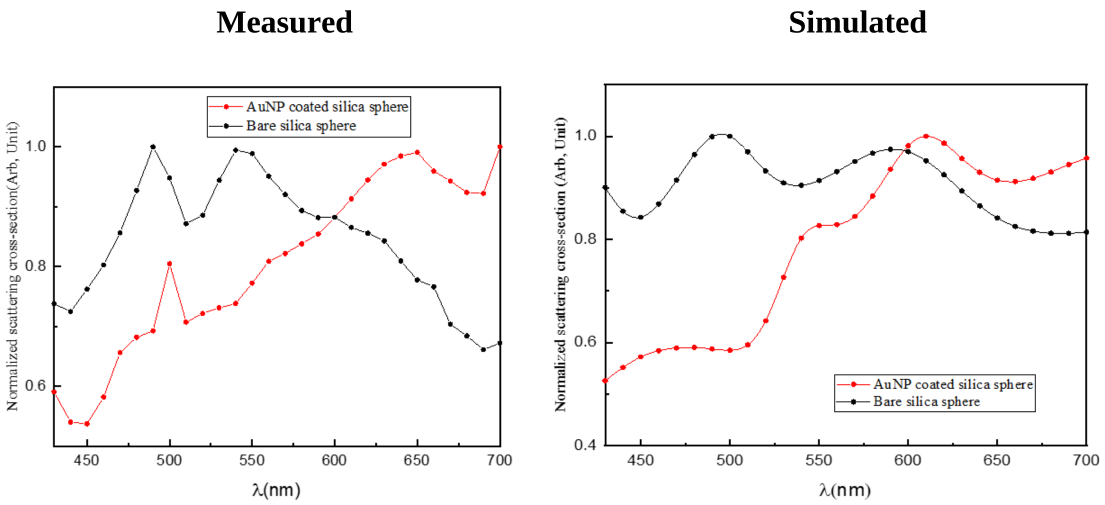

Figure 6.16 Measured scattering cross-section (left) of 700 nm bare silica sphere (black dots) and AuNP coated silica sphere (red dots) of the same size. Simulated scattering cross-section of the bare core and core-shell structures for 30% filling fraction showed on the right.

The common trend of increased scattering cross-section beyond 600 nm incident wavelength is present in both simulated and measured results. A filling fraction of 30% for simulating scattering cross-section of both core-shell structures was within the standard deviation of their filling fraction distribution shown in figures 6.11 and 6.12. Agreement between the overall measured and simulated cross-section is acceptable. However, some discrepancies in the amount of scattering suppression and position of resonance peaks need to be addressed. These discrepancies may be arising due to the following reasons. First, the simulated scattering cross-section refers to a single core-shell meta-structure. Second, the simulated structure had a constant AuNP coverage of 30%. Finally, the AuNP diameter was fixed for the simulated system. The experimental data was from numerous meta-structures. The AuNP filling fractions were not constant on these meta-structures. Filling fractions were as high as 0.45 and low as 0.05 for the fabricated structures. The AuNP also had a size distribution, from 19 nm to 24 nm. Therefore, discrepancies between the measured and simulated scattering cross-sections can be reduced further by incorporating filling fraction and AuNP size distribution.

6.5 Conclusion

Broadband scattering suppression (from 430 nm to 600 nm) in the visible spectrum was achieved experimentally using plasmonic meta-structures. Scattering suppression was observed by the 500 nm and the 700 nm core-shell structures up to 575 nm and 600 nm of the visible spectrum, respectively. Fabrication via electrostatic nano-assembly made physically realizable core-shell plasmonic meta-structures possible. This fabrication method was proved to be scalable for various core sizes. Simulated and measured scattering cross-section results showed good agreement in the wavelength range of suppression following an increase in scattering cross-section beyond 600 nm incident light. The experimental results also confirm that the computational model can predict scattering cross-sections of the meta-structures correctly to a great extent.

Chapter 7
Summary and future work

Far-field light scattering and diffraction originating from nano-assembled 3D plasmonic meta-structures were analyzed, modeled, and measured in this dissertation. It highlights the significance of a multiscale simulation model that can be used to analyze and predict multiple optical interactions between a dielectric spherical core surrounding randomly distributed plasmonic nanoparticles. Furthermore, successful fabrication of the physically realizable plasmonic meta-structures following scattering cross-section measurements presents potential applications for sensing and high-resolution imaging due to its ability to suppress scattering and alter the far-filed scattering pattern as a consequence of the scattering suppression.

The advent of nanostructured plasmonic material made the realization of meta-materials possible. One of the mentionable applications of meta-structure is passive electromagnetic cloaking by suppressing scattering. A numerical model to design meta-structure and compute its electromagnetic response showed that physically realizable (450 nm to 950 nm) structures are possible for plasmonic cloaking. These plasmonic meta-structures are comprised of a dielectric (silica) core coated with randomly distributed gold nanoparticles (AuNPs). It was demonstrated in this dissertation that the scattering suppression range could be manipulated by varying the amount of AuNPs or filling fractions (f). A broadband scattering suppression from 430 nm up to 600 nm was observed for a 750 nm meta-structure by varying the filling fractions ($0.2 \leq f \leq 0.6$) of 10 nm AuNP coating. Scattering suppression from a wide range of core sizes (450 nm – 950 nm) was also demonstrated for 10 nm AuNP coating for a constant filling fraction of 30%. Comparison of scattering cross-sections between the 5 nm and 20 nm AuNP coated meta-structures showed that a 5 nm AuNP is inefficient for scattering suppression. A numerical experiment to validate this model showed that it could reproduce the scattering minimum of an experimental system with a higher degree of accuracy than other models based on the effective medium theory. The numerical model presented in this dissertation is computationally robust and scalable because it can account for a wide range of core sizes, AuNP diameters, and interactions between the dielectric cores and randomly distributed plasmonic nanoparticles explicitly.

This dissertation established that strong scattering and absorption between the AuNPs and the silica core play a crucial role in achieving scattering suppression. The mechanism of attaining scattering suppression was explored in terms of scattering albedo (ϖ_0), scattering efficiency (σ_E) and anisotropy (g) parameters. Scattering by the AuNPs promotes multiple interactions (both scattering and absorptions) between the AuNPs and dielectric core. Hence plasmon-enhanced scattering properties of the AuNPs show dominance over their absorption in achieving scattering suppression was a fascinating and intriguing realization. The total scattering suppression also alters the angular distribution of the scattered energy. A differential scattering cross-section study showed that the meta-structures have narrower central peaks and smoother (suppressed) angular sidelobes than the corresponding bare silica cores. Angular distribution of the central peak was quantified by computing the anisotropy of the scattering pattern. Core-shell structures were found to have higher anisotropy (forward peaked) for all core diameters (450 nm $-$ 850 nm) and for all sizes of AuNP (5nm, 10nm, and 20 nm) coating than the corresponding bare cores. The scattering albedo (ϖ_0) and anisotropy (g) of the scattering pattern provides an effective and efficient combination of parameters to predict an operational wavelength range over which meta-structures can be successfully applied to increase the signal-to-noise ratio and high-resolution imaging.

A practical and scalable fabrication method for making plasmonic meta-structures was presented in this dissertation. This fabrication method takes advantage of the silica surface and ligand chemistry to adsorb AuNPs on the silica surface. AuNPs are adsorbed covalently on the silica surface and rearranged into a core-shell formation due to the electrostatic nano-assembly. The fabrication method was optimized to achieve a specific filling fraction (> 0.2) for meta-structures (diameter 500 nm and 700 nm) that are suitable for scattering suppression applications. Scattering suppression measurements of the meta-structures of 500 nm and 700 nm showed suppressed scattering compared to bare silica cores of the same sizes. Furthermore, simulated scattering cross-sections of the corresponding meta-structures showed a reasonable agreement between the measured and simulated results.

Successful fabrication of plasmonic meta-structure paves the way to measure the changes in angular sidelobes due to scattering suppression. The Rayleigh criterion for diffraction limits the resolving ability of two adjacent objects[233]. According to the Rayleigh criterion, two images are just resolvable if the center of the diffraction pattern of one directly overlaps the first minimum of the diffraction pattern of the second object. Two objects are barely resolvable if separated by the angle, $\theta \approx 1.22\,\lambda/D$, here D is the diameter of the aperture, mirror, lens, etc. λ is the incident wavelength. It was shown semi classically and quantum mechanically that Rayleigh criterion can be overcome[234]–[242]. A conclusion can be drawn from the concept of the Rayleigh criterion that resolving limit can be increased by suppressing angular sidelobes associated with a specific diffraction pattern. Figure 7.1 shows the overlapping diffraction patterns (airy disks) arising from two adjacent objects and the resolution limit.

As a part of the continued work, a proof-of-concept experimental method to observe suppression of the angular sidelobe was developed. In this experiment, a plasmonic meta-structure would be exposed to the diffracted light arising from a circular aperture (pinhole). Electric field arising from the pinhole would act as an incident field on the meta-structure.

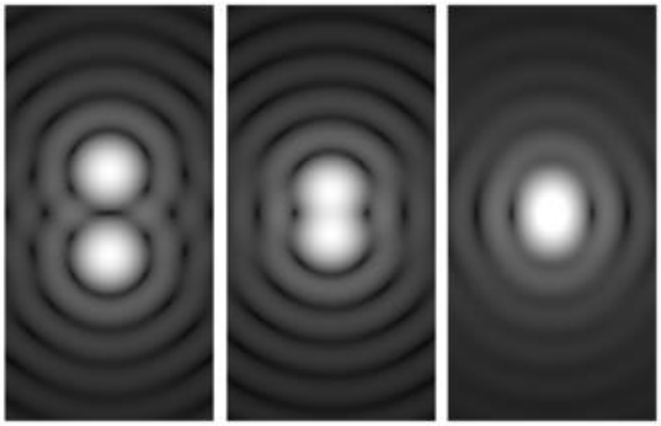

Figure 7.1 Airy diffraction patterns generated by light from two point sources passing through a circular aperture, such as the pupil of the eye. Points far apart (left) or meeting the Rayleigh criterion (middle) can be distinguished. Points closer than the Rayleigh criterion (right) are difficult to distinguish. © Spencer Bliven. Wikimedia Commons, the free media repository.

The resultant intensities on a far-field detector or screen would result from the incident field from a circular aperture after being modified by a meta-structure. Thus, a successful demonstration of the angular sidelobes suppression is sufficient to consider these meta-structures as a potential candidate for high-resolution imaging.

A computational model was developed to compute the interaction between the field exiting from a circular aperture and the meta-structure following the projection of the total field on a screen. This computation model extends the model described earlier (see chapter 4) following a modification to account for the interaction of the incident filed with a meta-structure. Fraunhofer or the far-field diffraction regime was considered for computing this interaction[243]. Distance of the meta-structure from the aperture was constrained using the following expression

$$\frac{a_0^2}{\lambda_{inc}\, z_0} \ll 1$$

Here a_0 is the diameter of the aperture. z_0 is the distance of the meta-structure from the circular aperture. λ_{inc} is the incident wavelength. This expression ensures the Fraunhofer condition was satisfied. Figure 7.2 shows the simulated airy disk patterns of a circular aperture (A) and the final intensity pattern (B). Meta-structure in this simulation was made of a 700 nm silica core coated with 20 nm AuNP and the filling fraction was 30%.

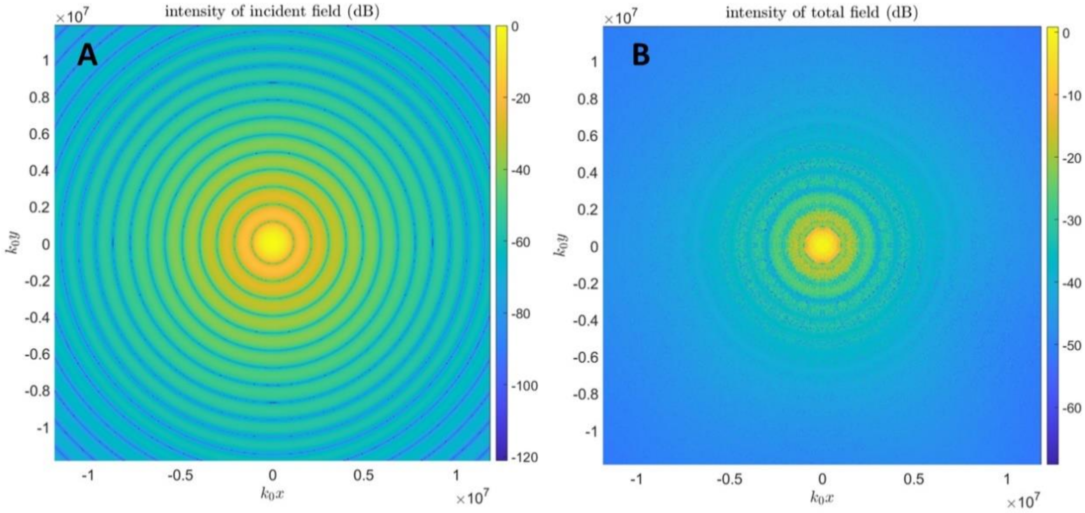

Figure 7.2 Electric field intensities. (A) The intensity of the incident field is due to a $1\mu m$ circular aperture. (B) Total intensity observed on a screen or a detector. The incident wavelength was 530 nm. The meta-structure was at $10\ \mu m$ from the aperture. The total field shows suppressed angular sidelobes.

The size of the circular aperture was chosen following Babinet's principle[173], so that the diffraction pattern from this circular aperture and an obstacle of the same diameter would be equivalent. Simulated results show total field intensities retained only a few angular sidelobes (figure 7.2 B), and their intensities are much reduced compared with the incident field intensities (figure 7.2 A).

Suppressed angular side-lobes and higher scattering anisotropy are the consequences of the total scattering suppression by the core-shell meta-structures. Tuning of these far-field scattering properties is possible due to the multiple interactions (scattering and absorption) between the metallic nanoparticles in the shell and dielectric cores. Experimentally it was demonstrated that plasmonic meta-structures are able to suppress scattering for a broad wavelength range of incident light. Numerically, the plasmonic meta-structure presented in this dissertation could suppress angular sidelobes and increase the scattering anisotropy. Thus, experimental and numerical studies support the claim that plasmonic meta-structures are a potential candidate for practical applications in high-resolution imaging and increase the signal-to-noise ratio in optical detection.

Appendix A: computational model

We use the MFS to compute the interior field inside the core, ψ^{int}. In the whole space composed of a uniform medium with wavenumber k_1, Green's function,

$$G_1(r - r') = \frac{e^{ik_1|r-r'|}}{4\pi|r-r'|} \tag{A1}$$

Gives a spherical wave centered at r'. We use the Fibonacci lattice[177] to compute boundary points $r_j \in B$ for $j = 1, \dots, M$ which are approximately uniformly distributed on the surface of the sphere. Then, we set

$$r_j^{int} = r_j + l\,\hat{v}_j,\ j = 1, \dots, M. \tag{A2}$$

With $\hat{v}_j$ denoting the unit outward normal at r_j, and $l > 0$ denoting a user-defined length parameter. In our simulations, we have set $l = 0.125d$. According to Eq(A2), r_j^{int} for $j = 1, \dots, M$ lie outside of the sphere. Using these points, we form the following approximation.

$$\psi^{int}(r) \approx \sum_{j=1}^{M} c_j^{int} G_1\left(r - r_j^{int}\right), \quad r \in D. \tag{A3}$$

Equation (A3) approximate ψ^{int} as a superposition of finitely many spherical waves centered at points located outside of D. Therefore, it is exactly satisfies Eq (4.1).

We compute the exterior field, ψ^{ext} using the sum,

$$\psi^{ext} = \psi^{inc} + \psi^{B} + \sum_{n=1}^{N} \Psi_n$$
(A4)

with ψ^B denoting the field scattered by the dielectric sphere and Ψ_n denoting the filed scattered by the *n*th metal nanoparticle. Green's function,

$$G_0(r - r') = \frac{e^{ik_0|r-r'|}}{4\pi|r-r'|} \tag{A5}$$

Gives a spherical wave centered at r' propagating in the whole space with wavenumber k_0. Just as we have done in Eq (A2), we set

$r_j^{ext} = r_j - l\hat{v}_j, \;\; j = 1, \dots, M.$
(A6)

It follows that r_j^{ext} for $j = 1, \dots, M$ lie inside the sphere. Consequently, the approximation given by

$\psi^B(r) \approx \; \sum_{j=1}^{M} c_j^{ext} G_0(r - r_j^{ext})$
(A7)

exactly satisfies

$$(\nabla^2 + k_0^2)\psi^B = 0, r \in E. \qquad \text{(A8)}$$

Let r_n^{NP} denote the center of the nth AuNP whose scattering amplitude is α_n. The filed scattered by the n*th* AuNP is then given by

$\Psi_n = \alpha_n G_0(r - r_n^{NP})\Psi_E(r_n^{NP}),$
(A9)

with $\Psi_E(r_n^{NP})$ denoting the exciting filed at r_n^{NP}. This exciting field is given as the sum,

$\Psi_E(r_n^{NP}) = \psi^{inc}(r_n^{NP}) + \psi^B(r_n^{NP}) + \; \sum_{\substack{n'=1 \\ n' \neq n}}^{N} \alpha_{n'} G_0\big(r_n^{NP} - r_{n'}^{NP}\big)\Psi_E(r_{n'}^{NP}).$
(A10)

Equation (A10) gives the exciting field at r_n^{NP} as the sum of the incident filed ψ^{inc} , the field scattered by the dielectric sphere ψ^B, and the fields scattered by all of the other $N - 1$ metal nanoparticles evaluated at r_n^{NP}.

In the expression for $\psi^{int}, \psi^B,$ and Ψ_n given by Eqs. (A3), (A7), and (A9), respectively, the quantities c_j^{int} for $j = 1, \dots, M,$ c_j^{ext} for $j = 1, \dots, M,$ and $\Psi_E(r_n)$ for $n = 1, \dots, N$ are to be determined. We find them using interface conditions Eqs. (3) and (4). By requiring that interface condition Eq(3) is satisfied exactly on the M boundary points, $r_j \in B$ for $i = 1, \dots, M,$ we find that

$$\sum_{j=0}^{M} c_j^{int} G_1\big(r_i - r_j^{int}\big) - \sum_{j=1}^{M} c_j^{ext} G_0\big(r_j - r_j^{ext}\big) - \sum_{n=1}^{N} \alpha_n G_0(r_i - r_n^{NP})\Psi_E(r_n^{NP}) = \psi^{inc}(r_i), \; i = 1, \dots, M. \qquad \text{(A11)}$$

Similarly, by requiring that boundary condition Eq (4) is satisfied exactly on the M boundary points, we find that

$$\sum_{j=0}^{M} c_j^{int} \partial_v G_1\big(r_i - r_j^{int}\big) - \sum_{j=1}^{M} c_j^{ext} \partial_v G_0\big(r_i - r_j^{ext}\big) - \; \sum_{n=1}^{N} \alpha_n \partial_v G_0(r_i - r_n^{NP})\Psi_E(r_n^{NP}) = \partial_v \psi^{inc}(r_i), \; i = 1, \dots, M. \qquad \text{(A12)}$$

Finally, by substituting Eq. (A7) into Eq (A10) and rearranging terms, we find that

$$\Psi_E(r_n^{NP}) - \sum_{\substack{n'=1 \\ n'\neq n}}^{N} \alpha_{n'} G_0\left(r_n^{NP} - r_{n'}^{NP}\right)\Psi_E\left(r_{n'}^{NP}\right) - \sum_{j=1}^{M} c_j^{ext} G_0\left(r_n^{NP} - r_j^{ext}\right) = \psi^{inc}(r_n),$$
$$n = 1, \dots, N \qquad \text{(A13)}$$

Equations (A11), (A12), and (A13) give $2MN$ equations for the $2MN$ unknows: c_j^{int} for $j = 1, \dots, M$, c_j^{ext} for $j = 1, \dots, M$, and $\Psi_E(r_n^{NP})$ for $n = 1, \dots, N$. These equations can be combined to form a $2MN \times 2MN$ linear systems that is solved standard numerical linear algebra methods.

Appendix B: computing the total scattering cross-section

Upon solution of the linear system comprised of Eqs. (A11)−(A13) given above, the scattered field is given by

$$\psi^s(r) = \psi^B + \sum_{j=1}^{N} \Psi_n \approx \sum_{j=1}^{M} c_j^{ext} G_0\left(r - r_j^{ext}\right) + \sum_{n=1}^{N} \alpha_n G_0(r - r_n^{NP})\Psi_E(r_n^{NP}), r \in E.$$
(B1)

The scattered field evaluated at $r = R\hat{o}$ with $R = |r|$ and $\hat{o} = r/|r|$ in the far-field corresponding to $R \gg 1$behaves like a spherical wave and is given by [2], [3], [173], [175]

$$\psi^s(r) \sim f(\hat{o}, \hat{\imath})\frac{e^{ik_0 R}}{R} \qquad \text{(B2)}$$

Here, $f(\hat{o}, \hat{\imath})$ is the scattering amplitude for the scattered field in the far field in direction $\hat{o}$ when the particle is illuminated by a plane wave propagating in the direction $\hat{\imath}$ with unit amplitude.

Suppose we have set ψ^{inc} to be a plane wave unit amplitude propagating in direction $\hat{\imath}$ and we have used that to compute the solution of Eqs. (A11) – (A13). Using $|R\hat{o} - r'| \sim R - \hat{o}.r'$ for $R \gg 1$, the far-field Green's function [2], [3], [173], [175] is

$$G_0(R\hat{o} - r') \sim e^{ik_0 \hat{o}.r'}\frac{e^{ik_0 R}}{4\pi R}, R \gg 1 \qquad \text{(B3)}$$

Replacing G_0 by Eq (B3) in Eq. (B1) yields

$$\psi^s(r) \sim \left[\frac{1}{4\pi}\sum_{j=1}^{M} c_j^{ext} e^{ik_0 \hat{o}.r_j^{ext}} + \sum_{n=1}^{N} \alpha_n e^{ik_0 \hat{o}.r_n^{NP}} \Psi_E(r_n^{NP})\right]\frac{e^{ik_0 R}}{R}, R >> 1$$
(B4)

By comparing Eq (B2) with Eq (B4), we find that the scattering amplitude using our method is given by

$$f(\hat{o},\hat{\imath}) \approx \frac{1}{4\pi}\sum_{j=1}^{M} c_j^{ext} e^{ik_o \hat{o}.r_j^{ext}} + \frac{1}{4\pi}\sum_{n=1}^{N} \alpha_n e^{1k_0 \hat{o}.r_n^{NP}} \Psi_E(r_n^{NP}). \tag{B5}$$

According to the Optical Theorem or forward scattering theorem [2], [3], [173], [175], we can compute the total cross-section σ_t of the scattering structure through evaluation of

$$\sigma_t = \frac{4\pi}{k_0}\, Im\,[f(\hat{\imath},\hat{\imath})]. \tag{B6}$$

We compute the total cross-section by substituting Eq (B5) into this formula. Remarkably, Eq (B6) allows for the determination of σ_t by only measuring the power scattered in the forward direction.

Appendix C : computer codes

Broadband scattering suppression using 3D nano-assembled plasmonic meta-structure

---

The codes below contain the complete computational work regarding the project on Broadband scattering suppression using 3D nanoassembled meta-structures. These codes are written in Python and optimized for Jupyter Notebook.

```
import  time
print( 'Last updated: %s' %time.strftime('%d/%m/%Y') )
```

```
Last updated: 06/09/2021
```

```
# defaults for the codes below

import numpy as np
import matplotlib.pyplot as plt
```

A. Compute the points needed for the method of fundamental solutions

```
def ComputeMFSPoints( a0, M ):
    """
    This function computes the set of points needed for the method of fundamental solutions (MFS).
    In particular, given the radius of a sphere, a0, and the number of points M, this function computes
    the Fibonnaci lattice on the unit sphere and stores them as the unit normal vectors v. Using v, we
    then compute ρ_bdy = a0 * v, ρ_int = ( a0 + ℓ ) * v, and ρ_ext = ( a0 - ℓ ) * v.

    This function outputs four vectors: v, ρ_bdy, ρ_int, and ρ_ext.
    """

    # allocate memory for the Fibonacci lattice points on the unit sphere

    v = np.full( ( M, 3 ), float( 'nan' ) )

    # compute the "golden angle"

    golden_angle = np.pi * ( 3 - np.sqrt( 5 ) )

    # compute the points on the unit sphere

    v[:,2] = ( 1 - 1 / M ) * ( 1 - 2 * np.arange( 0, M ) / ( M - 1 ) )

    ρ = np.sqrt( 1 - v[:,2] ** 2 )
    θ = golden_angle * np.arange( 0, M )

    v[:,0] = ρ * np.cos( θ )
    v[:,1] = ρ * np.sin( θ )

    # compute the boundary points, interior points, and exterior points

    ℓ = 0.25 * a0

    ρ_bdy = a0 * v
    ρ_int = ( a0 + ℓ ) * v
    ρ_ext = ( a0 - ℓ ) * v

    return v, ρ_bdy, ρ_int, ρ_ext;
```

B. Compute the positions of the point scatterers(plasmonic nanoparticles)

```
def Coordinates(CoreDia, NPDia, Vff):

  #this part of the code takes user input to initiate computation
  #print('Insert Silica core diameter')
  #CoreDia = np.double(input())
  #print('Insert nanoparticle diameter')
  #NPDia = np.double(input())
  #print('Inser ligand length')
    LigLen = 0.9800
  #print('Insert volume filling fraction')
  #Vff = np.double(input())
    ShellThickness = NPDia * 3
  # Physical space taken by a satelite sphere
  # Physical space taken by a satelite sphere

    R = (NPDia / 2 + LigLen)

    SmallSphereRadius = R
    ShellOuterRad = CoreDia /2  + ShellThickness
    ShellInnerRadius = CoreDia/2

    #Vs = (4/3)* np.pi * (R ** 3)
  #Floor returns rounding to nearest highest value of the floating numb
er
    ND = np.floor((ShellOuterRad ** 3 - ShellInnerRadius**3) / (R**3) *
Vff)
    N = np.int(ND) # Number of nanoparticles in integre
  #This part of the code calcuates random distributions of the coordina
tes of the
  #Allocating memory for coordinates
    R_N = np.full((N,3), float('nan'))
  # Allocating memory for specific nanoparticles coordinates
    Xcoord = np.full((N,1), float('nan'))
    Ycoord = np.full((N,1), float('nan'))
    Zcoord = np.full((N,1), float('nan'))
    for i in range(N):
        t = 2 * np.pi * np.random.rand() #Elevation angle
        p = np.arccos(2* np.random.rand()-1) # Azimuthal Angle
        dr = ShellInnerRadius +(np.random.rand())**(1/3) * (ShellOuterR
ad - ShellInnerRadius) # Distance along z
        Xcoord[i] = dr * np.cos(t) * np.sin(p)
        Ycoord[i] = dr * np.sin(t) * np.sin(p)
        Zcoord[i] = dr * np.cos(p)
        I = []
        # finding vacancies and checking for overlap
        NoLap = 0 # Seting overlap flag
        #m = 0;
        #Compute distances between the naoparticles
```

```
        if i > 1 :

            dist = np.sqrt((Xcoord - Xcoord[i])**2 + (Ycoord - Ycoord[i])**2 + (Zcoord - Zcoord[i])**2)
           #looking for the overlap
            idx = [idx for idx in range(i)]
            I = np.where(dist[idx] < SmallSphereRadius)
            I = np.asanyarray(I)
            if I.size == 0:
                NoLap = 0 #No overlap
            else:
                NoLap = 1 # Overlap Present
        if NoLap == 1:
            while NoLap == 1:

                t = 2 * np.pi * np.random.rand() #Elevation angle
                p = np.arccos(2* np.random.rand()-1) # Azimuthal Angle
                dr = ShellInnerRadius +(np.random.rand())**(1/3) * (ShellOuterRad - ShellInnerRadius )
                Xcoord[i] = dr * np.cos(t) * np.sin(p)
                Ycoord[i] = dr * np.sin(t) * np.sin(p)
                Zcoord[i] = dr * np.cos(p)
                dist = np.sqrt((Xcoord - Xcoord[i])**2 + (Ycoord - Ycoord[i])**2 + (Zcoord - Zcoord[i])**2)
                idx = [idx for idx in range(i)]
                I = np.where(dist[idx] < SmallSphereRadius)
                I = np.asanyarray(I)
                if I.size == 0:
                    NoLap = 0
                else:
                    NoLap = 1

        X_coords = Xcoord
        Y_coords = Ycoord
        Z_coords = Zcoord


    R_N[:,0:1] = X_coords
    R_N[:,1:2] = Y_coords
    R_N[:,2:3] = Z_coords



    return R_N;


def RayleighAlpha(R, WL, n, K):
      #refractive_index_data = ('gold_11nm_silica_film.csv') # loads .csv data
```

```
      #RawData = open(refractive_index_data,'rt') # Data filec processed
      #Data = np.loadtxt(RawData, delimiter=",") # Data now in CSV format
      #WL = Data[:,0] # Wavelength over which the computation takes place
      #n  = Data[:,1] # Refractive index of plasmonic gold nanoparticles
      #K  = Data[:,2] # Extinction of the plasmonic gold nanoparticles
      #nb = 1.0 # Refractive index of the Background medium
      N = np.zeros(1, dtype=complex)
      m = np.zeros(1,dtype=complex)
      K0 = np.zeros(1,dtype=complex)
      sigma_s = np.zeros(1,dtype=complex)
      sigma_abs = np.zeros(1,dtype=complex)
      sigma_t = np.zeros(1,dtype=complex)
      alpha_imag = np.zeros(1,dtype=complex)
      alpha_r = np.zeros(1,dtype=complex)
      alphaN = np.zeros(1,dtype=complex)
      # R Radius of the nanoparticle

      N = np.complex(n,K)
      m = N / nb
      K0 = (2 * np.pi / WL)
      sigma_s = (((2*np.pi**5/3)*((2*R)**6)*(np.absolute((m**2-1)/(m**2+2)))**2) /(WL**4))
      sigma_abs = ((((8*np.pi**2)*(1/WL)*R**3*np.imag((m**2-1)/(m**2+2)))))
      sigma_t = sigma_s+ sigma_abs
      alpha_imag = (K0)*sigma_t
      alpha_r = np.absolute(np.sqrt((4*np.pi*sigma_s) - K0*alpha_imag**2))
      alphaN = (4*np.pi)*(alpha_r + 1j*alpha_imag)

      return alphaN;
```

C. Computing Green's function and its normal derivative

```
# function to compute Green's function

def ComputeG( k, Rd ):
    """
    This function computes the whole space Green's function given a wavenumber k and a distance Rd.
```

```
    The output of this function is the evaluation of the whole space Gr
een's function.
    """

    # compute Green's function

    G = np.exp( 1j * k * Rd ) / ( 4 * np.pi * Rd )

    return G;

# function to compute the normal derivative of Green's function

def ComputeDvG( k, Rd, CosTheta ):
    """
    This function computes the normal derivative of the whole space Gre
en's function
    given a wavenumber k, a distance Rd, and the cosine of the angle ma
de between the
    difference vector and the unit normal.

    The output of this function is the evaluation of the normal derivat
ive of the whole
    space Green's function.
    """

    # compute Green's function

    G = ComputeG( k, Rd )

    # compute the normal derivative of Green's function

    DvG = CosTheta * ( 1j * k - 1 / Rd ) * G

    return DvG;
```

D. Compute the MFS expansion coefficients and Foldy-Lax exciting fields.

```
def ComputeExpansionCoefficientsExcitingFields( k0, k1, a0, v, ρ_bdy, ρ
_int, ρ_ext, α, R_N, M, N ):


    # interior points
```

```
    indx, jndx = np.meshgrid( np.arange(0,M), np.arange(0,M) )

    R_int = np.sqrt( ( ( ρ_bdy[indx] - ρ_int[jndx] ) ** 2 ).sum( axis =
2 ) )
    μ_int = np.divide(( v[indx] * ( ρ_bdy[indx] - ρ_int[jndx] ) ).sum(
axis = 2 ), R_int)

    # exterior points

    R_ext = np.sqrt( ( ( ρ_bdy[indx] - ρ_ext[jndx] ) ** 2 ).sum( axis =
2 ) )
    μ_ext = np.divide(( v[indx] * ( ρ_bdy[indx] - ρ_ext[jndx] ) ).sum(
axis = 2 ) , R_ext)

    # Foldy-Lax points

    indx, jndx = np.meshgrid( np.arange(0,M), np.arange(0,N) )

    ρ_bdy2RN = np.sqrt( ( ( ρ_bdy[indx] - R_N[jndx] ) ** 2 ).sum( axis
= 2 ) )
    μ_RN     = np.divide(( v[indx] * ( ρ_bdy[indx] - R_N[jndx] ) ).sum(
axis = 2 ), ρ_bdy2RN)
    RN2ρ_ext = np.sqrt( ( ( ρ_ext[indx] - R_N[jndx] ) ** 2 ).sum( axis
= 2 ) )

    indx, jndx = np.meshgrid( np.arange(0,N), np.arange(0,N) )

    RN2RN    = np.sqrt( ( ( R_N[indx] - R_N[jndx] ) ** 2 ).sum( axis =
2 ) )

    # compute the incident field and its normal derivative on the M bou
ndary points

    Ψ_inc   = np.exp( 1j * k0 * ρ_bdy[:,2] )
    DvΨ_inc = 1j * k0 * np.multiply( v[:,2], Ψ_inc )

    # compute the incident field on the N point scatterers

    Ψ_inc4FL = np.exp( 1j * k0 * R_N[:,2] )

    # compute the matrix blocks

    A11 =  ComputeG( k1, R_int )
    A12 = - ComputeG( k0, R_ext )
    A13 = -α * ComputeG( k0, ρ_bdy2RN ).T

    A21 =  ComputeDvG( k1, R_int, μ_int )
    A22 = - ComputeDvG( k0, R_ext, μ_ext )
```

```
    A23 = - α * ComputeDvG( k0, ρ_bdy2RN, μ_RN ).T

    A31 = np.zeros( ( N, M ), dtype ='complex' )
    A32 = - ComputeG( k0, RN2ρ_ext )

    A33 = np.zeros( ( N, N ), dtype = 'complex')
    offdiags = np.where( RN2RN != 0 )
    A33[offdiags] = -α * ( np.exp( 1j * k0 * RN2RN[offdiags]  ) / ( 4 *
np.pi * RN2RN[offdiags] ) )
    #A33 = -α * np.divide( np.exp( 1j * k0 * RN2RN ), ( 4 * np.pi * RN2
RN ) )
    A33 += np.eye( N, dtype = 'complex' )

    # form the linear system of equations

    A = np.block( [ [ A11, A12, A13 ], [ A21, A22, A23 ], [ A31, A32, A
33 ] ] )
    b = np.block( [ Ψ_inc, DvΨ_inc, Ψ_inc4FL ] )

    # solve the linear system

    c = np.linalg.solve( A, b )

    # parse the solution

    c_int = c[0:M]
    c_ext = c[M:2*M]
    Ψ_E   = c[2*M:2*M*N]

    return c_int, c_ext, Ψ_E;

def ComputeMFSExpansionCoefficients( k0, k1, a0, v, ρ_bdy, ρ_int, ρ_ext
, M ):
    """
    This function solves the 2M x 2M system of equations for the MFS ex
pansion coefficients.

    This code requires the results from ComputeMFSPoints, namely v, ρ_b
dy, ρ_int, and ρ_ext, in
    addition to the two wavenumbers k0 and k1, the sphere radius, a0, a
nd the number of MFS points,
    M.

    The output from this code are the 2 M-vectors, c_int and c_sca, cor
responding to the MFS
    expansions for the interior and scattered fields, respectively.
    """

    # interior points
```

```
    indx, jndx = np.meshgrid( np.arange(0,M), np.arange(0,M) )

    R_int = np.sqrt( ( ( ρ_bdy[indx] - ρ_int[jndx] ) ** 2 ).sum( axis = 2 ) )
    μ_int = ( v[indx] * ( ρ_bdy[indx] - ρ_int[jndx] ) ).sum( axis = 2 ) / R_int

    # exterior points

    R_ext = np.sqrt( ( ( ρ_bdy[indx] - ρ_ext[jndx] ) ** 2 ).sum( axis = 2 ) )
    μ_ext = ( v[indx] * ( ρ_bdy[indx] - ρ_ext[jndx] ) ).sum( axis = 2 ) / R_ext

    # compute the incident field and its normal derivative on the M boundary points

    Ψ_inc   = np.exp( 1j * k0 * ρ_bdy[:,2] )
    DvΨ_inc = 1j * k0 * np.multiply( v[:,2], Ψ_inc )

    # compute the matrix blocks

    A11 =  ComputeG( k1, R_int )
    A12 = -ComputeG( k0, R_ext )

    A21 =  ComputeDvG( k1, R_int, μ_int )
    A22 = -ComputeDvG( k0, R_ext, μ_ext )

    # form the linear system of equations

    A = np.block( [ [ A11, A12 ], [ A21, A22 ] ] )
    b = np.block( [ Ψ_inc, DvΨ_inc ] )

    # solve the linear system

    c = np.linalg.solve( A, b )

    # parse the solution

    c_int0 = c[0:M]
    c_ext0 = c[M:2*M]

    return c_int0, c_ext0;
```

E. Computing the total cross section

```
def ComputeTotalCrossSection( k0, k1, a0, v, ρ_bdy, ρ_int, ρ_ext, α, R_N, M, N ):
    """
    This function computes the total cross-section by evaluating the Optical Theorem using
    the results from the MFS approximation for the scattered field.
    """

    # compute the MFS expansion coefficients

    c_int, c_ext, Ψ_E = ComputeExpansionCoefficientsExcitingFields( k0, k1, a0, v, ρ_bdy, ρ_int, ρ_ext, α, R_N, M, N )

    # compute the scattering amplitude

    f1 = (0.25 / np.pi)  * np.exp( -1j * k0 * ρ_ext[:,2] ).T @ c_ext
    f2 = (0.25 / np.pi ) * α * np.exp( -1j * k0 * R_N[:,2] ).T @ Ψ_E

    # compute the scattering cross-section

    σ_t = 4 * np.pi * np.imag( f1 + f2 ) / k0

    return σ_t;

def ComputeTotalCrossSectionMFS( k0, k1, a0, v, ρ_bdy, ρ_int, ρ_ext, M ):
    """
    This function computes the total cross-section by evaluating the Optical Theorem using
    the results from the MFS approximation for the scattered field.
    """

    # compute the MFS expansion coefficients

    c_int, c_sca = ComputeMFSExpansionCoefficients( k0, k1, a0, v, ρ_bdy, ρ_int, ρ_ext, M )

    # compute the scattering amplitude

    f = 0.25 / np.pi * np.exp( -1j * k0 * ρ_ext[:,2] ).T @ c_sca

    # compute the scattering cross-section

    σ_t = 4 * np.pi * np.imag( f ) / k0

    return σ_t;
```

6 Compute and plot the total cross-section over the visible spectrum

```
#Here we upload data file containng refractive index and
#extinction values of the plasmoninc gold nanoparticles and Silica.
#The wavelength dependent optical parameters of plasmoninc gold nano pa
rticles.
#The included file (11nm_gold_film_silica.csv)in this project containes
those data .

# **--------***-------****

# Activate the commented line below to upload optical parameter files
#gold_Refractive_index = files.upload() # upload refractive index, exti
nction data for gold NPs and Silica

# **--------***-------****

Refractive_index_data = ('11nm_gold_film_silica.csv') # Data file is av
aialble for use
RawData = open(Refractive_index_data,'rt')
Data = np.loadtxt(RawData, delimiter=",") # Processed data file
Wavelength = np.asarray(Data[:,0]) # Wavelength over which the computat
ion takes place
NPRefndx  = np.asarray(Data[:,1]) # Refractive index of plasmonic gold
nanoparticles
NPExtinction  = np.asarray(Data[:,2]) # Extinction of the plasmonic gol
d nanoparticles
Silica_refndx = Data[:,3] # Refractive index of interior or dielectric
core
nb = 1.0 # Refractive index of the Background medium

#Core (dielectric) diameter

CoreDia = 690

#Dielectric core radius

a0 = CoreDia/2

#Plasmonic nanoparticles Dia

NPDia = 20

R = NPDia / 2 #radius of plasmonic NP
```

```
#Set the filling fraction of NPs in the shell

Vff = 0.10

#Compute the geometric cross-section

σ_g = np.pi * a0 ** 2 # bare core
σ_g_cs = np.pi * (a0+NPDia*3) ** 2 # core-shell


# Set refractive index

k0 = nb # Refractive index exterior or the background

#Set the number of MFS points

M = 512

#Compute the MFS points

v, ρ_bdy, ρ_int, ρ_ext = ComputeMFSPoints( a0, M )

# Generate the point scatteres position

R_N = Coordinates(CoreDia, NPDia, Vff)

# allocate memory for the total cross-sections

σ_t0 = np.full( ( len(Wavelength), 1 ), 'nan', dtype = 'float' )
σ_s  = np.full( ( len(Wavelength), 1 ), 'nan', dtype = 'float' )

N = len(R_N) # number of nanoparticles in the shell volume

for i in range(len(Wavelength)):
    WL = Wavelength[i]
    n = NPRefndx[i]
    K = NPExtinction[i]
    α = RayleighAlpha(R, WL, n, K)
    k0 = (2*np.pi/WL)*nb
    k1 = (2*np.pi/WL)*Silica_refndx[i]

  #Compute the MFS results for a Bare core and a core-shell plasmonic m
eta structure

    σ_t0[i] = ComputeTotalCrossSectionMFS( k0, k1, a0, v, ρ_bdy, ρ_int,
ρ_ext, M )
    σ_s[i]  = ComputeTotalCrossSection( k0, k1, a0, v, ρ_bdy, ρ_int, ρ_
```

```
ext, α, R_N, M, N )


# plot the results

plt.rcParams['figure.figsize'] = [12,8]

plt.plot( Wavelength, σ_t0 / σ_g, Wavelength, σ_s / σ_g , '--'  )
plt.xlabel( r'$\lambda$ (nm)', fontsize = 24 )
plt.ylabel( r'$\sigma_{s}/\sigma_{g}$', fontsize = 24 )
plt.legend( ( 'Bare Core', 'Core-shell Meta structure' ),  fontsize = 2
4 )
plt.grid()

plt.show()
```

Scattered E-filed computation and plot

```
# compute the scattered field on the xy-, xz-, and yz-planes

def ComputeScatteredField( k0, ρ_ext, c_sca, X1, X2 ):

    # compute distances

    Rdiff_xy = np.sqrt( ( X1 - ρ_ext[:,0] ) ** 2 + ( X2 - ρ_ext[:,1] )
** 2 + ρ_ext[:,2] ** 2 )
    Rdiff_xz = np.sqrt( ( X1 - ρ_ext[:,0] ) ** 2 + ρ_ext[:,1] ** 2 + (
X2 - ρ_ext[:,2] ) ** 2 )
    Rdiff_yz = np.sqrt( ρ_ext[:,0] ** 2 + ( X1 - ρ_ext[:,1] ) ** 2 + (
X2 - ρ_ext[:,2] ) ** 2 )

    # compute the scattered field on the xy-, xz-, and yz-planes

    Uxy = np.exp( 1j * k0 * Rdiff_xy ) / ( 4 * np.pi * Rdiff_xy ) @ c_s
ca
    Uxz = np.exp( 1j * k0 * Rdiff_xz ) / ( 4 * np.pi * Rdiff_xz ) @ c_s
ca
    Uyz = np.exp( 1j * k0 * Rdiff_yz ) / ( 4 * np.pi * Rdiff_yz ) @ c_s
ca

    return Uxy, Uxz, Uyz;

# compute the interior field on the xy-, xz-, and yz-planes

def ComputeInteriorField( k1, ρ_int, c_int, X1, X2 ):

    # compute distances
```

```
    Rdiff_xy = np.sqrt( ( X1 - ρ_int[:,0] ) ** 2 + ( X2 - ρ_int[:,1] ) ** 2 + ρ_int[:,2] ** 2 )
    Rdiff_xz = np.sqrt( ( X1 - ρ_int[:,0] ) ** 2 + ρ_int[:,1] ** 2 + ( X2 - ρ_int[:,2] ) ** 2 )
    Rdiff_yz = np.sqrt( ρ_int[:,0] ** 2 + ( X1 - ρ_int[:,1] ) ** 2 + ( X2 - ρ_int[:,2] ) ** 2 )

    # compute the scattered field on the xy-, xz-, and yz-planes

    Uxy = np.exp( 1j * k1 * Rdiff_xy ) / ( 4 * np.pi * Rdiff_xy ) @ c_int
    Uxz = np.exp( 1j * k1 * Rdiff_xz ) / ( 4 * np.pi * Rdiff_xz ) @ c_int
    Uyz = np.exp( 1j * k1 * Rdiff_yz ) / ( 4 * np.pi * Rdiff_yz ) @ c_int

    return Uxy, Uxz, Uyz;

from ipywidgets import interact

# set the size of the plots

plt.rcParams['figure.figsize'] = [20,6]

# set the values of λ to display

dict_comp = {"{} nm".format(Wavelength[wavelength]):wavelength for wavelength in range(len(Wavelength)) }

# compute the evaluation mesh

NN = 256

X1plot, X2plot = np.meshgrid( a0 * np.linspace( -10, 10, NN ), a0 * np.linspace( -10, 10, NN ) )

# plot the fields for each wavelength

@interact( wavelength = dict_comp )
def fun( wavelength = 0 ):

    # compute the wavenumbers

    k0 = 2 * np.pi / Wavelength[wavelength] * nb
    k1 = 2 * np.pi / Wavelength[wavelength] * Silica_refndx[wavelength]

    # compute the MFS expansion coefficients
```

```
    c_int, c_sca = ComputeMFSExpansionCoefficients( k0, k1, a0, v, ρ_bd
y, ρ_int, ρ_ext, M )

    # allocate memory for Uxy, Uxz, and Uyz

    Uxy = np.full( ( NN, NN ), 'nan', dtype = 'complex' )
    Uxz = np.full( ( NN, NN ), 'nan', dtype = 'complex' )
    Uyz = np.full( ( NN, NN ), 'nan', dtype = 'complex' )

    for i in range( NN ):

        for j in range( NN ):

            # compute the radial distance of the evaluation point

            R = np.sqrt( X1plot[i,j] ** 2 + X2plot[i,j] ** 2 )

            # compute the fields

            if R < a0:

                Uxy[i,j], Uxz[i,j], Uyz[i,j] = ComputeInteriorField( k1
, ρ_int, c_int, X1plot[i,j], X2plot[i,j] )

            else:

                Uxy[i,j], Uxz[i,j], Uyz[i,j] = ComputeScatteredField( k
0, ρ_ext, c_sca, X1plot[i,j], X2plot[i,j] )

    # plot the fields

    plt.subplot(1,3,1)
    plt.pcolormesh( X1plot / a0, X2plot / a0, np.real( Uxy ), vmin=-1,
vmax=1, cmap='cividis'  )
    plt.colorbar()
    plt.gca().set_aspect('equal', adjustable='box')
    plt.draw()
    plt.tight_layout()
    plt.xlabel( 'x', fontsize=18 )
    plt.ylabel( 'y', fontsize=18 )
    plt.title( 'field on the xy-plane', fontsize=20 )

    plt.subplot(1,3,2)
    plt.pcolormesh( X1plot / a0, X2plot / a0, np.real( Uxz ), vmin=-1,
vmax=1, cmap='cividis'  )
    plt.colorbar()
    plt.gca().set_aspect('equal', adjustable='box')
    plt.draw()
```

```
    plt.tight_layout()
    plt.xlabel( 'x', fontsize=18 )
    plt.ylabel( 'z', fontsize=18 )
    plt.title( 'field on the xz-plane', fontsize=20 )

    plt.subplot(1,3,3)
    plt.pcolormesh( X1plot / a0, X2plot / a0, np.real( Uyz ), vmin=-1,
vmax=1, cmap='cividis'  )
    plt.colorbar()
    plt.gca().set_aspect('equal', adjustable='box')
    plt.draw()
    plt.tight_layout()
    plt.xlabel( 'y', fontsize=18 )
    plt.ylabel( 'z', fontsize=18 )
    plt.title( 'field on the yz-plane', fontsize=20 )

    plt.show()
```

References

[1] M. I. Khan, S. Ghosh, R. Baxter, and A. D. Kim, “Modeling broadband cloaking using 3D nano-assembled plasmonic meta-structures,” *Opt. Express*, vol. 28, no. 15, p. 22732, 2020, doi: 10.1364/oe.395840.

[2] H. C. Hulst and H. C. van de Hulst, *Light Scattering by Small Particles*. Dover Publications, 1981.

[3] C. F. Bohren, *Absorption and scattering of light by small particles*. 1983.

[4] A. L. Aden and M. Kerker, “Scattering of electromagnetic waves from two concentric spheres,” *J. Appl. Phys.*, vol. 22, no. 10, pp. 1242–1246, 1951, doi: 10.1063/1.1699834.

[5] X. Fan, W. Zheng, and D. J. Singh, “Light scattering and surface plasmons on small spherical particles,” *Light Sci. Appl.*, vol. 3, no. November 2013, pp. 1–14, 2014, doi: 10.1038/lsa.2014.60.

[6] W. Hergert and T. Wriedt, “The Mie Theory,” *Mie Theory Basics Appl.*, pp. 53–71, 2012, doi: 10.1007/978-3-642-28738-1.

[7] M. Nieto-Vesperinas, “Fundamentals of Mie scattering,” in *Woodhead Publishing Series in Electronic and Optical Materials*, I. Brener, S. Liu, I. Staude, J. Valentine, and C. B. T.-D. M. Holloway, Eds. Woodhead Publishing, 2020, pp. 39–72.

[8] S. A. Maier, *Plasmonics: Fundamentals and Applications*. Springer US, 2007.

[9] D. Schaming and H. Remita, “Nanotechnology: from the ancient time to nowadays,” *Found. Chem.*, vol. 17, no. 3, pp. 187–205, 2015, doi: 10.1007/s10698-015-9235-y.

[10] A. Vincenzo, P. Roberto, F. Marco, M. M. Onofrio, and I. Maria Antonia,

“Surface plasmon resonance in gold nanoparticles: a review,” *J. Phys. Condens. Matter*, vol. 29, no. 20, p. 203002, 2017, [Online]. Available: http://stacks.iop.org/0953-8984/29/i=20/a=203002.

[11] N. Ashcroft and N. Mermin, *Solid State Physics*. 1976.

[12] J. D. Jackson 1925-2016, *Classical electrodynamics*. Third edition. New York : Wiley, [1999] ©1999.

[13] M. Fox, “Optical Properties of Solids,” *Am. J. Phys.*, vol. 70, no. 12, pp. 1269–1270, Nov. 2002, doi: 10.1119/1.1691372.

[14] K. A. Willets and R. P. Van Duyne, “Localized Surface Plasmon Resonance Spectroscopy and Sensing,” *Annu. Rev. Phys. Chem.*, vol. 58, no. 1, pp. 267–297, 2007, doi: 10.1146/annurev.physchem.58.032806.104607.

[15] W. L. Barnes, A. Dereux, and T. W. Ebbesen, “Surface plasmon subwavelength optics,” *Nature*, vol. 424, no. 6950, pp. 824–830, 2003, doi: 10.1038/nature01937.

[16] S. A. Maier, M. L. Brongersma, P. G. Kik, and H. A. Atwater, “Observation of near-field coupling in metal nanoparticle chains using far-field polarization spectroscopy,” *Phys. Rev. B*, vol. 65, no. 19, p. 193408, May 2002, doi: 10.1103/PhysRevB.65.193408.

[17] S. A. Maier, P. G. Kik, and H. A. Atwater, “Observation of coupled plasmon-polariton modes in Au nanoparticle chain waveguides of different lengths: Estimation of waveguide loss,” *Appl. Phys. Lett.*, vol. 81, no. 9, pp. 1714–1716, Aug. 2002, doi: 10.1063/1.1503870.

[18] H. L. Offerhaus, B. van den Bergen, M. Escalante, F. B. Segerink, J. P. Korterik, and N. F. van Hulst, “Creating Focused Plasmons by Noncollinear Phasematching on Functional Gratings,” *Nano Lett.*, vol. 5, no. 11, pp. 2144–2148, Nov. 2005, doi: 10.1021/nl0515089.

[19] A. Otto, “Excitation of nonradiative surface plasma waves in silver by the method of frustrated total reflection,” *Zeitschrift für Phys. A Hadron. Nucl.*,

vol. 216, no. 4, pp. 398–410, 1968, doi: 10.1007/BF01391532.

[20] R. B. Pettit, J. Silcox, and R. Vincent, “Measurement of surface-plasmon dispersion in oxidized aluminum films,” *Phys. Rev. B*, vol. 11, no. 8, pp. 3116–3123, Apr. 1975, doi: 10.1103/PhysRevB.11.3116.

[21] S. Park, G. Lee, S. H. Song, C. H. Oh, and P. S. Kim, “Resonant coupling of surface plasmons to radiation modes by use of dielectric gratings,” *Opt. Lett.*, vol. 28, no. 20, pp. 1870–1872, 2003, doi: 10.1364/OL.28.001870.

[22] E. Kretschmann and H. Raether, “Notizen: Radiative Decay of Non Radiative Surface Plasmons Excited by Light,” *Zeitschrift für Naturforsch. A*, vol. 23, no. 12, pp. 2135–2136, 1968, doi: doi:10.1515/zna-1968-1247.

[23] V. Amendola, R. Pilot, and M. Frasconi, “Surface plasmon resonance in gold nanoparticles : a review,” 2017.

[24] S. L. Smitha, K. M. Nissamudeen, D. Philip, and K. G. Gopchandran, “Studies on surface plasmon resonance and photoluminescence of silver nanoparticles,” *Spectrochim. Acta Part A Mol. Biomol. Spectrosc.*, vol. 71, no. 1, pp. 186–190, 2008, doi: https://doi.org/10.1016/j.saa.2007.12.002.

[25] Y. Q. He, S. P. Liu, L. Kong, and Z. F. Liu, “A study on the sizes and concentrations of gold nanoparticles by spectra of absorption, resonance Rayleigh scattering and resonance non-linear scattering,” *Spectrochim. Acta Part A Mol. Biomol. Spectrosc.*, vol. 61, no. 13, pp. 2861–2866, 2005, doi: https://doi.org/10.1016/j.saa.2004.10.035.

[26] W. A. Murray and W. L. Barnes, “Plasmonic Materials,” *Adv. Mater.*, vol. 19, no. 22, pp. 3771–3782, Nov. 2007, doi: https://doi.org/10.1002/adma.200700678.

[27] D. I. Yakubovsky, A. V. Arsenin, Y. V. Stebunov, D. Y. Fedyanin, and V. S. Volkov, “Optical constants and structural properties of thin gold films,” *Opt. Express*, vol. 25, no. 21, p. 25574, 2017, doi: 10.1364/oe.25.025574.

[28] J. N. Anker, W. P. Hall, O. Lyandres, N. C. Shah, J. Zhao, and R. P. Van

Duyne, “Biosensing with plasmonic nanosensors,” *Nat. Mater.*, vol. 7, no. 6, pp. 442–453, 2008, doi: 10.1038/nmat2162.

[29] M. Soler, C. S. Huertas, and L. M. Lechuga, “Label-free plasmonic biosensors for point-of-care diagnostics: a review,” *Expert Rev. Mol. Diagn.*, vol. 19, no. 1, pp. 71–81, Jan. 2019, doi: 10.1080/14737159.2019.1554435.

[30] A. G. Brolo, “Plasmonics for future biosensors,” *Nat. Photonics*, vol. 6, no. 11, pp. 709–713, 2012, doi: 10.1038/nphoton.2012.266.

[31] R. T. Hill, “Plasmonic biosensors,” *WIREs Nanomedicine and Nanobiotechnology*, vol. 7, no. 2, pp. 152–168, Mar. 2015, doi: https://doi.org/10.1002/wnan.1314.

[32] B. Špačková, P. Wrobel, M. Bocková, and J. Homola, “Optical Biosensors Based on Plasmonic Nanostructures: A Review,” *Proc. IEEE*, vol. 104, no. 12, pp. 2380–2408, 2016, doi: 10.1109/JPROC.2016.2624340.

[33] D. Mortazavi, A. Z. Kouzani, A. Kaynak, and W. Duan, “Nano-plasmonic biosensors: A review,” in *The 2011 IEEE/ICME International Conference on Complex Medical Engineering*, 2011, pp. 31–36, doi: 10.1109/ICCME.2011.5876700.

[34] V. E. Bochenkov and T. I. Shabatina, “Chiral Plasmonic Biosensors,” *Biosensors* , vol. 8, no. 4. 2018, doi: 10.3390/bios8040120.

[35] J.-H. Lee, H.-Y. Cho, H. K. Choi, J.-Y. Lee, and J.-W. Choi, “Application of Gold Nanoparticle to Plasmonic Biosensors,” *International Journal of Molecular Sciences* , vol. 19, no. 7. 2018, doi: 10.3390/ijms19072021.

[36] S. Balbinot, A. M. Srivastav, J. Vidic, I. Abdulhalim, and M. Manzano, “Plasmonic biosensors for food control,” *Trends Food Sci. Technol.*, vol. 111, pp. 128–140, 2021, doi: https://doi.org/10.1016/j.tifs.2021.02.057.

[37] S. Nie and S. R. Emory, “Probing Single Molecules and Single Nanoparticles by Surface-Enhanced Raman Scattering,” *Science (80-.).*, vol. 275, no. 5303, pp. 1102–1106, 1997, doi:

10.1126/science.275.5303.1102.

[38] S. Berweger, J. M. Atkin, R. L. Olmon, and M. B. Raschke, “Light on the Tip of a Needle: Plasmonic Nanofocusing for Spectroscopy on the Nanoscale,” *J. Phys. Chem. Lett.*, vol. 3, no. 7, pp. 945–952, Apr. 2012, doi: 10.1021/jz2016268.

[39] J. Lu, W. Wang, S. Wang, X. Shan, J. Li, and N. Tao, “Plasmonic-Based Electrochemical Impedance Spectroscopy: Application to Molecular Binding,” *Anal. Chem.*, vol. 84, no. 1, pp. 327–333, Jan. 2012, doi: 10.1021/ac202634h.

[40] M. Abb, Y. Wang, N. Papasimakis, C. H. de Groot, and O. L. Muskens, “Surface-Enhanced Infrared Spectroscopy Using Metal Oxide Plasmonic Antenna Arrays,” *Nano Lett.*, vol. 14, no. 1, pp. 346–352, Jan. 2014, doi: 10.1021/nl404115g.

[41] A. J. Haes, C. L. Haynes, A. D. McFarland, G. C. Schatz, R. P. Van Duyne, and S. Zou, “Plasmonic Materials for Surface-Enhanced Sensing and Spectroscopy,” *MRS Bull.*, vol. 30, no. 5, pp. 368–375, 2005, doi: DOI: 10.1557/mrs2005.100.

[42] J. P. Camden, J. A. Dieringer, J. Zhao, and R. P. Van Duyne, “Controlled Plasmonic Nanostructures for Surface-Enhanced Spectroscopy and Sensing,” *Acc. Chem. Res.*, vol. 41, no. 12, pp. 1653–1661, Dec. 2008, doi: 10.1021/ar800041s.

[43] R. Adato *et al.*, “Ultra-sensitive vibrational spectroscopy of protein monolayers with plasmonic nanoantenna arrays,” *Proc. Natl. Acad. Sci.*, vol. 106, no. 46, pp. 19227 LP – 19232, Nov. 2009, doi: 10.1073/pnas.0907459106.

[44] O. Pérez-González, N. Zabala, A. G. Borisov, N. J. Halas, P. Nordlander, and J. Aizpurua, “Optical Spectroscopy of Conductive Junctions in Plasmonic Cavities,” *Nano Lett.*, vol. 10, no. 8, pp. 3090–3095, Aug. 2010,

doi: 10.1021/nl1017173.

[45] D. A. Kalashnikov, Z. Pan, A. I. Kuznetsov, and L. A. Krivitsky, “Quantum Spectroscopy of Plasmonic Nanostructures,” *Phys. Rev. X*, vol. 4, no. 1, p. 11049, Mar. 2014, doi: 10.1103/PhysRevX.4.011049.

[46] S. J. Lee, Z. Guan, H. Xu, and M. Moskovits, “Surface-Enhanced Raman Spectroscopy and Nanogeometry: The Plasmonic Origin of SERS,” *J. Phys. Chem. C*, vol. 111, no. 49, pp. 17985–17988, Dec. 2007, doi: 10.1021/jp077422g.

[47] E. J. R. Vesseur, R. de Waele, M. Kuttge, and A. Polman, “Direct Observation of Plasmonic Modes in Au Nanowires Using High-Resolution Cathodoluminescence Spectroscopy,” *Nano Lett.*, vol. 7, no. 9, pp. 2843–2846, Sep. 2007, doi: 10.1021/nl071480w.

[48] A. M. Katzenmeyer, J. Chae, R. Kasica, G. Holland, B. Lahiri, and A. Centrone, “Nanoscale Imaging and Spectroscopy of Plasmonic Modes with the PTIR Technique,” *Adv. Opt. Mater.*, vol. 2, no. 8, pp. 718–722, Aug. 2014, doi: https://doi.org/10.1002/adom.201400005.

[49] S. I. Azzam *et al.*, “Ten years of spasers and plasmonic nanolasers,” *Light Sci. Appl.*, vol. 9, no. 1, p. 90, 2020, doi: 10.1038/s41377-020-0319-7.

[50] Y.-J. Lu *et al.*, “Plasmonic nanolaser using epitaxially grown silver film,” in *2012 Conference on Lasers and Electro-Optics (CLEO)*, 2012, pp. 1–2.

[51] S. Chang and S. L. Chuang, “Fundamental Formulation for Plasmonic Nanolasers,” *IEEE J. Quantum Electron.*, vol. 45, no. 8, pp. 1014–1023, 2009, doi: 10.1109/JQE.2009.2017210.

[52] J. Y. Suh *et al.*, “Plasmonic Bowtie Nanolaser Arrays,” *Nano Lett.*, vol. 12, no. 11, pp. 5769–5774, Nov. 2012, doi: 10.1021/nl303086r.

[53] Q. Zhang *et al.*, “A room temperature low-threshold ultraviolet plasmonic nanolaser,” *Nat. Commun.*, vol. 5, no. 1, p. 4953, 2014, doi: 10.1038/ncomms5953.

[54] P. Melentiev *et al.*, “Plasmonic nanolaser for intracavity spectroscopy and sensorics,” *Appl. Phys. Lett.*, vol. 111, no. 21, p. 213104, Nov. 2017, doi: 10.1063/1.5003655.

[55] A. K. Sarychev and G. Tartakovsky, “Magnetic plasmonic metamaterials in actively pumped host medium and plasmonic nanolaser,” *Phys. Rev. B*, vol. 75, no. 8, p. 85436, Feb. 2007, doi: 10.1103/PhysRevB.75.085436.

[56] L. Xu, F. Li, S. Liu, F. Yao, and Y. Liu, “Low Threshold Plasmonic Nanolaser Based on Graphene,” *Applied Sciences* , vol. 8, no. 11. 2018, doi: 10.3390/app8112186.

[57] Y.-J. Lu *et al.*, “All-Color Plasmonic Nanolasers with Ultralow Thresholds: Autotuning Mechanism for Single-Mode Lasing,” *Nano Lett.*, vol. 14, no. 8, pp. 4381–4388, Aug. 2014, doi: 10.1021/nl501273u.

[58] A. S. Baburin *et al.*, “Highly directional plasmonic nanolaser based on high-performance noble metal film photonic crystal ,” in *Proc.SPIE*, May 2018, vol. 10672, [Online]. Available: https://doi.org/10.1117/12.2307572.

[59] C.-Y. Wu *et al.*, “Plasmonic Green Nanolaser Based on a Metal–Oxide–Semiconductor Structure,” *Nano Lett.*, vol. 11, no. 10, pp. 4256–4260, Oct. 2011, doi: 10.1021/nl2022477.

[60] Y. Liang, C. Li, Y.-Z. Huang, and Q. Zhang, “Plasmonic Nanolasers in On-Chip Light Sources: Prospects and Challenges,” *ACS Nano*, vol. 14, no. 11, pp. 14375–14390, Nov. 2020, doi: 10.1021/acsnano.0c07011.

[61] M. Ren *et al.*, “Nanostructured Plasmonic Medium for Terahertz Bandwidth All-Optical Switching,” *Adv. Mater.*, vol. 23, no. 46, pp. 5540–5544, Dec. 2011, doi: https://doi.org/10.1002/adma.201103162.

[62] M. T. Quint, S. Delgado, J. H. Paredes, Z. S. Nuno, L. S. Hirst, and S. Ghosh, “All-optical switching of nematic liquid crystal films driven by localized surface plasmons,” *Opt. Express*, vol. 23, no. 5, p. 6888, 2015, doi: 10.1364/oe.23.006888.

[63] J. Chen, Z. Li, X. Zhang, J. Xiao, and Q. Gong, “Submicron bidirectional all-optical plasmonic switches,” *Sci. Rep.*, vol. 3, no. 1, p. 1451, 2013, doi: 10.1038/srep01451.

[64] S. Khani, M. Danaie, and P. Rezaei, “Realization of a plasmonic optical switch using improved nano-disk resonators with Kerr-type nonlinearity: A theoretical and numerical study on challenges and solutions,” *Opt. Commun.*, vol. 477, p. 126359, 2020, doi: https://doi.org/10.1016/j.optcom.2020.126359.

[65] J. Tao, Q. J. Wang, and X. G. Huang, “All-Optical Plasmonic Switches Based on Coupled Nano-disk Cavity Structures Containing Nonlinear Material,” *Plasmonics*, vol. 6, no. 4, p. 753, 2011, doi: 10.1007/s11468-011-9260-1.

[66] C. Hoessbacher *et al.*, “The plasmonic memristor: a latching optical switch,” *Optica*, vol. 1, no. 4, pp. 198–202, 2014, doi: 10.1364/OPTICA.1.000198.

[67] M. Kauranen and A. V Zayats, “Nonlinear plasmonics,” *Nat. Photonics*, vol. 6, no. 11, pp. 737–748, 2012, doi: 10.1038/nphoton.2012.244.

[68] N. C. Panoiu, W. E. I. Sha, D. Y. Lei, and G.-C. Li, “Nonlinear optics in plasmonic nanostructures,” *J. Opt.*, vol. 20, no. 8, p. 83001, 2018, doi: 10.1088/2040-8986/aac8ed.

[69] H. Rostami, M. I. Katsnelson, and M. Polini, “Theory of plasmonic effects in nonlinear optics: The case of graphene,” *Phys. Rev. B*, vol. 95, no. 3, p. 35416, Jan. 2017, doi: 10.1103/PhysRevB.95.035416.

[70] S. Gwo *et al.*, “Plasmonic Metasurfaces for Nonlinear Optics and Quantitative SERS,” *ACS Photonics*, vol. 3, no. 8, pp. 1371–1384, Aug. 2016, doi: 10.1021/acsphotonics.6b00104.

[71] I. C. Khoo, “Nonlinear optics, active plasmonics and metamaterials with liquid crystals,” *Prog. Quantum Electron.*, vol. 38, no. 2, pp. 77–117, 2014, doi: https://doi.org/10.1016/j.pquantelec.2014.03.001.

[72] A. Cala’ Lesina, L. Ramunno, and P. Berini, “Dual-polarization plasmonic metasurface for nonlinear optics,” *Opt. Lett.*, vol. 40, no. 12, pp. 2874–2877, 2015, doi: 10.1364/OL.40.002874.

[73] N. Chauvet *et al.*, “Hybrid KTP–Plasmonic Nanostructures for Enhanced Nonlinear Optics at the Nanoscale,” *ACS Photonics*, vol. 7, no. 3, pp. 665–672, Mar. 2020, doi: 10.1021/acsphotonics.9b01484.

[74] N. Yu *et al.*, “Light Propagation with Phase Discontinuities: Generalized Laws of Reflection and Refraction,” *Science (80-.).*, vol. 334, no. 6054, pp. 333–337, 2011, doi: 10.1126/science.1210713.

[75] R. Won, “The rise of plasmonic metasurfaces,” *Nat. Photonics*, vol. 11, no. 8, pp. 462–464, 2017, doi: 10.1038/nphoton.2017.136.

[76] E. Rahimi and R. Gordon, “Nonlinear Plasmonic Metasurfaces,” *Adv. Opt. Mater.*, vol. 6, no. 18, p. 1800274, Sep. 2018, doi: https://doi.org/10.1002/adom.201800274.

[77] N. Meinzer, W. L. Barnes, and I. R. Hooper, “Plasmonic meta-atoms and metasurfaces,” *Nat. Photonics*, vol. 8, no. 12, pp. 889–898, 2014, doi: 10.1038/nphoton.2014.247.

[78] P. Wang, M. E. Nasir, A. V Krasavin, W. Dickson, Y. Jiang, and A. V Zayats, “Plasmonic Metamaterials for Nanochemistry and Sensing,” *Acc. Chem. Res.*, vol. 52, no. 11, pp. 3018–3028, Nov. 2019, doi: 10.1021/acs.accounts.9b00325.

[79] N. Yu, F. Aieta, P. Genevet, M. A. Kats, Z. Gaburro, and F. Capasso, “A Broadband, Background-Free Quarter-Wave Plate Based on Plasmonic Metasurfaces,” *Nano Lett.*, vol. 12, no. 12, pp. 6328–6333, Dec. 2012, doi: 10.1021/nl303445u.

[80] A. Pors and S. I. Bozhevolnyi, “Plasmonic metasurfaces for efficient phase control in reflection,” *Opt. Express*, vol. 21, no. 22, pp. 27438–27451, 2013, doi: 10.1364/OE.21.027438.

[81] Y. Zhao and A. Alù, “Manipulating light polarization with ultrathin plasmonic metasurfaces,” *Phys. Rev. B*, vol. 84, no. 20, p. 205428, Nov. 2011, doi: 10.1103/PhysRevB.84.205428.

[82] S. Keren-Zur, O. Avayu, L. Michaeli, and T. Ellenbogen, “Nonlinear Beam Shaping with Plasmonic Metasurfaces,” *ACS Photonics*, vol. 3, no. 1, pp. 117–123, Jan. 2016, doi: 10.1021/acsphotonics.5b00528.

[83] A. Pors, M. G. Nielsen, and S. I. Bozhevolnyi, “Analog Computing Using Reflective Plasmonic Metasurfaces,” *Nano Lett.*, vol. 15, no. 1, pp. 791–797, Jan. 2015, doi: 10.1021/nl5047297.

[84] W. T. Chen *et al.*, “Integrated plasmonic metasurfaces for spectropolarimetry,” *Nanotechnology*, vol. 27, no. 22, p. 224002, 2016, doi: 10.1088/0957-4484/27/22/224002.

[85] S. Babar and J. H. Weaver, “Optical constants of Cu, Ag, and Au revisited,” *Appl. Opt.*, vol. 54, no. 3, p. 477, 2015, doi: 10.1364/ao.54.000477.

[86] R. W. Boyd, *Nonlinear Optics*. Elsevier Science, 2020.

[87] S. J. Oldenburg, R. D. Averitt, S. L. Westcott, and N. J. Halas, “Nanoengineering of optical resonances,” *Chem. Phys. Lett.*, vol. 288, no. 2–4, pp. 243–247, 1998, doi: 10.1016/S0009-2614(98)00277-2.

[88] K. M. Mayer and J. H. Hafner, “Localized Surface Plasmon Resonance Sensors,” *Chem. Rev.*, vol. 111, no. 6, pp. 3828–3857, Jun. 2011, doi: 10.1021/cr100313v.

[89] L. Novotny and N. van Hulst, “Antennas for light,” *Nat. Photonics*, vol. 5, no. 2, pp. 83–90, 2011, doi: 10.1038/nphoton.2010.237.

[90] S. A. Maier, “Plasmonics : Metal Nanostructures for Subwavelength Photonic Devices,” vol. 12, no. 6, pp. 1214–1220, 2006.

[91] J. W. Jarrett, T. Zhao, J. S. Johnson, and K. L. Knappenberger, “Investigating Plasmonic Structure-Dependent Light Amplification and Electronic Dynamics Using Advances in Nonlinear Optical Microscopy,” *J.*

Phys. Chem. C, vol. 119, no. 28, pp. 15779–15800, Jul. 2015, doi: 10.1021/acs.jpcc.5b02494.

[92] P. Nordlander and F. Le, “Plasmonic structure and electromagnetic field enhancements in the metallic nanoparticle-film system,” *Appl. Phys. B*, vol. 84, no. 1, pp. 35–41, 2006, doi: 10.1007/s00340-006-2203-4.

[93] P. K. Jain, X. Huang, I. H. El-Sayed, and M. A. El-Sayed, “Review of Some Interesting Surface Plasmon Resonance-enhanced Properties of Noble Metal Nanoparticles and Their Applications to Biosystems,” *Plasmonics*, vol. 2, no. 3, pp. 107–118, 2007, doi: 10.1007/s11468-007-9031-1.

[94] J. M. Sanz *et al.*, “UV Plasmonic Behavior of Various Metal Nanoparticles in the Near- and Far-Field Regimes: Geometry and Substrate Effects,” *J. Phys. Chem. C*, vol. 117, no. 38, pp. 19606–19615, Sep. 2013, doi: 10.1021/jp405773p.

[95] J. A. Faucheaux, A. L. D. Stanton, and P. K. Jain, “Plasmon Resonances of Semiconductor Nanocrystals: Physical Principles and New Opportunities,” *J. Phys. Chem. Lett.*, vol. 5, no. 6, pp. 976–985, Mar. 2014, doi: 10.1021/jz500037k.

[96] J. M. Luther, P. K. Jain, T. Ewers, and A. P. Alivisatos, “Localized surface plasmon resonances arising from free carriers in doped quantum dots,” *Nat. Mater.*, vol. 10, no. 5, pp. 361–366, 2011, doi: 10.1038/nmat3004.

[97] K.-S. Lee and M. A. El-Sayed, “Gold and Silver Nanoparticles in Sensing and Imaging: Sensitivity of Plasmon Response to Size, Shape, and Metal Composition,” *J. Phys. Chem. B*, vol. 110, no. 39, pp. 19220–19225, Oct. 2006, doi: 10.1021/jp062536y.

[98] S. Link, Z. L. Wang, and M. A. El-Sayed, “Alloy Formation of Gold−Silver Nanoparticles and the Dependence of the Plasmon Absorption on Their Composition,” *J. Phys. Chem. B*, vol. 103, no. 18, pp. 3529–3533, May 1999, doi: 10.1021/jp990387w.

[99] S. W. Verbruggen, M. Keulemans, J. A. Martens, and S. Lenaerts, "Predicting the Surface Plasmon Resonance Wavelength of Gold–Silver Alloy Nanoparticles," *J. Phys. Chem. C*, vol. 117, no. 37, pp. 19142–19145, Sep. 2013, doi: 10.1021/jp4070856.

[100] B. J. Wiley, S. H. Im, Z.-Y. Li, J. McLellan, A. Siekkinen, and Y. Xia, "Maneuvering the Surface Plasmon Resonance of Silver Nanostructures through Shape-Controlled Synthesis," *J. Phys. Chem. B*, vol. 110, no. 32, pp. 15666–15675, Aug. 2006, doi: 10.1021/jp0608628.

[101] J. B. Pendry, "Negative refraction makes a perfect lens," *Phys. Rev. Lett.*, vol. 85, no. 18, pp. 3966–3969, 2000, doi: 10.1103/PhysRevLett.85.3966.

[102] R. Fleury, F. Monticone, and A. Alù, "Invisibility and cloaking: Origins, present, and future perspectives," *Phys. Rev. Appl.*, vol. 4, no. 3, pp. 1–20, 2015, doi: 10.1103/PhysRevApplied.4.037001.

[103] V. M. S. A. K. Sarychev, *Electrodynamics of Metamaterials*. World Scientific, Singapore, 2007.

[104] M. S. R. Marques , F. Martin, *Metamaterials with Negative Parameters: Theory, Design and Microwave Applications*. Wiley , New York, 2008.

[105] R. W. Z. N. Engheta, *Metamaterials: Physics and Engineering Explorations*. Wiley , New York, 2006.

[106] G. V. Eleftheriades and K. G. Balmain, *Negative-Refraction Metamaterials*. Wiley , New York, 2005.

[107] T. I. C. Caloz, *Electromagnetic Metamaterials: Transmission Line Theory and Microwave Applications*. Wiley, New york, 2005.

[108] P. Y. Chen, J. Soric, and A. Alù, "Invisibility and cloaking based on scattering cancellation," *Adv. Mater.*, vol. 24, no. 44, pp. 281–304, 2012, doi: 10.1002/adma.201202624.

[109] J. B. Pendry *et al.*, "Controlling Electromagnetic Fields," *Science (80-.).*, vol. 312, no. 5781, pp. 1780–1782, 2006, doi: 10.1126/science.1125907.

[110] B. J. Justice *et al.*, “Metamaterial electromagnetic cloak at microwave frequencies,” *Science (80-.).*, vol. 314, no. 5801, pp. 977–980, 2006, doi: 10.1126/science.1133628.

[111] J. Perczel, T. Tyc, and U. Leonhardt, “Invisibility cloaking without superluminal propagation,” *New J. Phys.*, vol. 13, 2011, doi: 10.1088/1367-2630/13/8/083007.

[112] J. Li and J. B. Pendry, “Hiding under the carpet: A new strategy for cloaking,” *Phys. Rev. Lett.*, vol. 101, no. 20, pp. 1–4, 2008, doi: 10.1103/PhysRevLett.101.203901.

[113] M. Gharghi *et al.*, “A carpet cloak for visible light,” *Nano Lett.*, vol. 11, no. 7, pp. 2825–2828, 2011, doi: 10.1021/nl201189z.

[114] J. Valentine, J. Li, T. Zentgraf, G. Bartal, and X. Zhang, “An optical cloak made of dielectrics,” *Nat. Mater.*, vol. 8, no. 7, pp. 568–571, 2009, doi: 10.1038/nmat2461.

[115] T. Ergin, J. C. Halimeh, N. Stenger, and M. Wegener, “Optical microscopy of 3D carpet cloaks:ray-tracing calculations,” *Opt. Express*, vol. 18, no. 19, pp. 20535–20545, 2010, doi: 10.1364/OE.18.020535.

[116] A. Alù, “Mantle cloak: Invisibility induced by a surface,” *Phys. Rev. B - Condens. Matter Mater. Phys.*, vol. 80, no. 24, pp. 1–5, 2009, doi: 10.1103/PhysRevB.80.245115.

[117] P.-Y. Chen and A. Alù, “Mantle cloaking using thin patterned metasurfaces,” *Phys. Rev. B*, vol. 84, no. 20, p. 205110, Nov. 2011, doi: 10.1103/PhysRevB.84.205110.

[118] Y. R. Padooru, A. B. Yakovlev, P. Y. Chen, and A. Alù, “Line-source excitation of realistic conformal metasurface cloaks,” *J. Appl. Phys.*, vol. 112, no. 10, 2012, doi: 10.1063/1.4765688.

[119] B. A. Munk, “Frequency Selective Surfaces: Theory and Design,” *New York*, p. 416, 2000, doi: 10.1002/0471723770.

[120] P. Y. Chen and A. Alù, “Atomically thin surface cloak using graphene monolayers,” *ACS Nano*, vol. 5, no. 7, pp. 5855–5863, 2011, doi: 10.1021/nn201622e.

[121] A. Monti *et al.*, “Mantle cloaking for co-site radio-frequency antennas,” *Appl. Phys. Lett.*, vol. 108, no. 11, p. 113502, Mar. 2016, doi: 10.1063/1.4944042.

[122] A. Monti, J. C. Soric, A. Alù, A. Toscano, and F. Bilotti, “Anisotropic Mantle Cloaks for TM and TE Scattering Reduction,” *IEEE Trans. Antennas Propag.*, vol. 63, no. 4, pp. 1775–1788, 2015, doi: 10.1109/TAP.2015.2396532.

[123] P.-Y. Chen, J. Soric, and A. Alù, “Invisibility and Cloaking Based on Scattering Cancellation,” *Adv. Mater.*, vol. 24, no. 44, pp. OP281–OP304, 2012, doi: https://doi.org/10.1002/adma.201202624.

[124] A. Alù and N. Engheta, “Achieving transparency with plasmonic and metamaterial coatings,” *Phys. Rev. E*, vol. 72, no. 1, p. 16623, Jul. 2005, doi: 10.1103/PhysRevE.72.016623.

[125] M. G. Silveirinha, A. Alù, and N. Engheta, “Infrared and optical invisibility cloak with plasmonic implants based on scattering cancellation,” *Phys. Rev. B - Condens. Matter Mater. Phys.*, vol. 78, no. 7, pp. 1–7, 2008, doi: 10.1103/PhysRevB.78.075107.

[126] A. Alù and N. Engheta, “Multifrequency optical invisibility cloak with layered plasmonic shells,” *Phys. Rev. Lett.*, vol. 100, no. 11, pp. 1–4, 2008, doi: 10.1103/PhysRevLett.100.113901.

[127] M. Farhat, S. Bin Hasan, S. Mu, and A. Cunningham, “A self-assembled three-dimensional cloak in the visible ´,” pp. 1–7, 2013, doi: 10.1038/srep02328.

[128] S. Mühlig *et al.*, “A self-assembled three-dimensional cloak in the visible,” *Sci. Rep.*, vol. 3, pp. 1–7, Aug. 2013, doi: 10.1038/srep02328.

[129] M. G. Silveirinha, A. Alù, and N. Engheta, “Cloaking mechanism with antiphase plasmonic satellites,” *Phys. Rev. B - Condens. Matter Mater. Phys.*, vol. 78, no. 20, pp. 1–9, 2008, doi: 10.1103/PhysRevB.78.205109.

[130] A. Alú and N. Engheta, “Theory and potentials of multi-layered plasmonic covers for multi-frequency cloaking,” *New J. Phys.*, vol. 10, p. 115036, 2008.

[131] A. Alù and N. Engheta, “Cloaked near-field scanning optical microscope tip for noninvasive near-field imaging,” *Phys. Rev. Lett.*, vol. 105, no. 26, pp. 1–4, 2010, doi: 10.1103/PhysRevLett.105.263906.

[132] A. Alù and N. Engheta, “Cloaking a receiving antenna or a sensor with plasmonic metamaterials,” *Metamaterials*, vol. 4, no. 2, pp. 153–159, 2010, doi: https://doi.org/10.1016/j.metmat.2010.03.005.

[133] A. Alù and N. Engheta, “Cloaking a sensor,” *Phys. Rev. Lett.*, vol. 102, no. 23, pp. 1–4, 2009, doi: 10.1103/PhysRevLett.102.233901.

[134] P. Chýlek and J. Zhan, *Absorption and scattering of light by small particles: the interference structure*, vol. 29, no. 28. 2009.

[135] M. G. Silveirinha, A. Alù, and N. Engheta, “Parallel-plate metamaterials for cloaking structures,” *Phys. Rev. E - Stat. Nonlinear, Soft Matter Phys.*, vol. 75, no. 3, pp. 1–16, 2007, doi: 10.1103/PhysRevE.75.036603.

[136] J. C. M. Garnett and J. Larmor, “XII. Colours in metal glasses and in metallic films,” *Philos. Trans. R. Soc. London. Ser. A, Contain. Pap. a Math. or Phys. Character*, vol. 203, no. 359–371, pp. 385–420, Jan. 1904, doi: 10.1098/rsta.1904.0024.

[137] T. C. Choy, *Effective Medium Theory: Principles and Applications*, 2nd ed. Oxford: Oxford University Press, 2015.

[138] V. Markel, “Introduction to the Maxwell Garnett approximation : tutorial Vadim Markel To cite this version : HAL Id : hal-01282105 Introduction to Maxwell Garnett approximation : tutorial,” 2016.

[139] V. C. De Silva, P. Nyga, and V. P. Drachev, “Scattering suppression in epsilon-near-zero plasmonic fractal shells,” vol. 5, no. 11, pp. 2183–2186, 2015, doi: 10.1364/OME.5.002491.

[140] K. Yao and Y. Liu, “Plasmonic metamaterials,” vol. 3, no. 2, pp. 177–210, 2014, doi: 10.1515/ntrev-2012-0071.

[141] W. Zhao and X. Zhao, “Fabrication and characterization of metamaterials at optical frequencies,” *Opt. Mater. (Amst).*, vol. 32, no. 3, pp. 422–426, 2010, doi: 10.1016/j.optmat.2009.09.012.

[142] L. O. Herrmann *et al.*, “Threading plasmonic nanoparticle strings with light,” *Nat. Commun.*, vol. 5, 2014, doi: 10.1038/ncomms5568.

[143] M. I. Stockman, “Nanoplasmonics: past, present, and glimpse into future,” *Opt. Express*, vol. 19, no. 22, pp. 22029–22106, 2011, doi: 10.1364/OE.19.022029.

[144] M. Jablan, H. Buljan, and M. Soljačić, “Plasmonics in graphene at infrared frequencies,” *Phys. Rev. B - Condens. Matter Mater. Phys.*, vol. 80, no. 24, pp. 1–7, 2009, doi: 10.1103/PhysRevB.80.245435.

[145] P. Dey, S. Zhu, K. J. Thurecht, and M. Fredericks, “assemblies mediated by hyperbranched polymer,” pp. 2827–2837, 2014, doi: 10.1039/c4tb00263f.

[146] H. Chen, “Metamaterials: constitutive parameters, performance, and chemical methods for realization,” *J. Mater. Chem.*, vol. 21, no. 18, pp. 6452–6463, 2011, doi: 10.1039/C0JM03138K.

[147] P. R. West, S. Ishii, G. V. Naik, N. K. Emani, V. M. Shalaev, and A. Boltasseva, “Searching for better plasmonic materials,” *Laser Photonics Rev.*, vol. 4, no. 6, pp. 795–808, 2010, doi: 10.1002/lpor.200900055.

[148] B. Edwards, A. Alù, M. G. Silveirinha, and N. Engheta, “Experimental verification of plasmonic cloaking at microwave frequencies with metamaterials,” *Phys. Rev. Lett.*, vol. 103, no. 15, pp. 1–4, 2009, doi: 10.1103/PhysRevLett.103.153901.

[149] A. Alù and N. Engheta, “Cloaking and transparency for collections of particles with metamaterial and plasmonic covers,” *Opt. Express*, vol. 15, no. 12, p. 7578, 2007, doi: 10.1364/OE.15.007578.

[150] D. S. Filonov, A. P. Slobozhanyuk, P. A. Belov, and Y. S. Kivshar, “Double-shell metamaterial coatings for plasmonic cloaking,” *Phys. Status Solidi - Rapid Res. Lett.*, vol. 6, no. 1, pp. 46–48, 2012, doi: 10.1002/pssr.201105475.

[151] C. Argyropoulos, P. Y. Chen, F. Monticone, G. D’Aguanno, and A. Alù, “Nonlinear plasmonic cloaks to realize giant all-optical scattering switching,” *Phys. Rev. Lett.*, vol. 108, no. 26, pp. 1–5, 2012, doi: 10.1103/PhysRevLett.108.263905.

[152] A. Alù and N. Engheta, “Effects of size and frequency dispersion in plasmonic cloaking,” *Phys. Rev. E - Stat. Nonlinear, Soft Matter Phys.*, vol. 78, no. 4, pp. 1–4, 2008, doi: 10.1103/PhysRevE.78.045602.

[153] S. Tricarico, F. Bilotti, A. Alù, and L. Vegni, “Plasmonic cloaking for irregular objects with anisotropic scattering properties,” *Phys. Rev. E - Stat. Nonlinear, Soft Matter Phys.*, vol. 81, no. 2, pp. 1–12, 2010, doi: 10.1103/PhysRevE.81.026602.

[154] S. Mühlig, M. Farhat, C. Rockstuhl, and F. Lederer, “Cloaking dielectric spherical objects by a shell of metallic nanoparticles,” *Phys. Rev. B - Condens. Matter Mater. Phys.*, vol. 83, no. 19, pp. 1–14, 2011, doi: 10.1103/PhysRevB.83.195116.

[155] S. Mühlig *et al.*, “Self-assembled plasmonic metamaterials,” *Nanophotonics*, vol. 2, no. 3, pp. 211–240, 2013, doi: 10.1515/nanoph-2012-0036.

[156] A. Monti, F. Bilotti, and A. Toscano, “Optical cloaking of cylindrical objects by using covers made of core–shell nanoparticles,” *Opt. Lett.*, vol. 36, no. 23, p. 4479, 2011, doi: 10.1364/ol.36.004479.

[157] M. Farhat *et al.*, “Understanding the functionality of an array of invisibility cloaks,” *Phys. Rev. B - Condens. Matter Mater. Phys.*, vol. 84, no. 23, pp. 2–7, 2011, doi: 10.1103/PhysRevB.84.235105.

[158] D. Rainwater, A. Kerkhoff, K. Melin, J. C. Soric, G. Moreno, and A. Alù, “Experimental verification of three-dimensional plasmonic cloaking in free-space,” *New J. Phys.*, vol. 14, 2012, doi: 10.1088/1367-2630/14/1/013054.

[159] M. Farhat, S. Mühlig, C. Rockstuhl, and F. Lederer, “Scattering cancellation of the magnetic dipole field from macroscopic spheres,” *Opt. Express*, vol. 20, no. 13, pp. 13896–13906, 2012, doi: 10.1364/OE.20.013896.

[160] G. Labate and L. Matekovits, “Invisibility and cloaking structures as weak or strong solutions of Devaney-Wolf theorem,” *Opt. Express*, vol. 24, no. 17, pp. 19245–19253, 2016, doi: 10.1364/OE.24.019245.

[161] A. Monti, F. Bilotti, A. Toscano, and L. Vegni, “Possible implementation of epsilon-near-zero metamaterials working at optical frequencies,” *Opt. Commun.*, vol. 285, no. 16, pp. 3412–3418, 2012, doi: https://doi.org/10.1016/j.optcom.2011.12.037.

[162] A. Monti, A. Alù, A. Toscano, and F. Bilotti, “Optical Scattering Cancellation through Arrays of Plasmonic Nanoparticles: A Review,” pp. 540–552, 2015, doi: 10.3390/photonics2020540.

[163] A. Monti, A. Alù, A. Toscano, and F. Bilotti, “Optical invisibility through metasurfaces made of plasmonic nanoparticles,” *J. Appl. Phys.*, vol. 117, no. 12, 2015, doi: 10.1063/1.4916257.

[164] A. Alù and N. Engheta, “Theory and potentials of multi-layered plasmonic covers for multi-frequency cloaking,” *New J. Phys.*, vol. 10, 2008, doi: 10.1088/1367-2630/10/11/115036.

[165] R. Fleury and A. Alu, “CLOAKING AND INVISIBILITY: A REVIEW (Invited Review),” *Prog. Electromagn. Res.*, vol. 147, no. 1, pp. 171–202, 2015, doi: 10.2528/pier15011403.

[166] A. L. Rodarte, R. J. Pandolfi, S. Ghosh, and L. S. Hirst, "Quantum dot/liquid crystal composite materials: Self-assembly driven by liquid crystal phase transition templating," *J. Mater. Chem. C*, vol. 1, no. 35, pp. 5527–5532, 2013, doi: 10.1039/c3tc31043d.

[167] M. T. Quint *et al.*, "Plasmon-actuated nano-assembled microshells," *Sci. Rep.*, vol. 7, no. 1, pp. 1–11, 2017, doi: 10.1038/s41598-017-17691-6.

[168] R. Mathon and R. L. Johnston, "The Approximate Solution of Elliptic Boundary-Value Problems by Fundamental Solutions," *SIAM J. Numer. Anal.*, vol. 14, no. 4, pp. 638–650, Sep. 1977, doi: 10.1137/0714043.

[169] A. Doicu, *Acoustic and Electromagnetic Scattering Analysis Using Discrete Sources*. 2000.

[170] L. L. Foldy, "The Multiple Scattering of Waves. I. General Theory of Isotropic Scattering by Randomly Distributed Scatterers," *Phys. Rev.*, vol. 67, no. 3–4, pp. 107–119, Feb. 1945, doi: 10.1103/PhysRev.67.107.

[171] M. Lax, "Multiple Scattering of Waves. II. The Effective Field in Dense Systems," *Phys. Rev.*, vol. 85, no. 4, pp. 621–629, Feb. 1952, doi: 10.1103/PhysRev.85.621.

[172] K. Huang, K. Solna, and H. Zhao, "Generalized Foldy-Lax formulation," *J. Comput. Phys.*, vol. 229, no. 12, pp. 4544–4553, 2010, doi: 10.1016/j.jcp.2010.02.021.

[173] M. Born *et al.*, *Principles of Optics: Electromagnetic Theory of Propagation, Interference and Diffraction of Light*. Cambridge University Press, 1999.

[174] A. Ishimaru, "Scattering of Pulse Waves from a Random Distribution of Particles," in *Wave Propagation and Scattering in Random Media*, IEEE, 1997, pp. 93–115.

[175] A. Ishimaru, *Wave Propagation and Scattering in Random Media*. Wiley, 1999.

[176] K. M. McPeak *et al.*, “Plasmonic films can easily be better: Rules and recipes,” *ACS Photonics*, vol. 2, no. 3, pp. 326–333, 2015, doi: 10.1021/ph5004237.

[177] Á. González, “Measurement of Areas on a Sphere Using Fibonacci and Latitude–Longitude Lattices,” *Math. Geosci.*, vol. 42, no. 1, p. 49, 2009, doi: 10.1007/s11004-009-9257-x.

[178] E. Hutter and J. H. Fendler, “Exploitation of Localized Surface Plasmon Resonance,” *Adv. Mater.*, vol. 16, no. 19, pp. 1685–1706, 2004, doi: https://doi.org/10.1002/adma.200400271.

[179] J. Zhao, X. Zhang, C. R. Yonzon, A. J. Haes, and R. P. Van Duyne, “Localized surface plasmon resonance biosensors,” *Nanomedicine*, vol. 1, no. 2, pp. 219–228, 2006, doi: 10.2217/17435889.1.2.219.

[180] E. Petryayeva and U. J. Krull, “Localized surface plasmon resonance: Nanostructures, bioassays and biosensing—A review,” *Anal. Chim. Acta*, vol. 706, no. 1, pp. 8–24, 2011, doi: https://doi.org/10.1016/j.aca.2011.08.020.

[181] A. Alù, “Designer matter: Fascinating interactions of light and sound with metamaterials,” *MRS Bull.*, vol. 42, no. 9, pp. 677–682, 2017, doi: 10.1557/mrs.2017.188.

[182] M. B. Ross, C. A. Mirkin, and G. C. Schatz, “Optical Properties of One-, Two-, and Three-Dimensional Arrays of Plasmonic Nanostructures,” *J. Phys. Chem. C*, vol. 120, no. 2, pp. 816–830, Jan. 2016, doi: 10.1021/acs.jpcc.5b10800.

[183] N. Liu, H. Guo, L. Fu, S. Kaiser, H. Schweizer, and H. Giessen, “Three-dimensional photonic metamaterials at optical frequencies,” *Nat. Mater.*, vol. 7, no. 1, pp. 31–37, 2008, doi: 10.1038/nmat2072.

[184] D. García-Lojo *et al.*, “Plasmonic Supercrystals,” *Acc. Chem. Res.*, vol. 52, no. 7, pp. 1855–1864, 2019, doi: 10.1021/acs.accounts.9b00213.

[185] J. Zhu and L. L. Goddard, “All-dielectric concentration of electromagnetic fields at the nanoscale: the role of photonic nanojets,” *Nanoscale Adv.*, vol. 1, no. 12, pp. 4615–4643, 2019, doi: 10.1039/C9NA00430K.

[186] D. McCloskey, J. J. Wang, and J. F. Donegan, “Low divergence photonic nanojets from Si3N4 microdisks,” *Opt. Express*, vol. 20, no. 1, pp. 128–140, Jan. 2012, doi: 10.1364/OE.20.000128.

[187] H. Choo *et al.*, “Nanofocusing in a metal–insulator–metal gap plasmon waveguide with a three-dimensional linear taper,” *Nat. Photonics*, vol. 6, no. 12, pp. 838–844, 2012, doi: 10.1038/nphoton.2012.277.

[188] R. Gordon, D. Sinton, K. L. Kavanagh, and A. G. Brolo, “A New Generation of Sensors Based on Extraordinary Optical Transmission,” *Acc. Chem. Res.*, vol. 41, no. 8, pp. 1049–1057, Aug. 2008, doi: 10.1021/ar800074d.

[189] H. Im *et al.*, “Label-free detection and molecular profiling of exosomes with a nano-plasmonic sensor,” *Nat. Biotechnol.*, vol. 32, no. 5, pp. 490–495, 2014, doi: 10.1038/nbt.2886.

[190] T. W. Ebbesen, H. J. Lezec, H. F. Ghaemi, T. Thio, and P. A. Wolff, “Extraordinary optical transmission through sub-wavelength hole arrays,” *Nature*, vol. 391, no. 6668, pp. 667–669, 1998, doi: 10.1038/35570.

[191] S. Linden *et al.*, “Photonic metamaterials: Magnetism at optical frequencies,” *IEEE J. Sel. Top. Quantum Electron.*, vol. 12, no. 6, pp. 1097–1104, 2006, doi: 10.1109/JSTQE.2006.880600.

[192] M. Mayer, M. J. Schnepf, T. A. F. König, and A. Fery, “Colloidal Self-Assembly Concepts for Plasmonic Metasurfaces,” *Adv. Opt. Mater.*, vol. 7, no. 1, 2019, doi: 10.1002/adom.201800564.

[193] S. Ghosh *et al.*, “Directed Self-Assembly Driven Mesoscale Lithography Using Laser-Induced and Manipulated Microbubbles: Complex Architectures and Diverse Applications,” *Nano Lett.*, vol. 21, no. 1, pp. 10–

25, 2021, doi: 10.1021/acs.nanolett.0c03839.

[194] M. B. Ross, J. C. Ku, V. M. Vaccarezza, G. C. Schatz, and C. A. Mirkin, “Nanoscale form dictates mesoscale function in plasmonic DNA–nanoparticle superlattices,” *Nat. Nanotechnol.*, vol. 10, no. 5, pp. 453–458, 2015, doi: 10.1038/nnano.2015.68.

[195] K. L. Young *et al.*, “Using DNA to Design Plasmonic Metamaterials with Tunable Optical Properties,” *Adv. Mater.*, vol. 26, no. 4, pp. 653–659, 2014, doi: https://doi.org/10.1002/adma.201302938.

[196] A. L. Rodarte, R. J. Pandolfi, S. Ghosh, and L. S. Hirst, “Quantum dot/liquid crystal composite materials: Self-assembly driven by liquid crystal phase transition templating,” *J. Mater. Chem. C*, vol. 1, no. 35, pp. 5527–5532, 2013, doi: 10.1039/c3tc31043d.

[197] A. L. Rodarte *et al.*, “Self-assembled nanoparticle micro-shells templated by liquid crystal sorting,” *Soft Matter*, vol. 11, no. 9, pp. 1701–1707, 2015, doi: 10.1039/c4sm02326a.

[198] A. Masłowska, P. J. Flatau, and G. L. Stephens, “On the validity of the anomalous diffraction theory to light scattering by cubes,” *Opt. Commun.*, vol. 107, no. 1, pp. 35–40, 1994, doi: https://doi.org/10.1016/0030-4018(94)90099-X.

[199] K. Atkinson, “Numerical integration on the sphere,” *J. Austral. Math. Soc. Ser. B*, vol. 23, no. 3, pp. 332–347, 1982, doi: 10.1017/S0334270000000278.

[200] L. G. Henyey and J. L. Greenstein, “Diffuse radiation in the galaxy,” *Astrophys. J.*, vol. 93, pp. 70–83, 1941.

[201] K. R. ILER, “The Chemistry of Silica,” *Solubility, Polym. Colloid Surf. Prop. Biochem. Silica*, 1979, [Online]. Available: https://ci.nii.ac.jp/naid/10029819198/en/.

[202] A. B, “Tailoring surfaces with silanes,” *CHEM. TECH*, vol. 7, no. 12, pp.

755–788, 1977.

[203] H. S. Jung, D. S. Moon, and J. K. Lee, “Quantitative analysis and efficient surface modification of silica nanoparticles,” *J. Nanomater.*, vol. 2012, 2012, doi: 10.1155/2012/593471.

[204] C. Bresson, M.-J. Menu, M. Dartiguenave, and Y. Dartiguenave, “Triethoxysilyl-substituted aminoethanethiol ligands for zinc and cadmium complexes and aminoethanethiol-modified silica gel. Evaluation of the corresponding supported molecular trap for metallic pollutant uptake (Cd2+{,} Hg2+ and Pb2+),” *J. Environ. Monit.*, vol. 2, no. 3, pp. 240–247, 2000, doi: 10.1039/B001408G.

[205] P. W. Schindler, B. Fürst, R. Dick, and P. U. Wolf, “Ligand properties of surface silanol groups. I. surface complex formation with Fe3+, Cu2+, Cd2+, and Pb2+,” *J. Colloid Interface Sci.*, vol. 55, no. 2, pp. 469–475, 1976, doi: https://doi.org/10.1016/0021-9797(76)90057-6.

[206] K. C. Vrancken, L. De Coster, P. Van Der Voort, P. J. Grobet, and E. F. Vansant, “The Role of Silanols in the Modification of Silica Gel with Aminosilanes,” *J. Colloid Interface Sci.*, vol. 170, no. 1, pp. 71–77, 1995, doi: https://doi.org/10.1006/jcis.1995.1073.

[207] T. Ishikawa *et al.*, “Surface silanol groups of mesoporous silica FSM-16,” *J. Chem. Soc. Faraday Trans.*, vol. 92, no. 11, pp. 1985–1989, 1996, doi: 10.1039/FT9969201985.

[208] L. T. Zhuravlev and V. V Potapov, “Density of silanol groups on the surface of silica precipitated from a hydrothermal solution,” *Russ. J. Phys. Chem.*, vol. 80, no. 7, pp. 1119–1128, 2006, doi: 10.1134/S0036024406070211.

[209] D. Kino, K. Okada, Y. Tokudome, M. Takahashi, L. Malfatti, and P. Innocenzi, “Reactivity of silanol group on siloxane oligomers for designing molecular structure and surface wettability,” *J. Sol-Gel Sci. Technol.*, vol. 97, no. 3, pp. 734–742, 2021, doi: 10.1007/s10971-020-05448-z.

[210] S. L. Warring, D. A. Beattie, and A. J. McQuillan, “Surficial Siloxane-to-Silanol Interconversion during Room-Temperature Hydration/Dehydration of Amorphous Silica Films Observed by ATR-IR and TIR-Raman Spectroscopy,” *Langmuir*, vol. 32, no. 6, pp. 1568–1576, Feb. 2016, doi: 10.1021/acs.langmuir.5b04506.

[211] R. G. Acres *et al.*, “Molecular Structure of 3-Aminopropyltriethoxysilane Layers Formed on Silanol-Terminated Silicon Surfaces,” *J. Phys. Chem. C*, vol. 116, no. 10, pp. 6289–6297, Mar. 2012, doi: 10.1021/jp212056s.

[212] B. Sadtler and A. Wei, “Spherical ensembles of gold nanoparticles on silica: electrostatic and size effects,” *Chem. Commun.*, no. 15, pp. 1604–1605, 2002, doi: 10.1039/B204760H.

[213] R. Grillo, D. Beutel, U. Cataldi, C. Rockstuhl, and T. Bu, “Self-Assembled Arrays of Gold Nanorod-Decorated Dielectric Microspheres with a Magnetic Dipole Response in the Visible Range for Perfect Lensing and Cloaking Applications,” 2020, doi: 10.1021/acsanm.0c01346.

[214] S. E. Denmark and G. L. Beutner, “Lewis Base Catalysis in Organic Synthesis,” *Angew. Chemie Int. Ed.*, vol. 47, no. 9, pp. 1560–1638, Feb. 2008, doi: https://doi.org/10.1002/anie.200604943.

[215] A.-J. Liu, Y. Han, F. Xu, S.-D. Han, J. Pan, and G.-M. Wang, “Coordinate bond- and hydrogen bond-assisted electron transfer strategy towards the generation of photochromic metal phosphites,” *Dalt. Trans.*, vol. 49, no. 41, pp. 14598–14604, 2020, doi: 10.1039/D0DT03010D.

[216] A. Schroedter and H. Weller, “Ligand Design and Bioconjugation of Colloidal Gold Nanoparticles,” *Angew. Chemie Int. Ed.*, vol. 41, no. 17, pp. 3218–3221, Sep. 2002, doi: https://doi.org/10.1002/1521-3773(20020902)41:17<3218::AID-ANIE3218>3.0.CO;2-P.

[217] S. Gomez, K. Philippot, V. Collière, B. Chaudret, F. Senocq, and P. Lecante, “Gold nanoparticles from self-assembled gold() amine precursors,”

Chem. Commun., no. 19, pp. 1945–1946, 2000, doi: 10.1039/B005327I.

[218] M. J. Rak, N. K. Saadé, T. Friščić, and A. Moores, “Mechanosynthesis of ultra-small monodisperse amine-stabilized gold nanoparticles with controllable size,” *Green Chem.*, vol. 16, no. 1, pp. 86–89, 2014, doi: 10.1039/C3GC41827H.

[219] A. Oliva-Puigdomènech, J. De Roo, J. Kuhs, C. Detavernier, J. C. Martins, and Z. Hens, “Ligand Binding to Copper Nanocrystals: Amines and Carboxylic Acids and the Role of Surface Oxides,” *Chem. Mater.*, vol. 31, no. 6, pp. 2058–2067, Mar. 2019, doi: 10.1021/acs.chemmater.8b05107.

[220] H. Ye, R. W. J. Scott, and R. M. Crooks, “Synthesis, Characterization, and Surface Immobilization of Platinum and Palladium Nanoparticles Encapsulated within Amine-Terminated Poly(amidoamine) Dendrimers,” *Langmuir*, vol. 20, no. 7, pp. 2915–2920, Mar. 2004, doi: 10.1021/la0361060.

[221] D. Mercier, J.-C. Rouchaud, and M.-G. Barthés-Labrousse, “Interaction of amines with native aluminium oxide layers in non-aqueous environment: Application to the understanding of the formation of epoxy-amine/metal interphases,” *Appl. Surf. Sci.*, vol. 254, no. 20, pp. 6495–6503, 2008, doi: https://doi.org/10.1016/j.apsusc.2008.04.010.

[222] S. D. Techane, L. J. Gamble, and D. G. Castner, “X-ray photoelectron spectroscopy characterization of gold nanoparticles functionalized with amine-terminated alkanethiols,” *Biointerphases*, vol. 6, no. 3, pp. 98–104, Aug. 2011, doi: 10.1116/1.3622481.

[223] S. Mühlig *et al.*, “Self-assembled plasmonic core-shell clusters with an isotropic magnetic dipole response in the visible range,” *ACS Nano*, vol. 5, no. 8, pp. 6586–6592, 2011, doi: 10.1021/nn201969h.

[224] N. Chiron, R. Guilet, and E. Deydier, “Adsorption of Cu(II) and Pb(II) onto a grafted silica: isotherms and kinetic models,” *Water Res.*, vol. 37, no. 13,

pp. 3079–3086, 2003, doi: https://doi.org/10.1016/S0043-1354(03)00156-8.

[225] T. J. Williams, “Scanning electron microscopy and x-ray microanalysis, 3rd edition. By Joseph Goldstein, Dale Newbury, David Joy, Charles Lyman, Patrick Echlin, Eric Lifshin, Linda Sawyer, Joseph Michael Kluwer Academic Publishers, New York (2003) ISBN 0306472929; hardbac,” *Scanning*, vol. 27, no. 4, pp. 215–216, Jul. 2005, doi: https://doi.org/10.1002/sca.4950270410.

[226] M. De Graef *et al.*, *Introduction to the Scanning Electron Microscope*, vol. 9, no. S02. 2018.

[227] C. A. Schneider, W. S. Rasband, and K. W. Eliceiri, “NIH Image to ImageJ: 25 years of image analysis,” *Nat. Methods*, vol. 9, no. 7, pp. 671–675, 2012, doi: 10.1038/nmeth.2089.

[228] K. OHKUBO, “Integrating Sphere Theory for Measuring Optical Radiation,” *J. Light Vis. Environ.*, vol. 34, no. 2, pp. 111–122, 2010, doi: 10.2150/jlve.34.111.

[229] J. L. Taylor, “Integrating Sphere Functionality : The Scatter Transmission Measurement,” pp. 1–6, 2013.

[230] T. E. C. Cal, “Integrating Sphere Theory and Applications.”

[231] S. A. Mann *et al.*, “Integrating Sphere Microscopy for Direct Absorption Measurements of Single Nanostructures,” *ACS Nano*, vol. 11, no. 2, pp. 1412–1418, 2017, doi: 10.1021/acsnano.6b06534.

[232] Newport, “Integrating Sphere Components,” pp. 3–6, [Online]. Available: https://www.newport.com/medias/sys_master/images/images/hc3/h13/8797116858398/Integrating-Spheres-Datasheet.pdf.

[233] J. W. Strutt, *Scientific Papers: Volume 3: 1887–1892*, vol. 3. Cambridge: Cambridge University Press, 2009.

[234] M. Tsang, R. Nair, and X.-M. Lu, “Quantum Theory of Superresolution for Two Incoherent Optical Point Sources,” *Phys. Rev. X*, vol. 6, no. 3, p.

31033, Aug. 2016, doi: 10.1103/PhysRevX.6.031033.

[235] R. Nair and M. Tsang, “Interferometric superlocalization of two incoherent optical point sources,” *Opt. Express*, vol. 24, no. 4, pp. 3684–3701, 2016, doi: 10.1364/OE.24.003684.

[236] M. Tsang, R. Nair, and X.-M. Lu, “Quantum information for semiclassical optics,” in *Proc.SPIE*, Nov. 2016, vol. 10029, [Online]. Available: https://doi.org/10.1117/12.2245733.

[237] R. Nair and M. Tsang, “Far-Field Superresolution of Thermal Electromagnetic Sources at the Quantum Limit,” *Phys. Rev. Lett.*, vol. 117, no. 19, p. 190801, Nov. 2016, doi: 10.1103/PhysRevLett.117.190801.

[238] M. Tsang, “Conservative classical and quantum resolution limits for incoherent imaging,” *J. Mod. Opt.*, vol. 65, no. 11, pp. 1385–1391, Jun. 2018, doi: 10.1080/09500340.2017.1377306.

[239] S. Z. Ang, R. Nair, and M. Tsang, “Quantum limit for two-dimensional resolution of two incoherent optical point sources,” *Phys. Rev. A*, vol. 95, no. 6, p. 63847, Jun. 2017, doi: 10.1103/PhysRevA.95.063847.

[240] M. Tsang, “Subdiffraction incoherent optical imaging via spatial-mode demultiplexing,” *New J. Phys.*, vol. 19, no. 2, p. 23054, 2017, doi: 10.1088/1367-2630/aa60ee.

[241] X.-M. Lu, H. Krovi, R. Nair, S. Guha, and J. H. Shapiro, “Quantum-optimal detection of one-versus-two incoherent optical sources with arbitrary separation,” *npj Quantum Inf.*, vol. 4, no. 1, p. 64, 2018, doi: 10.1038/s41534-018-0114-y.

[242] M. Tsang and R. Nair, “Resurgence of Rayleigh’s curse in the presence of partial coherence: comment,” *Optica*, vol. 6, no. 4, pp. 400–401, 2019, doi: 10.1364/OPTICA.6.000400.

[243] G. R. Fowles, *Introduction to Modern Optics*. Dover Publications, 1989.